SAPIENZA
UNIVERSITÀ DI ROMA

Irreversibility and nonequilibrium properties in dynamical models for turbulence and geophysical systems

Scuola Dottorale in Scienze Astronomiche, Chimiche, Fisiche, Matematiche e della Terra "Vito Volterra"
Dottorato in Fisica (XXXVII cycle)

Niccolò Cocciaglia
ID number 1763735

Advisors
Prof. Angelo Vulpiani
Dr. Massimo Cencini

Academic Year 2023/2024

Thesis defended on January 29th, 2025
in front of a Board of Examiners composed by:

Dr. Michele Buzzicotti
Prof. Tobias Galla
Prof. Vito Latora
Prof. Samir Simon Suweis

Reviewers:

Dr. Michele Buzzicotti
Prof. Filippo De Lillo

Irreversibility and nonequilibrium properties in dynamical models for turbulence and geophysical systems
PhD thesis. Sapienza University of Rome

This thesis has been typeset by LaTeX and the Sapthesis class.

Author's email: niccolo.cocciaglia@uniroma1.it

Abstract

Nonequilibrium phenomena display such diverse phenomenological properties that cannot be treated in a unified manner. Some of them, especially those of geophysical origin, are described by a large number of variables following complex dynamical laws, thus the need of simplified models is strongly felt. In this Thesis we aim at investigating nonequilibrium properties of two nonlinear dynamical models inspired by geophysical flows, the Lorenz96 model and the Sabra shell model, using effective tools from nonequilibrium statistical physics, namely asymmetric time correlations and response functions. We show that both indicators are able to detect the presence or absence of time irreversibility, visualize effectively the statistical fluxes where present, and ultimately provide an alternative perspective on the transport properties characterizing both systems, whether they are in- or out-of- equilibrium (namely with zero or non-zero forcing and damping, respectively).

Acknowledgments

This thesis would not have existed without the presence and support of several people.

First of all I thank my supervisors, Angelo and Massimo, who introduced me to the fascinating realm of turbulence. Angelo is responsible for the (partial) knowledge I have about nonequilibrium statistical mechanics, and his ability to explain complex topics with ease and clarity has been a source of inspiration. Massimo struck me since the beginning for his vast knowledge on turbulence (and on basically everything), and his caring presence and guidance during my Ph.D. has been invaluable. I feel very grateful for everything I learned from them during these three years, and for the concrete help they provided regarding the prosecution of my career.

I benefited much from interactions with the "TNT group", and I witnessed how joviality and scientific rigor can coexist naturally. Without a doubt I have to acknowledging Dario, with whom I have worked on the Lorenz96 model and whose passion and enthusiasm about physics gave me renewed motivation. I would also like to thank Marco, who showed a genuine interest in the studies we were doing and gave me useful suggestions for the thesis.

I thank the external referees, dr. Michele Buzzicotti and prof. Filippo De Lillo, for their feedbacks and interesting remarks.

Room 117 provided an ideal environment for doing research, and this is especially due to all the fellow Ph.D. students who came, stayed and went. I especially thank Francesco, my desk-neighbour: even though he was the one perturbing this ideal environment with his loud voice and silly jokes, his humor broke the monotony of a day at the office, and we supported each other during the bittersweet life as a researcher.

During these three years I met wonderful young researchers in the turbulence community, with whom I exchanged ideas and from whom I learned many new things. I thank André, Andrea, Chiara, Francesco, Pierpaolo, Silvia, Simone and Xander for their precious friendship, and for the good times we spent at conferences.

I would like to express my gratitude to Luca Biferale's group at Tor Vergata of for having welcomed me for the past months. I really learned a lot from discussions with Luca and Alessandra, and I must thank Fabio for sharing with me part of his infinite knowledge on computer science and advanced computing.

Life does not have much meaning without friends and affections. To the 'physics-related' friends with whom I shared my years as a student in Rome: even though we took different roads and some of them do not live in Rome anymore, it is always a special moment when we find an occasion to meet again and catch up on each others' lives. Thank you Benedetta, Christian, Davide, Elisa and Tiberio for the beautiful moments we had (and will continue to have). All other, 'physics-unrelated', friends have an equally important place in my heart. To the friends in Rome, in Abruzzo and to those who emigrated elsewhere: thank you for simply everything.

Finally, my family. I feel deeply fortunate and proud to have been raised in the family I have. Thank you for having allowed me to follow my passions without any conditioning, for the love you have given me and for your persistent support. Thank you mom and dad, Roberta and Lorenzo, all the grandparents, Cristiano and Grazia, little Edoardo, cousins, uncles and aunts: this thesis is dedicated to all of you.

Contents

Chapter 1

Introduction

Many successful physical theories possess a certain degree of universality: their mathematical framework, even if originally aimed at modelling and studying a specific phenomenon, has a much broader range of applicability and turns out to work even for different systems. Naturally this range is limited: some level of similarity has to exist between the phenomena we want to describe using a given theory. In this respect, equilibrium statistical mechanics has a high degree of universality [1]. However, the same thing cannot be said about nonequilibrium statistical mechanics. A unified approach to treat off-equilibrium processes is still lacking, and it often happens that concepts and considerations developed for a given phenomenon appear ineffective when a generalization is attempted. Some approaches of broad validity are nonetheless available: entropy balance considerations, Fokker-Planck-like equations, perturbative studies, just to cite a few [2, 3]. The overall picture is that, while equilibrium processes all fall into the realm of validity of equilibrium statistical mechanics, on the other hand nonequilibrium processes cannot be grouped into a unified class, and each specific system must be dealt with independently. Rephrasing the famous incipit of "Anna Karenina" by Tolstoj, we can say that *all equilibrium systems share quite similar features, each non-equilibrium system has its own peculiarity.*

A common feature of nonequilibrium processes is their time irreversibility [2]. Frequently this property is illustrated in the form of an "arrow of time": a cube of ice left at room temperature will inevitably melt, the vacuum in a sealed bag is filled by air when it is opened, and in both examples the time-reversed process is never observed. In other cases the irreversible nature is less evident, and physical quantities may display a stationary behaviour even if they are subject to source and sink terms: a situation usually referred to as Non-Equilibrium Steady State (NESS) [4] or persistent nonequilibrium [5]. A notable example of this behaviour is found in the total kinetic energy measured in a stirred viscous flow, which despite the action of an external forcing and dissipation behaves as a stationary signal due to delicate balances [6].

Understanding and identifying nonequilibrium processes is a central problem in modern statistical mechanics [3]. The problem can indeed be tackled from different perspectives and using different methods: in this Thesis, the guiding principle has been the observation and analysis of the temporal, statistical asymmetries

displayed by nonequilibrium systems, absent instead in equilibrium ones, often triggering transfer processes among the degrees of freedom; a principle that provides remarkable relations with the underlying physics, as we observed for models inspired by turbulent and atmospheric flows exploiting asymmetric time correlations and response functions. Revealing the irreversible nature of a physical system by only looking at available measurements in time of some observables can represent a major challenge, especially if the dynamics that produced the signals is unknown or the observations cover only a part of the whole system [7]. The possibility to discriminate an equilibrium regime from a nonequilibrium one is of extreme importance: knowing that a system is in thermal equilibrium gives access to the solid methods and tools of equilibrium statistical mechanics, that often allow a complete understanding of the average properties since the probability distribution is known. Conversely, when out of equilibrium, the situation is more diversified. Some nonequilibrium systems are recognized from basic statistical properties - for instance, we will see in the Thesis that the Lorenz96 model [8] is described by variables showing non-zero expected values in the viscous formulation, that become zero in the inviscid case. Others require higher-order moments to ascertain the absence of equilibrium - for instance, we will also see that the shell variables of the Sabra model [9] display symmetric pdf's, either in the viscous or the inviscid case, yet suitable third-order moments permit the identification of statistical fluxes in the dissipative model and their absence in the conservative model. After all, third-order moments have a crucial role in systems whose evolution laws present quadratic nonlinearities: given some relevant quadratic quantity, its rate of change is mainly ruled by cubic terms if the system cannot be linearized.

Common techniques used for detecting and studying nonequilibrium properties look for (temporal, spatial, causal, etc.) "asymmetries" in the system [10, 11, 12]. It is known that the detailed balance condition is broken out of equilibrium, and the non-equivalence between transition probabilities generates non-zero statistical fluxes among the degrees of freedom [2]. Sometimes these fluxes are quite obscure quantities from a physical perspective, but in some cases they reflect transport properties of characteristic observables (energy flux, electric current). The most widespread technique, closely related to the concept of irreversibility, is to measure the entropy production rate of the system (or proxies of it), indicating how far it is from statistical equilibrium [13, 4]. In its most used definition, the entropy production rate compares the probabilities of forward-in-time trajectories with that of time-reversed ones. Statistical equilibrium implies a symmetry of such probabilities, while broken time-reversal invariance yields a positive entropy production. However this quantity is hard to compute in general - and only in a few cases, e.g. Gaussian processes, it can be computed analytically - and it provides just a global indication (a non-negative number) about the system's nature. An alternative approach is represented by Thermodynamic Uncertainty Relations (TURs) [14], establishing a link between the entropy production and the first two cumulants of the fluctuations of any kind of current measured in the system, and providing lower bounds for the entropy production. Other two effective methods, even if less known, exist for characterizing nonequilibrium processes, and they will constitute the main tools employed in this Thesis. Asymmetric time correlation functions [15] allow to observe the lack of time-reversal invariance starting from suitable time signals, providing

further information about currents and exchange properties. Non-diagonal (or cross-) response functions [16] reveal causal dependencies among the degrees of freedom, highlight transfer mechanisms, and their relaxation properties determine the statistical nature of the system.

Out-of-equilibrium phenomena can be observed everywhere around us. Correctly describing their behaviour requires the careful determination of the coupling between system and environment, determining the influence the latter exerts on the former - but also viceversa. Geophysical processes (having in mind as prototypical examples fluid turbulence and atmospheric circulation) owe their phenomenology to external drivings which can have different origins: radiation from the Sun, mechanical stirring, heat sources and so on [17]. The magnitude of their effect on the system cannot be neglected: as an example, in most fluid mechanics experiments we can say that the major energy contribution derives from external forcings. In other contexts, instead, the opposite may happen: the influence of the environment is minimal, so that it can be either removed altogether, in the crudest approximation, or treated as a small corrective term [18]. Energy dissipation is another phenomenon that cannot be neglected in realistic geophysical systems: at the microscopic scale irreversible transformations of internal energy into heat take place [19], and at long enough times they would bring the system to a state of rest if energy supplies were absent.

The joint action of external drivings and viscous dissipation, besides advection, buoyancy, pressure variations, non-inertial forces (Coriolis) and others, determines very complex dynamical features. Furthermore, the multiscale nature of geophysical processes makes it necessary, for a good modelization, to resolve time- and length-scales encompassing several orders of magnitude. To give an idea, in the atmosphere turbulent fluctuations at the millimeter scales, lasting a few seconds, coexist with long-lived waves with typical wavelengths of thousands of kilometers and lasting up to months [20]. To reproduce and predict these phenomena with computer simulations one must decide between two alternative approaches. One is to integrate directly the continuum equations with spatial and temporal discretization schemes, that should satisfy the requirements imposed by the length and time scales - namely small enough timestep and grid spacing, but also large integration time and spatial extension - at the expense of an enormous computational cost [21]. The other is to exploit simplified versions of the dynamical equations, in which a considerable reduction in number of degrees of freedom and computational cost is attained, but discarding some features of the original system [22, 20]. The second approach led to many celebrated models: the random walk reproducing Brownian motion, the Drude model for electrical conductivity, the Hopfield model for associative memory in neural networks[1], and many more others. The study of reduced geophysical models, often described by ODEs instead of PDEs, paved the way to important discoveries, enabled to reach extreme regimes that could not be attained by Direct Numerical Simulations (DNS), and also attracted the interest of the mathematical community [23, 24]. Often, neglecting some details in the physical description of a phenomenon proved to be useful for identifying the most fundamental aspects

[1]John J. Hopfield was awarded the 2024 Nobel prize in Physics for the development of this model and the relevance it had *for foundational discoveries and inventions that enable machine learning with artificial neural networks.*

governing the underlying processes [25].

The work presented in this Thesis aims at detecting and characterizing irreversible and, generally, nonequilibrium properties in systems of geophysical and hydrodynamical origin. In order to accomplish this, simplified yet nontrivial models have been employed: the Sabra shell model [9] for turbulence and the two-scales Lorenz96 model [8] for atmospheric circulation. Their evolution equations share a similar structure, that in terms of a generic phase-space vector $\boldsymbol{x}$ read:

$$\frac{d\boldsymbol{x}}{dt} = Q(\boldsymbol{x}, \boldsymbol{x}) + F(\boldsymbol{x}) - \nu\,(\boldsymbol{c} \cdot \boldsymbol{x}) \ ,$$

in which Q is a quadratic function coupling a triplet of variables, F a linear term that may include forcing, and the last is a linear damping term, written separately in terms of a time-independent vector $\boldsymbol{c}$ with positive entries and a positive constant ν. They will be used as testing-grounds for analyzing the effectiveness of the two alternative indicators of statistical nonequilibrium mentioned before. These are asymmetric time-correlation functions [15], that may be expressed in terms of suitable time correlations $C(\tau)$ as:

$$\psi(\tau) = C(\tau) - I[C(\tau)] \ ,$$

with $I[\cdot]$ indicating the time-reversal operator, and non-diagonal response functions [16]

$$R_{A,B}(t) = \frac{\overline{\delta B}(t)}{\delta A(0)}$$

measuring in time the average displacement of an observable B caused by a perturbation on observable A. The choice of using reduced models comes from several reasons: the interest in their nonequilibrium nature was predominant over their adherence to physical reality (let us point out that in both models, despite the very small number of degrees of freedom, the key features of the physical phenomena are well reproduced); the added possibility to perform long numerical computations on a single PC; the nonlinear structure of the evolution equations, for which analytical results are hard to find and computer simulations represent the first option to obtain useful information. The present study evidenced how the characteristic transport properties observed in turbulent fluids and atmospheric flows, nicely reproduced by the two models, are clearly revealed by both indicators. Furthermore, unlike entropy production rate that is inherently a global quantity, they allow to investigate also temporal and "spatial" nonequilibrium properties, and do not present serious technical difficulties in their computation.

This Thesis is structured as follows:

Chapter 2 gives a pedagogical introduction to the main statistical features of nonequilibrium systems. Parallelisms, but especially differences, are drawn between equilibrium and nonequilibrium statistical physics [26], and it is pointed out how irreversible systems can be divided into two classes: 'transient' and 'persistent' nonequilibrium processes. The former are characterized by irreversible behaviour only for a limited amount of time before relaxing to an equilibrium state: examples include diffusion of a gas from an initial small region, or two bodies of different temperatures

put in contact and eventually reaching a common equilibrium temperature [27]. The latter are kept out of equilibrium indefinitely by external drivings, or by intrinsically time-irreversible internal mechanisms: one may think about Non-Equilibrium Steady States (NESS) [4], but also about turbulent fluids and the atmosphere since they are subject to perpetual forcing and dissipation [20]. Afterwards, an overview of key results about macroscopic irreversibility follows, starting from Boltzmann's pioneering results [28], passing through nonequilibrium thermodynamics [29, 27] and arriving to modern topics such as entropy production and fluctuation relations [10, 30]. Finally, practical approaches allowing to detect the absence of statistical equilibrium, that were mentioned before, are properly described. Specifically, we will analyze the general properties of entropy production rate, asymmetric time correlations and response functions; also the Fluctuation-Dissipation Relation (FDR) [16] is discussed at the end. A pedagogical case-study accompanies these theoretical descriptions, showing operatively the behaviour of these functions in a minimal discrete-time Gaussian model that can be either in or out of equilibrium by varying a single parameter, and for which analytical results are found. We point out that time correlations and response functions will be actively used in the rest of the Thesis, while the entropy production rate has been avoided for the reasons explained before.

Chapter 3 deals with time-irreversibility and the characterization of transport properties in the two-scales Lorenz96 model [8]:

$$\begin{aligned}\frac{dX_n}{dt} &= X_{n-1}(X_{n+1} - X_{n-2}) - \nu_1 X_n + F - \frac{hc}{b}\sum_{k=1}^{K} y_{n,k} \\ \frac{dy_{n,k}}{dt} &= cby_{n,j+1}(y_{n,j-1} - y_{n,j+2}) - c\nu_2 y_{n,k} + \frac{hc}{b}X_n \ ,\end{aligned}$$

in which the X_n's are a set of slow variables while the $y_{n,k}$'s are fast variables, with $n = 1, \ldots, N$ and $k = 1, \ldots, K$. First the meaning of this simplified model is understood in the context of atmospheric predictability studies, and the main properties that contributed to make its fortune in different research areas are outlined. After that the original contribution is presented, in which the nonequilibrium indicators mentioned above are computed in both 'viscous' (with positive ν_1, ν_2 and F) and 'inviscid' models (with $\nu_1 = \nu_2 = F = 0$). The former is an out-of-equilibrium driven-dissipative system and has been extensively studied [31, 32, 33, 34] (see especially [35] for a survey of different applications), whereas the latter is conservative, thus in statistical equilibrium, and only a few studies are found in the literature [20]. We saw how large fluctuations of the asymmetric time correlations in the viscous model, absent in the inviscid one, reveal the presence of time-reversal symmetry breaking. Response functions allow to observe that such asymmetry can be traced in the propagation of traveling waves along the degrees of freedom. The effect of perturbations crossing from one scale to another is also shown and interpreted. Using the model as a prototypical example, we proceeded to demonstrate how the measurement of the average deviation from stationarity of a generic observable cannot provide many indications about the features of the perturbing agent (in some cases, not even the origin of the disturbance can be guessed): this is especially relevant in climate studies. This work is the result of a collaboration with Dr. Dario Lucente [36].

Chapter 4 is devoted to the study of the direct energy cascade in three-dimensional turbulent fluids from the perspective of nonequilibrium statistical mechanics. As a minimal model of 3D turbulence the Sabra shell model [9] is employed, whose equations mimic the spectrally-truncated Navier Stokes equation and read:

$$\dot{u}_n = i\left[ak_{n+1}u^*_{n+1}u_{n+2} + bk_n u^*_{n-1}u_{n+1} - ck_{n-1}u_{n-2}u_{n-1}\right] - \nu k_n^2 u_n + f_n \ .$$

For the sake of completeness, the Chapter starts with an introduction to hydrodynamic turbulence [19]. Ideal fluids are then briefly described, and their connection with equilibrium statistical physics is explained [37]. A section is dedicated to Kolmogorov's statistical theory of homogeneous isotropic turbulence [6], followed by a description of the multifractal approach [38] introduced for explaining intermittency and anomalous scaling. Reduced turbulent systems called 'shell models' are later discussed [39, 40], delineating in particular the properties of the Sabra shell model. The second part of the Chapter presents the original contribution, in which both viscous and inviscid Sabra models (the latter roughly reproducing a truncated Euler flow) are investigated. Asymmetric time correlations, besides the behaviour already observed in the Lorenz96 model, give further insights into the energy exchanges taking place among shell variables, that in the viscous case are consistent with a cascade of energy towards small scales. Further properties about time irreversibility are studied in terms of moments of the local powers and their anomalous scaling laws, which are rationalized in terms of the multifractal model. Response functions display different trends in the two cases: in the inviscid it is consistent with an energy-preserving dynamics, while in the viscous the presence (and direction) of a statistical flux among the variables is detected. Afterwards we analyze the viscous Sabra model when forced at intermediate scales, and not at large scales as customary. An interesting coexistence of equilibrium (at smaller shells) and nonequilibrium (at larger shells) properties is observed, as revealed by spectra and fluxes and confirmed by both nonequilibrium indicators. This work was done in collaboration with my supervisors Prof. Angelo Vulpiani and Dr. Massimo Cencini and published in *Physical Review E* [41].

Finally, Chapter 5 is dedicated to conclusions and perspectives of the Thesis.

The thesis is supplemented by some Appendices in which technical material is presented, in particular Apps. A and F expand the derivation of some formulas and results discussed in the core text, App. B provides theoretical background and App. C some information on the numerics. Appendices D and E, instead, contain additional discussions on specific topics.

Chapter 2

Irreversibility and nonequilibrium statistical physics: an overview

In this Chapter we aim at giving a brief introduction to the vast field of nonequilibrium statistical mechanics, with special emphasis on the practical methods for quantifying the "distance" from equilibrium in a system. We shall start with a quick recap of equilibrium statistical physics, before entering into the realm of nonequilibrium phenomena. The pioneering work of Boltzmann regarding macroscopic irreversibility, which set the path for most of later developments, is then treated, with a focus on Boltzmann's equation and the related H-theorem. An account of post-Boltzmann developments in the field of nonequilibrium thermodynamics and irreversibility follows. The Chapter ends with a description of the main tools, used in this thesis, that are able to detect the absence of statistical equilibrium, either revealing the breaking of time-reversal invariance or the presence of statistical fluxes.

2.1 Equilibrium and nonequilibrium statistical mechanics

2.1.1 A primer on equilibrium physics

Systems in thermal equilibrium are characterized by measurable macroscopic properties that remain unchanged in time (for instance temperature, pressure, density), despite the complex and unpredictable molecular dynamics taking place at the microscopic scale. In the second half of the XIX century the connection between microscopic and macroscopic world was still unclear: chemistry and thermodynamics existed only as independent fields.

The desire to predict the macroscopic behaviour of a large system starting from the microscopic laws of its basic constituents moved three eminent scientists, Maxwell, Boltzmann and Gibbs, to introduce a novel physical approach in which probability theory and statistics played key roles. Central in the new field of *equilibrium statistical mechanics* is the understanding that the macroscopic state of a system, called *macrostate* and defined by the measured values of thermodynamic quantities,

can be obtained from several different microscopic states, or *microstates*, described e.g. by all positions and momenta of the elementary constituents of the system. Formally, a microstate is a point in a high-dimensional space called *phase space*, and the microscopic evolution of the system is described by a curve in phase space. Microstates and macrostates are characterized by extremely different length and time scales: indeed, macroscopic properties are obtained from a coarsening procedure - i.e. computing time and space averages - on the corresponding microstates [42].

The most "likely" macrostates are the ones that are in correspondence with a comparatively larger number of microstates: this is quantified by the famous Boltzmann's law of entropy [18]:

$$S = k_B \ln W \ , \tag{2.1}$$

stating that the thermodynamic entropy S of a system grows with the number of microstates W yielding that macrostate. It represents a link between the macroscopic and the microscopic description of a thermodynamical system. These notions can be also transposed to phase space, by saying that a set of microstates leading to a frequently observed macrostate occupies a large portion of the available phase space. Therefore, thermodynamic equilibrium states are characterized by high entropy and by a huge number of associated microstates.

A formal probabilistic framework was introduced by means of the concept of *statistical ensembles*: our ignorance about the system's microstate is quantified by a probability density function $\rho(\boldsymbol{x}, t)$ describing the probability of finding a microstate in proximity of $\boldsymbol{x}$ at time t. Classical examples are the microcanonical, canonical and grand canonical ensembles, devised for describing, respectively, isolated systems, closed systems exchanging energy with a thermal reservoir and open system exchanging also matter.

A fundamental result that can be derived from equilibrium statistical mechanics is the *generalized equipartition theorem* [18]. Considering a system described by an Hamiltonian $H(\boldsymbol{x})$, the theorem reads:

$$\langle x_i \frac{\partial H}{\partial x_j} \rangle = \delta_{ij} k_B T \ , \tag{2.2}$$

in which the brackets indicate an ensemble average over the phase-space distribution. Substituting $x_i = p_i$, $x_j = p_i$ and summing over i yields the classical energy equipartition theorem found in kinetic theory: $\langle E \rangle = \frac{3}{2} N k_B T$, where $\langle E \rangle$ is the mean kinetic energy, N the number of particles and T the temperature of the gas.

The formalism of the ensembles always assumes a state of equilibrium due to mutual interactions between particles (even when not explicitly included in the Hamiltonian, some form of interaction must be assumed) and to the fact that the system of interest is, besides in the microcanonical framework, coupled to a larger reservoir of energy and/or particles. But the introduction of a phase-space density is a very general procedure, that may be applied even to systems which have little or no relationship to thermodynamics. In these cases the presence of a reservoir is not guaranteed, with the consequences that nontrivial macroscopic behaviour, not accountable with an equilibrium probability density, may emerge. We are entering the realm of *nonequilibrium physics*, which will be discussed in the next Paragraph.

2.1.2 Introducing time: nonequilibrium statistical physics

Systems in statistical equilibrium basically follow a common macroscopic behaviour: considering a closed system (i.e. exchanging energy but not matter with the environment) we can say that, whatever its initial condition, the system will relax to an equilibrium state characterized by the same temperature T of the reservoir it is in contact with, and by an average total kinetic energy that, according to the equipartition theorem, will be proportional to T [18]. The microstates which are "visited" in phase space give rise to macroscopic observables that are slightly-fluctuating variables around a mean, stationary value. Time is basically irrelevant in thermalized states: a measurement made around time t will not be that dissimilar from one performed around time $t + \tau$, even if $\tau \gg 1$. The macrostate can be effectively specified by providing the mean value $\langle A_i \rangle$ and the standard deviation σ_{A_i} of a set of thermodynamic variables A_i, where expected values could be obtained from empirical time averages.

A different approach altogether is necessary for those cases in which there are no reservoirs yielding a relaxation process in the system. In real life, most systems are free to exchange energy and matter with their environment. For instance, there exist in nature different processes that are subject to random *external forces*, with magnitude and orientation abruptly changing in time. The effect of a stochastic driving force on a system is completely dissimilar to that of a reservoir: at each timestep the phase-space coordinate is displaced in a random direction, and with a high probability it will be driven far from the high-dimensional manifold that represents the set of equilibrium states. Another natural mechanism that prevents to reach a thermalized state is *dissipation*. Like external forcings, also irreversible dissipative processes do not allow energy conservation, and generally their manifestation in phase space consists in the presence of a trivial stable fixed point where $\boldsymbol{p}_i = 0 \ \forall \, i$, generally acting like a basin of attraction for all initial conditions. It is trivial that the process of dissipation (of energy, for instance) has nothing in common with thermodynamic equilibrium, and the time dependence of the process is useful for estimating the rate of decay of a generic phase-space quantity. This limited-in-time nonequilibrium behaviour, which can also be found in diffusive systems characterized by relaxation to equilibrium, is dubbed *transient nonequilibrium*.

One could infer from the above discussion that the action of an external driving and the presence of macroscopic irreversibility is always associated to non-stationary values of physical observables. While this is generally true if the two processes do not act simultaneously - the former providing energy to the system and the latter removing it - it happens that in driven-dissipative systems a Non-Equilibrium Steady State (NESS) [4] is spontaneously reached, which is the outcome of a balance between the average input and the average output of energy (or some other quantity). This behaviour can be named *persistent nonequilibrium* since a NESS is maintained indefinitely, as long as the sources and sinks of energy continue to operate. It is generally said that an open system exists in a state away from equilibrium even when it reaches its steady state [4]. As a consequence, certain measurements performed when the mechanical and thermodynamical nature is not known cannot allow to discriminate between equilibrium and nonequilibrium, since even in the latter there

are physical observables which are statistically stationary, as in thermal equilibrium. As an example we point out the case of hydrodynamic turbulence, which will be studied in Chapter 4: if an external stirring acts on a viscous fluid the aforementioned balance between energy input and output is established, in such a way that the total kinetic energy merely fluctuates around a constant value, and any observable has a stationary statistics.

One of the trademark features of nonequilibrium is the presence of nonzero *currents* in the system. Notable examples in physics are: the electric current, representing the average displacement of charged particles in a preferred direction; the energy flux in turbulence, carrying energy from the large forced lengthscales down to the dissipative small scales; the heat current, observed in presence of a gradient of temperature in a macroscopic object. Speaking in more general terms, such currents are all manifestations of the same microscopic condition, called "broken detailed balance".

The concept of *detailed balance* originated from Markov systems, which in their most accessible version describe the discrete-time evolution of a system characterized by a finite number of accessible states $i = 1, \dots, N$ with initial probability distributions $(p_1(0), \dots, p_N(0))$. Also known are the (constant) transition probabilities q_{ji} from state i to state j. This is the only known information about the past state given the present state, i.e. Markov processes have a finite (usually 1-step) memory. Considering instead the time variable to be continuous, the probability density of state i evolves according to the Master Equation:

$$\frac{dp_i(t)}{dt} = \sum_{j \neq i} \left[-p_i(t) q_{ji} + p_j(t) q_{ij} \right] \ . \tag{2.3}$$

Let us point out that this equation, which can seem quite abstract, is very useful in chemistry when substituting the concentration of the i-th component to p_i and the reaction rates constants to q_{ji}: it yields the Law of Mass Action in chemical kinetics [4] describing the dynamics of a chemical reaction between N components. The detailed balance condition is verified when an invariant distribution $(\pi_1, \dots, \pi_N)$ exists which satisfies:

$$\pi_j q_{ij} = \pi_i q_{ji} \ , \tag{2.4}$$

meaning that the probability to have a transition from a state to another is equivalent to that of the reverse transition. Notice that if detailed balance (2.4) holds then $p_i(t) = \pi_i \ \forall\, i$ are stationary solutions of (2.3), which under specific conditions are also asymptotic solutions of the Master Equation. In conclusion, this type of system is said to be in equilibrium if and only if there exists an invariant distribution $(\pi_1, \dots, \pi_N)$ and the system satisfies the detailed balance condition (2.4).

On the other hand, the violation of detailed balance determines the absence of statistical equilibrium. In the same terms as before, if a system has an invariant distribution $(\pi_1, \dots, \pi_N)$ but for some i, j $\pi_j q_{ij} \neq \pi_i q_{ji}$ holds, then it is said to be in a nonequilibrium steady state (NESS) [4]. It can happen that the asymmetry between transition probabilities has visible effects at the macroscopic level, like in the previously mentioned examples of electric current, energy cascade and heat flux. Indeed the dissimilarity between forward-in-time and backward-in-time transitions determines a common nonequilibrium indicator, the entropy production rate [10, 30].

This and other tools which allow to detect time irreversibility and nonequilibrium will be discussed in Section 2.3.

Meanwhile, in the next Section we shall describe a historical issue in nonequilibrium physics, the emergence of macroscopic irreversibility, stressing Boltzmann's contribution to the resolution of this paradoxical phenomenon and then exploring some modern developments (from the beginning of XX century to the first years of the XXI) in the study of irreversible processes.

2.2 Macroscopic irreversibility: Boltzmann and beyond

Most thermodynamical processes are of irreversible nature, as ruled by the second law of thermodynamics. However, the microscopic laws governing them (either classical or quantum-mechanical) are invariant under time reversal. Then, how can time-irreversible phenomena arise at the macroscopic scale? The reconciliation of this apparent paradox is attributed to Boltzmann and his "H theorem" at the end of the XIX century. Notable developments in the XX century include the study of irreversible phenomena, such as heat flow and electric current, and their mutual influence (Onsager relations) [29]. Also, entropy and its rate of change assumed a central role in nonequilibrium physics, specifically the understanding that the Entropy Production Rate (EPR) is an invaluable tool for characterizing time-irreversibility [26, 10]. In the 90's a novel line of research started focusing on the asymmetry shown by entropy fluctuations, which led to the discovery of several Fluctuation Theorems [30]. These works, and further studies focusing on small systems (polymers, molecular machines, nanoprocessors), are nowadays included in the novel field of Stochastic Thermodynamics [30, 43]. In this Section we will give an outline of these above-mentioned developments, to provide a general (and historical) overview on the topic of macroscopic irreversibility.

2.2.1 Boltzmann's H theorem

With the aim of understanding the process of relaxation to equilibrium of an ideal N-particle gas, Boltzmann studied the time evolution of the one-particle distribution function $f(\boldsymbol{r}, \boldsymbol{v}, t)$, with $(\boldsymbol{r}, \boldsymbol{v}) \in \mathbb{R}^6$ denoting the microstate of a single particle and such that $f(\boldsymbol{r}, \boldsymbol{v}, t)\, d\boldsymbol{r}d\boldsymbol{v}$ represents the fraction of molecules in the small phase-space volume $d\boldsymbol{r}d\boldsymbol{v}$ at time t. Starting from the microscopic equations of motion, and assuming to discretize the velocity variable such that f_i represents the probability of finding the velocity in the region i into which the continuum space has been split, we obtain:

$$\frac{df_i}{dt} = \sum_{k,l,j} f_k(t)\, f_l(t)\, W_{(k,l)\to(i,j)} - \sum_{k,l,j} f_i(t)\, f_j(t)\, W_{(i,j)\to(k,l)} \ . \tag{2.5}$$

This represents a discretized version of the celebrated *Boltzmann equation*. The r.h.s. is the collision term, giving a positive contribution if binary collisions yield one particle with velocity in region i, and a negative one if a particle from that region changes its velocity. The terms $W_{(k,l)\to(i,j)}$ denote the collision rate from state (k, l) to state (i, j), and the density of the two-particle state is substituted by the product of single-particle densities, according to the *molecular chaos* hypothesis.

Boltzmann realized that this law allowed to predict the asymptotic behaviour of a generic initial velocity distribution. Introducing the H-function (or functional)

$$H(t) = \sum_i f_i(t) \ln f_i(t) \tag{2.6}$$

it can be shown [28] to be a non-increasing function, namely:

$$dH(t)/dt \leq 0 \ . \tag{2.7}$$

This result, known as *H-theorem*, implies an asymptotic approach of f_i towards a stationary probability distribution, satisfying the equality in Eq. (2.7). This asymptotic distribution, from the constraint imposed by the theorem, is proved to be exactly the Maxwell-Boltzmann one.

Despite the several simplifying assumptions, the theorem provided a justification to the time-irreversible nature of relaxation processes despite being described, at the microscopic level, by time-symmetric laws. However it also yield seemingly paradoxical consequences, even in contradiction with well-established mathematical laws:

- Zermelo pointed out that Poincaré's recurrence theorem should imply, at some point, an increase of the H-function close to its initial value. This objection was dismissed by Boltzmann by noticing that the recurrence time T_R, in macroscopic systems, is so large to be practically unreachable. A rough estimate of T_R indeed showed that, in a cubic centimeter of gas at ambient pressure and temperature, the recurrence time is incredibly larger than the age of the universe.

- Loschmidt, on the other hand, noticed that upon inversion of the velocity components the H-function should retrace its history, and thus increase towards its initial value. Boltzmann responded by pointing out that the H-function is not perfectly monotonic. Fluctuations also generate small and short-timed increases, but the crucial point is that $H(t)$ remains non-increasing on average, with a probability of decreasing that is larger the more the p.d.f. is distant from the Maxwell-Boltzmann distribution.

Boltzmann's work contributed to bridge the gap between mechanics and thermodynamics, particularly in understanding that it is impossible to recover irreversibility only from mechanical laws. Macroscopic irreversibility turns out to be an emerging phenomenon, which requires specific conditions to manifest itself: a very large number of interacting particles - or generally degrees of freedom - and proper initial conditions. Furthermore, a single macroscopic evolution can in principle evolve "against" the arrow of time, but this event has a probability to occur so tiny that, in practical terms, it will never be observed.

2.2.2 Irreversible processes and Onsager relations

The first steps towards extending the classical thermodynamic formalism to irreversible processes were taken, naturally, in the vicinity of equilibrium. For small deviations from equilibrium it is possible to use the hypothesis of *local equilibrium*:

the system of interest is made of small "mass elements" for which the entropy per unit mass, s, is the same function of macroscopic variables (e.g. internal energy, specific volume, mass fraction) as happens in the equilibrium case [27]. A direct consequence is that for such mass elements the first law of thermodynamics remains valid.

In a general framework of nonequilibrium thermodynamics [27, 44], the state of the system is defined by a set of extensive variables $\alpha_1, \ldots, \alpha_n$ that can be quantities like volume, energy, electric charge. We assume that thermodynamic functions are completely determined by the specification of the α's[1]. The entropy S is thus written as a function of these variables, namely:

$$S = S(\alpha_1, \ldots, \alpha_n) = S(\boldsymbol{\alpha}) \ . \tag{2.8}$$

Its maximum S_0 is reached when the variables assume their equilibrium values $\alpha_i = \alpha_i^0$, i.e. $S_0 = S(\alpha_1^0, \ldots, \alpha_n^0)$. Let us now define the *thermodynamic forces* (or affinities) as:

$$X_i = \frac{\partial S}{\partial \alpha_i} \ , \tag{2.9}$$

which measure the tendency to move towards equilibrium, and the corresponding *fluxes* (or rates) as:

$$J_i = \frac{\partial \alpha_i}{\partial t} \ . \tag{2.10}$$

The latter ones can be flows of matter, heat, electricity, etc. The entropy change due to a small fluctuation about equilibrium $\delta\boldsymbol{\alpha} = (\boldsymbol{\alpha} - \boldsymbol{\alpha}^0)$ can be expanded in Taylor series:

$$\Delta S \equiv S - S_0 = -\frac{1}{2} \sum_{i,j} s_{ij} \delta\alpha_i \delta\alpha_j + \mathcal{O}(\alpha^3) \ . \tag{2.11}$$

The linear term is zero because $\partial S/\partial \alpha_i|_{\boldsymbol{\alpha}^0} = 0$ (remember that entropy is stationary at equilibrium) and we have defined $s_{ij} = -\partial^2 S/\partial\alpha_i \partial\alpha_j|_{\boldsymbol{\alpha}^0}$. We know that $\Delta S \leq 0$, therefore the symmetric matrix s_{ij} is a positive-definite form. Neglecting higher order terms consists in assuming that fluctuations are Gaussian: as a matter of fact, Boltzmann's law of entropy (2.1) can in principle be inverted to give a measure of the probability of a thermodynamic state knowing its entropy. It follows that:

$$P(\boldsymbol{\alpha}) \propto e^{\Delta S/k_B} \propto \exp\left(-\frac{1}{2k_B} \sum_{i,j} s_{ij} \delta\alpha_i \delta\alpha_j \right) \ . \tag{2.12}$$

The end result is the following: small fluctuations of a thermodynamic variable about equilibrium follow a multivariate Gaussian distribution centered at the equilibrium value.

Let us point our attention to the thermodynamic forces (2.9) and the fluxes (2.10). From the discussion above we know that, at thermodynamic equilibrium, $X_i = 0 = J_i$ for any thermodynamic quantity. Furthermore, well-established phenomenological equations assert that the fluxes are linear functions of the thermodynamic forces [27]: the most notable are Fick's law of diffusion, Fourier's law of heat conduction

[1] The assumption of local equilibrium is necessary for defining thermodynamic functions.

and Ohm's law of electric conduction. They all quantify the physical phenomenon according to which a localized dynamic quantity tends to move naturally towards regions with less presence of such quantity (i.e. an evolution towards a maximum entropy configuration). Moreover, linear laws involving cross-effects between different phenomena have been observed: thermoelectric phenomena, in which an electromotive force generates a heat flux and a temperature gradient produces an electric current, have been known since the middle of the XIX century, while the Soret effect, consisting in diffusion in presence of a temperature gradient, is accompanied by the reciprocal Dufour effect, where heat flow is caused by a concentration gradient [27]. Formally, these phenomena can be written as a linear system relating fluxes and forces, like:

$$J_i = \sum_j L_{ij} X_j \ , \tag{2.13}$$

or:

$$X_i = \sum_j R_{ij} J_j \ . \tag{2.14}$$

The matrices L and R, whose entries are generally named "phenomenological coefficients", are such that $LR = I$, I being the identity matrix. This is a known result in linear algebra.

It is conceivable that in some particular cases the relationship between flows and forces may not be linear, but in a limited range close to equilibrium one may assume the linear relation to retain its validity. It happens indeed that ordinary transport phenomena like heat and electric conduction are linear even under rather extreme experimental conditions, whereas chemical reactions must be described by nonlinear laws [27].

Despite the enormous difference in the physical nature of this cross-phenomena, there were already strong evidences that the phenomenological coefficients displayed peculiar symmetries. Thomson, in 1854, analyzed various thermoelectric phenomena characterized by an electric current J_1 and a heat flow J_2 driven, respectively, by an electromotive force X_1 and by a force X_2, associated to heat, proportional to (minus) the temperature gradient. The interference between the two processes yields linear relations of the type (2.13) or (2.14), with $i, j = 1, 2$. Thomson, using thermodynamic reasoning and conservation laws, and adding further assumptions, was able to determine the relation [27]: $R_{12} = R_{21}$. In words, it means that when the electric current J_1 is influenced by the temperature gradient $\propto X_2$, then the heat flux J_2 is also influenced by the electromotive force X_1 through the same phenomenological coefficient $R_{12} = R_{21}$. This was the first *reciprocal relation* found in cross-phenomena, but unfortunately the line of thought applied for Thomson's special case proved to be ineffective for other irreversible processes. A generalization of this relation encompassing all nonequilibrium processes alike was long sought without success, until in 1931 Onsager [29] adopted a microscopic approach and proved that all reciprocal relations are in fact a consequence of the invariance of the microscopic equations of motion under time reversal.

The derivation is not very lengthy, and proceeds as follows [45]. Retrieving the notation used from Eq. (2.8), and assuming without loss of generality that $\boldsymbol{\alpha}^0 = (0, \ldots, 0)$, implying that $\delta\boldsymbol{\alpha} = \boldsymbol{\alpha}$, we are interested in the time correlation between delayed fluctuations of the α's, of the type: $\overline{\alpha_i(t)\alpha_j(t+\tau)}$, where the

overbar denotes a time average on the variable t. On the other hand, the correlation $\overline{\alpha_j(t)\alpha_i(t+\tau)}$ differs from the previous one only by the temporal order of the fluctuations, or by the substitution $\tau \to -\tau$. Microscopic reversibility is then expressed by:

$$\overline{\alpha_i(t)\alpha_j(t+\tau)} = \overline{\alpha_j(t)\alpha_i(t+\tau)} \ . \tag{2.15}$$

Subtracting $\overline{\alpha_i(t)\alpha_j(t)}$ from both members of the equation, dividing by τ and taking the $\tau \to 0$ limit leads to:

$$\overline{\alpha_i(t)\dot{\alpha}_j(t)} = \overline{\alpha_j(t)\dot{\alpha}_i(t)} \ . \tag{2.16}$$

An observation is needed here: the time derivative has to be intended as a quotient of finite differences, because the value of τ cannot be smaller than a characteristic molecular time τ_0 of the same size of the time interval between molecular collisions. Substituting the linear relations (2.13) for $J_i \equiv \dot{\alpha}_i$ into (2.16) we get:

$$\sum_k L_{jk}\overline{\alpha_i(t)X_k(t)} = \sum_k L_{ik}\overline{\alpha_j(t)X_k(t)} \ . \tag{2.17}$$

Assuming ergodicity, the correlations appearing in (2.17) are equivalent to the expected values of $X_i\alpha_j \equiv \frac{\partial \Delta S}{\partial \alpha_i}\alpha_j$ on the probability distribution $P(\boldsymbol{\alpha}) \propto e^{\Delta S/k_B}$, with ΔS the entropy variation (w.r.t. equilibrium) caused by fluctuations in the α's. A fairly easy computation of this integral allows to find: $\overline{X_i\alpha_j} = -k_B\delta_{ij}$, in which a Kronecker delta appears. This is the last ingredient needed, because a substitution into (2.17) yields: $-k_B\sum_k L_{jk}\delta_{i,k} = -k_B\sum_k L_{ik}\delta_{j,k}$, i.e.:

$$L_{ji} = L_{ij} \ . \tag{2.18}$$

These are the Onsager relations we sought.

The extension to systems violating microscopic reversibility (e.g. in the presence of an external magnetic field or of Coriolis forces) is not trivial. The so-called Onsager-Casimir relations can be obtained reverting, besides time and velocity, also the direction of the invariance-breaking agent (e.g. magnetic field and angular velocity, respectively), but this action would generate a separate system. Nonetheless, a generalized time-reversal symmetry that lead to the usual reciprocal relations was recently devised [46]. The further extension to continuous system adds formal difficulties, as elucidated in [27] for various applications.

2.2.3 Entropy production and fluctuation relations

The way the entropy of a generic thermodynamic system changes over time allows to characterize its statistical nature: as we already saw, the unconstrained evolution would bring the system towards a state of maximum entropy. Unlikely (far-from-equilibrium) initial conditions are characterized by a low entropy, so the relaxation to equilibrium is accompanied by a positive entropy production.

The variation of entropy dS in a physical system can be written as the sum of two terms [27]:

$$dS = d_eS + d_iS \ , \tag{2.19}$$

where d_eS is the exchange (or external) entropy, i.e. the entropy supplied to the system by the external environment, while d_iS, the internal entropy, is the entropy

produced inside the system. From the second law of thermodynamics we know that:

$$d_i S \geq 0 \ , \tag{2.20}$$

equality holding if the system performs reversible (equilibrium) transformations. On the other hand, the supplied entropy $d_e S$ can be positive, zero or negative depending on the interaction of the system with its surroundings. The Carnot-Clausius definition is: $d_e S = dQ/T$, dQ denoting the heat supplied to the system by the environment and T the absolute temperature at which heat is exchanged. It follows that for an isolated system (i.e. $d_e S = 0$) the inequality $dS \geq 0$ holds. Thus, in isolated systems entropy can never decrease, so the behaviour of such function provides a criterion for detecting the presence of irreversible processes.

It is useful to write the time variation of the entropy in terms of intensive and local quantities. We thus define the entropy per unit mass s (dependence on space coordinates will be omitted) as:

$$S = \int_V \rho \, s \, dV \ , \tag{2.21}$$

where ρ is the mass density and V the volume occupied by the system. The entropy exchange and entropy production can be supposed to evolve in time according to:

$$\frac{d_e S}{dt} = -\int_\Omega \boldsymbol{J}_s \cdot d\boldsymbol{\Omega} \qquad\qquad \frac{d_i S}{dt} = \int_V \sigma dV \ , \tag{2.22}$$

where Ω is the surface enclosing the volume V, $\boldsymbol{J}_s$ the (outward) *entropy flow* per unit area and unit time, and σ the *entropy production* per unit volume and unit time. The first equation is written as a continuity equation, since the exchange entropy variation is only due to contributions crossing the boundary of the system. The second means that internal entropy increments are generated by a source term. Using Gauss' theorem and substituting (2.21) and (2.22) into Eq. (2.19), we obtain:

$$\frac{\partial \rho s}{\partial t} + \boldsymbol{\nabla} \cdot \boldsymbol{J}_s - \sigma = 0 \ . \tag{2.23}$$

The above expression provides a balance equation for the entropy density ρs, in terms of a flux term and a source term. Furthermore, from (2.20) one has

$$\sigma \geq 0 \ . \tag{2.24}$$

Equations (2.23) and (2.24) are the local expressions for the second law of thermodynamics [27]. In deriving it, we have tacitly assumed that the laws (2.19) and (2.20), which are valid for macroscopic systems, also hold for infinitesimally small parts of the system.

Going back to the linear irreversible processes seen in the previous Paragraph, we can rewrite the time derivative of the entropy change (2.11) in terms of thermodynamic forces and fluxes:

$$\frac{d\Delta S}{dt} = -\sum_{i,j} s_{ij} \alpha_j \frac{d\alpha_i}{dt} = \sum_i X_i J_i \ , \tag{2.25}$$

where we used (2.10) and recognized that $-s_{ij}\alpha_j = \partial\Delta S/\partial\alpha_i \equiv X_i$. The entropy rate of change thus becomes a bilinear expression in the forces and fluxes appearing in the phenomenological equations.

The study of weak deviations from equilibrium is certainly relevant for large macroscopic systems, where thermal fluctuations are small. However, as the dimensions of the system decrease, fluctuations away from equilibrium begin to dominate the behavior and can lead to significant deviations from the system's average behavior [47, 30]. Small systems with this behaviour are ubiquitous in nature: one can think of magnetic domains, polymers, quantum dots and so on. These small systems operate away from equilibrium, dissipate energy continuously, and make transitions between steady states. They often exchange heat and work with their environment, so the concepts of entropy and entropy production emerge naturally, even though in small systems they will be highly-fluctuating quantities. We cannot expect entropy fluctuations to be Gaussian-distributed anymore: in far-from-equilibrium regimes positive increments of entropy must be dominant over negative ones, so an asymmetry in the fluctuations has to emerge

The research that initiated the study of fluctuations asymmetry in nonequilibrium systems was published in 1993 by Evans, Cohen and Morriss [48] for a two-dimensional thermostatted shear-driven fluid in contact with a heat bath. Supported by molecular dynamics simulations, they found that the ratio of the probability of finding a value of the shear stress and the probability of finding its opposite-signed value falls exponentially with the shear stress. Since this hydrodynamic quantity turns out to be proportional to a generalized rate of entropy production, they indirectly found the first Fluctuation Relation (FR) indicating an asymmetry between the probability of a positive and a negative entropy production rate σ in a NESS. The results indicated in any case a nonzero probability of violating the second law of thermodynamics. A transient FR valid for the relaxation towards the steady state was later found by Evans and Searles [49], while Gallavotti and Cohen [50] proved the steady-state FR for a large class of systems using concepts from chaotic dynamical systems. What became later known as Gallavotti-Cohen relation roughly states that, for the total entropy production ΔS [30]:

$$\frac{P(-\Delta S)}{P(\Delta S)} = e^{-\Delta S} \ , \tag{2.26}$$

where the total entropy production is computed for an arbitrary length of time. In words, the larger the negative fluctuations of entropy are, the exponentially-smaller their probability of occurrence will be.

The quantitative study of fluctuations and heat exchanges in mesoscopic systems, supported by FRs, later extended their scope and contributed to the establishment of Stochastic Thermodynamics [30, 43].

2.3 Tools for detecting and characterizing nonequilibrium

In this Section we aim at describing different tools and techniques that have proved to be much effective in detecting the absence of statistical equilibrium.

Arguably, there are two different approaches that one can follow to study deviations from equilibrium or, otherwise stated, there are two conditions to look for in a generic system. One is to analyze the behaviour of entropy changes, namely look for positive entropy production. Systems in equilibrium are found in a state of maximum entropy, hence the entropy becomes a time-independent quantity. On the other hand, system driven far from equilibrium are usually characterized by a lower-entropy regime, and their tendency to restore equilibrium yields a positive entropy production. This increase has a finite duration for transient nonequilibrium states, whereas it continues indefinitely in systems characterized by persistent nonequilibrium. In the latter case it has become very common to quantify how much a system is far from statistical equilibrium by measuring the value of the (positive) Entropy Production Rate (EPR). The second approach, more probability-based, exploits the breaking of the detailed balance condition (2.4), signaling an asymmetry in the transition probability between two states. Due to ergodicity, the relationship between conditional probability distributions can be mapped into a relationship between time correlation functions, thus the broken detailed balance is formally equivalent to an asymmetry between time correlation functions. From this idea, a descriptor of nonequilibrium, or better of broken time reversal invariance, is a class of Asymmetric Time Correlation Functions (ATCFs) [15, 51] that fluctuate around zero in the equilibrium case while showing nontrivial time dependencies in nonequilibrium regimes. Furthermore, the absence of detailed balance implies the existence of statistical fluxes (or currents), which often can be related to physical fluxes (energy or heat fluxes, electric current, etc.). The asymmetry created by the statistical fluxes is well captured by suitable Response Functions (RFs) [12, 11], since they are able to display the disturbances created by an external perturbation as they evolve and travel through the system. These indicators allow a good characterization of the nonequilibrium properties, as we will see when they will be used on the Lorenz96 and the Sabra models in Chapters 3 and 4, respectively. We will now proceed to delineate the main features of the above mentioned quantities: EPR, ATCFs and RFs.

2.3.1 Entropy Production Rate (EPR)

We have already met the EPR σ in Eq. (2.22), where it was defined as the source of "internal" (e.g. not caused by the environment) entropy change $d_i S$ per unit time and unit volume [27]. The second law of thermodynamics immediately implies that it is a non-negative quantity, as written in (2.24). Despite its clear thermodynamic origin and meaning, novel results in stochastic thermodynamics led to understand that EPR, just like many other thermodynamical concepts, could be given an alternative form if one follows the new interpretation of thermodynamic variables as stochastic ones, defined on individual microscopic trajectories.

Among the first investigations on this matter we find the one by Lebowitz and Spohn [10] on Markov processes, which preceded the birth of stochastic thermodynamics. Let us consider a continuous time Markov process with finite state space $\mathcal{S}$. Points in $\mathcal{S}$ are denoted by s. The process is determined by the rates $k(s, s') \geq 0$ for jumping from s to s'. We will call $\mu(s, t)$ the probability distribution of s at time t, such that any function f depending on phase space coordinates has an expected

value: $\langle f \rangle_{\mu(t)} = \sum_s \mu(s,t) f(s)$. The time evolution of $\langle f \rangle_{\mu(t)}$ is written as:

$$\frac{d}{dt}\langle f \rangle_{\mu(t)} = \sum_{s,s'} \mu(s,t) \left[k(s',s) f(s') - k(s,s') f(s) \right] \ , \tag{2.27}$$

and taking f to be a Kronecker delta selecting state s we obtain the Master Equation:

$$\frac{d\mu(s,t)}{dt} = \sum_{s'} k(s',s)\mu(s',t) - r(s)\mu(s,t) \ , \tag{2.28}$$

where $r(s) = \sum_{s'} k(s,s')$. The Gibbs entropy then reads:

$$S_G(\mu(t)) = -\sum_s \mu(s,t) \log \mu(s,t) \ . \tag{2.29}$$

Its rate of change can be written, using (2.28), in the form:

$$\frac{d}{dt} S_G(\mu(t)) = R(\mu(t)) - A(\mu(t)) \ , \tag{2.30}$$

where

$$R(\mu(t)) = \frac{1}{2} \sum_{s,s'} \left[k(s,s')\mu(s,t) - k(s',s)\mu(s',t) \right] \log \left[\frac{\mu(s,t)k(s,s')}{\mu(s',t)k(s',s)} \right] \geq 0 \tag{2.31}$$

and

$$A(\mu(t)) = \sum_{s,s'} k(s,s')\mu(s,t) \log \left[\frac{k(s,s')}{k(s',s)} \right] \ . \tag{2.32}$$

This splitting of the rate of change into a non-negative term R and a term A that is linear in μ leads us to identify the first as the entropy produced by the stochastic jumps per unit time - i.e. the EPR - and the second as the entropy flow that can have either sign. Notice the evident similarity between (2.23) and (2.30).

On the other hand, defining a trajectory (or history) of the process $t \to s_t$, the authors define the quantity:

$$W(T, \{s_t, 0 \leq t \leq T\}) = \int_0^T \sum_{s,s'} w_{s,s'}(t) \, dt \tag{2.33}$$

with $w_{s,s'}(t)$ denoting a sequence of δ-functions, located at those times t when s_t jumps from s to s', with weight $w(s,s') = [\log k(s,s') - \log k(s',s)]$. This means that if the trajectory visits in succession the states $s_0, s_1, \ldots, s_n$, where s_0 is the state at time 0 and s_n the state at time T, then:

$$W(T, \{s_t, 0 \leq t \leq T\}) = \log \left[\frac{k(s_0,s_1)}{k(s_1,s_0)} \cdots \frac{k(s_{n-1},s_n)}{k(s_n,s_{n-1})} \right] \ . \tag{2.34}$$

This quantity was named by the authors *action functional*.

Now, when the system reaches the steady state - and $\mu(t)$ converges to the stationary measure $\overline{\mu}$ - we have that $dS_G(\overline{\mu})/dt = 0$ and the entropy flow balances the entropy production rate. It means that:

$$\lim_{T \to \infty} \langle W(T)/T \rangle = R(\overline{\mu}) = A(\overline{\mu}) \ . \tag{2.35}$$

Thus the quantity on the l.h.s. is equivalent to the EPR in the steady state. Let us remark that $R(\overline{\mu}) = A(\overline{\mu}) = 0$ if $k(s, s')$ satisfies detailed balance with the invariant measure $\overline{\mu}(s) \sim e^{-V(s)}$, i.e.

$$e^{-V(s)}k(s, s') = e^{-V(s')}k(s', s) \ . \tag{2.36}$$

This happens because each term of the sum in the definition of R vanishes, and by (2.35) also A will be zero. Thus, as expected, the EPR is zero in statistical equilibrium (where detailed balance holds), whereas it is strictly positive in nonequilibrium regimes (where entropy exchanges with the environment may also be observed).

It is quite interesting to notice that the action functional (2.34) compares forward-in-time and backward-in-time trajectories. The probability of a trajectory $\{s\} = \{s_0, \ldots, s_n\}$ is:

$$P(\{s\} = \overline{\mu}(s_0)p(s_0, s_1) \cdots p(s_{n-1}, s_n) \tag{2.37}$$

when starting in the stationary measure $\overline{\mu}$. Indeed we can rewrite (2.34) as:

$$W(n, \{s\}) = \sum_{j=1}^{n} \log \left[\frac{p(s_{j-1}, s_j)}{p(s_j, s_{j-1})} \right] = \log \frac{P(\{s\})}{P(\mathcal{R}\{s\})} \ , \tag{2.38}$$

having denoted with $\mathcal{R}\{s\}$ the time-reversed trajectory $\{s_n, \ldots, s_0\}$. Indicating with $P(T, \{s\})$ the probability of a trajectory of length T passing through the states $\{s\}$, the EPR reads:

$$\sigma \equiv R(\overline{\mu}) = \lim_{T \to \infty} \frac{1}{T} \left\langle \log \frac{P(T, \{s\})}{P(T, \mathcal{R}\{s\})} \right\rangle \ . \tag{2.39}$$

This constitutes a direct link between time reversal invariance and statistical equilibrium signalled by zero entropy production rate.

A stochastic thermodynamics approach to entropy production was later pointed out by Seifert [13, 30] in the context of small systems with intrinsic randomness. To convey the idea, the author considers the motion $x(t)$ of a colloidal particle of mobility γ subject to an external force $F(x, t)$ and evolving according to a Langevin equation. The associated Fokker-Planck equation [52] can be written as well for $p(x, t)$, the probability to find the particle at x at time t, and reads:

$$\partial_t p(x, t) = -\partial_x j(x, t) = -\partial_x \left[\gamma F(x, t) - D\partial_x \right] p(x, t) \ , \tag{2.40}$$

where $j(x, t)$ is the probability current defined by the r.h.s. while D is the diffusion coefficient of the particle. A "trajectory-dependent" entropy for the particle is defined as:

$$s(t) = -\log p(x(t), t) \ , \tag{2.41}$$

where the probability is evaluated along the stochastic trajectory. The rate of change of the *total entropy* s_{tot}, sum of the entropy of the system s and that of the medium s_m, can be explicitly computed. Exploiting Eq. (2.40) and using thermodynamic relations one obtains:

$$\dot{s}_{tot}(t) \equiv \dot{s}_m(t) + \dot{s}(t) = -\frac{\partial_t p(x, t)}{p(x, t)}\bigg|_{x(t)} + \frac{j(x, t)}{D\, p(x, t)}\bigg|_{x(t)} \dot{x} \ . \tag{2.42}$$

At this point, the entropies should be averaged over the probability distributions for comparing them to the familiar quantities of nonequilibrium thermodynamics. Omitting the details, the author found that:

$$\langle \dot{s}_{tot} \rangle = \int dx \, \frac{j^2(x,t)}{D\, p(x,t)} \geq 0 \ , \tag{2.43}$$

where equality holds in equilibrium only. Furthermore:

$$\langle \dot{s}_m \rangle = \int dx \, \frac{F(x,t) j(x,t)}{T} \ , \tag{2.44}$$

where T is the temperature.

EPR, however, has important downsides: it is a difficult quantity to measure in real systems since it requires the complete knowledge of the states visited by the system, and can be explicitly calculated only in limited cases (e.g. Markov processes). Furthermore it is a global quantity, so it cannot provide any information about the physical currents between degrees of freedom. Even though EPR will not be used in the numerical studies of this thesis, we thought it useful to discuss its derivation and meaning since it is very widespread in both nonequilibrium thermodynamics and stochastic processes.

A case study part 1/3: EPR

We think it is worthwhile, before moving on, to present a simple example where analytical calculations can be performed to find an explicit expression of the EPR (2.39). The 2nd and 3rd part of such study, about response functions and the fluctuation-dissipation relation, will be continued in Paragraphs 2.3.3 and 2.3.4. The toy model we will use is a slight variation of the one introduced in [12]: it is a linear map with reciprocal interactions between three variables, x_t, y_t and z_t, in which one single coupling has a variable weight that can break the reciprocity. The discrete-time evolution reads:

$$x_{t+1} = a x_t + (a - \beta) y_t + a z_t + \eta_t^{(x)} \tag{2.45a}$$

$$y_{t+1} = a x_t + a y_t + \eta_t^{(y)} \tag{2.45b}$$

$$z_{t+1} = a x_t + a z_t + \eta_t^{(z)} \ . \tag{2.45c}$$

where η_t's are independent Gaussian variables with zero mean and unitary variance, while a and β are assigned constants. In compact form, the evolution can be written as:

$$\boldsymbol{s}_{t+1} = A \boldsymbol{s}_t + B \boldsymbol{\eta}_t \ , \tag{2.46}$$

where $\boldsymbol{s}_t = (x_t, y_t, z_t)^T$, $\boldsymbol{\eta}_t = (\eta_t^{(x)}, \eta_t^{(y)}, \eta_t^{(z)})^T$, $B = I_3 \equiv \mathrm{diag}(1,1,1)$, and

$$A = \begin{pmatrix} a & a-\beta & a \\ a & a & 0 \\ a & 0 & a \end{pmatrix} \tag{2.47}$$

The former parameter is fixed to $a = 0.4$, while β is varied from 0 to a. The value of a was chosen to ensure that the spectral radius of A was less than one $\forall \beta$, thereby

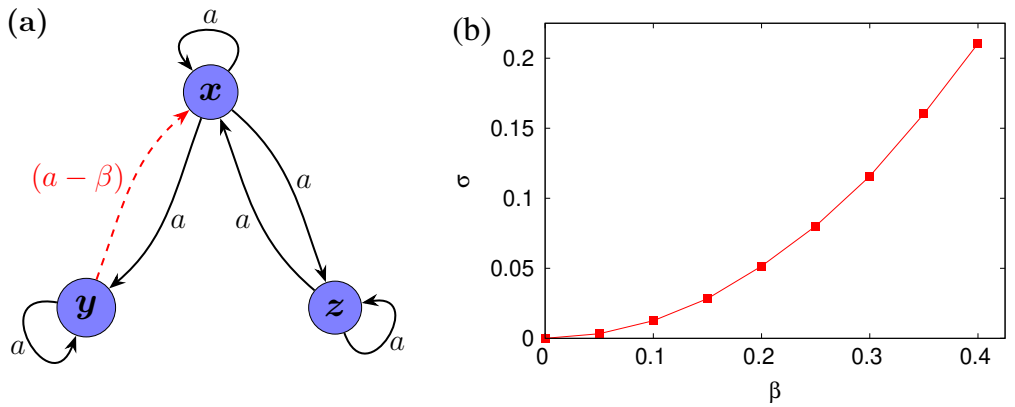

Figure 2.1. Panel (a): sketch of the model, where black solid arrows refer to a value $a = 0.4$ in the interaction matrix, while the red dashed arrow has a weight $(a - \beta)$, with β a free parameter. Panel (b): Entropy production rate, computed from (2.49), at varying β. Reciprocal interactions ($\beta = 0$) yield $\sigma = 0$, while a breaking of the interaction symmetry ($\beta > 0$) translates into a positive EPR.

avoiding a diverging dynamics. A sketch of the model is represented in Fig. 2.1a. The case $\beta = a$ is an example in which the behavior of two quantities, y and z, is influenced by a common-causal variable x; as a consequence, y and z are correlated even though they are not in causal relationship. On the other hand, if $\beta = 0$ all interactions are reciprocal, and A becomes a symmetric matrix.

For linear Gaussian processes, with either continuous or discrete time, several analytical results can be found [52]. Among them, an explicit formula of the EPR (2.39) can be written. Since our system (2.46) is Markovian, we only need to consider one time-step, namely:

$$\sigma = \left\langle \log \frac{P(\{\boldsymbol{s}_{t'}\}_t^{t+1})}{P(\{\boldsymbol{s}_{t'}\}_{t+1}^{t})} \right\rangle \ , \tag{2.48}$$

where the average is taken on $P(\{\boldsymbol{s}_{t'}\}_t^{t+1})$, the probability of the direct path $\boldsymbol{s}_t \to \boldsymbol{s}_{t+1}$. After expressing the above probabilities in terms of Gaussian distribution, the following expression is found:

$$\sigma = \mathrm{Tr}\left[(A^T B^{-2} - B^{-2} A) A C_0\right] = \mathrm{Tr}\left[(A^T - A) A C_0\right] \ , \tag{2.49}$$

in which $C_0 = \langle \boldsymbol{s}_t \boldsymbol{s}_t^T \rangle$, and in the last step we discarded the matrix $B^{-2} = I_3$. The complete derivation of (2.49) can be found in Appendix A. The values of the EPR at varying β are shown in Fig. 2.1b. As expected, for $\beta = 0$ we have no entropy production: all interactions are reciprocal ($A^T = A$) and detailed balance holds. Increasing the value of β we create an asymmetry in the system and bring it out of statistical equilibrium, resulting in a positive EPR. Let us notice that a non-zero EPR could have been obtained, besides for non-reciprocal interactions, also if the matrix B had non-identical elements on the diagonal, i.e. in presence of temperature gradients.

2.3.2 Asymmetric Time Correlation Functions (ATCFs)

In nonequilibrium systems one would like to understand how the (density, temperature, etc.) fluctuations are correlated in time, namely investigate the temporal coherence of a system. To this end one can introduce *time correlation functions* [26].

Let us denote with $\delta A(t)$ the instantaneous deviation or fluctuation of the observable $A(t)$ from its time-independent statistical average $\langle A \rangle$ (describing either an equilibrium state or a NESS), namely:

$$\delta A(t) = A(t) - \langle A \rangle \ . \tag{2.50}$$

Let us remark in passing that the average $\langle \cdot \rangle$ computed over a steady-state distribution can be intended also as a time average assuming ergodicity. While from the definition it trivially follows that $\langle \delta A \rangle = 0$, one can obtain interesting information by considering correlations between fluctuations at different times. This is computed, for two fluctuations at time 0 and time τ, as:

$$C(\tau) = \langle \delta A(0) \delta A(\tau) \rangle = \langle A(0) A(\tau) \rangle - \langle A^2 \rangle \ . \tag{2.51}$$

In an equilibrium system the correlations between dynamical variables at different times should depend only upon the separation between these times: equilibrium systems are by default stationary. Then:

$$C(\tau) = \langle \delta A(t) \delta A(t+\tau) \rangle \ . \tag{2.52}$$

An important consequence of stationarity is that C is an even function:

$$C(\tau) = \langle \delta A(0) \delta A(\tau) \rangle = \langle \delta A(-\tau) \delta A(0) \rangle = C(-\tau) \ . \tag{2.53}$$

For $\tau = 0$ and $\tau \to \infty$, considering that at large times the fluctuations will become uncorrelated, the time correlations behave as:

$$C(0) = \langle (\delta A)^2 \rangle \qquad\qquad C(\tau) \xrightarrow{\tau \to \infty} \langle \delta A(0) \rangle \langle \delta A(\tau) \rangle = 0 \ . \tag{2.54}$$

A widespread normalized form of correlation functions, that in statistics is called Pearson correlation coefficient, reads as:

$$\tilde{C}(\tau) = \frac{\langle \delta A(0) \delta A(\tau) \rangle}{\langle (\delta A)^2 \rangle} = \frac{\langle A(0) A(\tau) \rangle - \langle A^2 \rangle}{\langle A^2 \rangle - \langle A \rangle^2} \ , \tag{2.55}$$

and is such that: $\tilde{C}(0) = 1$.

Actually the type of correlations we just described are often called *time autocorrelation functions*, since they measure the statistical similarity of two delayed fluctuations of the *same* quantity A. In the more generic case of two different observables $A(t)$ and $B(t)$ one defines, as in (2.51),

$$C_{A,B}(\tau) = \langle \delta A(0) \delta B(\tau) \rangle = \langle A(0) B(\tau) \rangle - \langle A \rangle \langle B \rangle \ , \tag{2.56}$$

and we will call them *Time Correlation Functions* (TCF). Now the symmetry relation (2.53) becomes:

$$C_{A,B}(\tau) = C_{B,A}(-\tau) \ , \tag{2.57}$$

while the normalized form (2.55) reads:

$$\tilde{C}_{A,B}(\tau) = \frac{\langle \delta A(0)\delta B(\tau)\rangle}{\sqrt{\langle(\delta A)^2\rangle\langle(\delta B)^2\rangle}} = \frac{\langle A(0)B(\tau)\rangle - \langle A\rangle\langle B\rangle}{\sqrt{[\langle A^2\rangle - \langle A\rangle^2]\,[\langle B^2\rangle - \langle B\rangle^2]}} \ . \tag{2.58}$$

One sees that all quantities and relations found for autocorrelation functions are special cases of the general ones found for TCFs if $A = B$.

The relation (2.57) is expected to hold for any system in a stationary state: it is valid for both statistical equilibrium states and NESS's. On the other hand, time-reversibility implies that for any pair of observables A and B the identity:

$$C_{A,B}(\tau) = C_{B,A}(\tau) \tag{2.59}$$

holds. As a consequence, if two observables exist such that (2.59) is violated, then the system is in a nonequilibrium regime.

In a 1982 work, Pomeau [15] studied the behaviour of nonequilibrium fluctuations under time reversal. He noticed that, while the function $C(\tau)$ (Eq. (2.51)) is unchanged by the transformation $\tau \to -\tau$, being then insensitive to the direction of time, one could exploit the property (2.59) of $C_{A,B}(\tau)$ to devise other types of TCFs able to manifest the nonequilibrium nature (hence time-irreversibility) of the "signal" $A(t)$. Specifically, one defines Asymmetric Time Correlation Functions (ATCFs), depending only on the observable $A(t)$, that are exactly zero if the system is time reversible and which do not vanish if it is not invariant under time reversal. The general idea is to seek time correlations that change form under time reversal - this excludes simple autocorrelations of the type (2.51) - and exploit this change in form to construct an ATCF which is the difference between the forward and the time-reversed correlations. In general quadratic correlation functions, like the ones we described up to now, cannot reveal this asymmetry: higher-order correlations (at least cubic) must be employed.

Of course, different possible functions can be built using this procedure. The author suggested as examples the following third- and fourth-order functions:

$$\Psi_1(\tau) = \langle A(t)[A(t+2\tau) - A(t+\tau)]A(t+3\tau)\rangle \ , \tag{2.60}$$

$$\Psi_2(\tau) = \langle A^3(t)A(t+\tau) - A(t)A^3(t+\tau)\rangle \ . \tag{2.61}$$

Notice that the ATCFs are odd: $\Psi_i(\tau) = -\Psi_i(-\tau)$. Let us remark that Eqs. (2.60) and (2.61) are zero in equilibrium: this follows from microscopic reversibility, as we saw in Eq. (2.15). On the contrary, far from equilibrium the time-reversed TCF is not equivalent to the forward one, so the resulting ATCF will show a nontrivial behaviour. A peculiar property is that, for third-order functions such as (2.60) it is equivalent to study the ATCF of the observable $A(t)$ itself, as in the examples above, or that of the deviation $\delta A(t)$: the additional terms involving $\langle A\rangle$ all cancel out if stationarity holds. On the other hand, it can be shown that ATCFs from the fourth order above, computed for $\delta A(t)$, can be split into a linear combination of same- and lower-order ATCFs computed for $A(t)$.

One particular ATCF that will be used in the following studies is:

$$\Psi(\tau) = \langle A^2(t)A(t+\tau) - A(t)A^2(t+\tau)\rangle \ . \tag{2.62}$$

It is cubic, thus computing the correlation of the observable or of its fluctuation is the same. Furthermore, one can easily notice that the function $\Psi(\tau)$ is formally equivalent to:

$$\Phi(\tau) = \frac{1}{3}\langle [A(t+\tau) - A(t)]^3 \rangle \ . \tag{2.63}$$

Expanding the cube, we get: $\Psi(\tau) = \langle [A^3(t+\tau) + 3A^2(t)A(t+\tau) - 3A(t)A^2(t+\tau) - 3A^3(t)] \rangle / 3$. But the first and last term cancel out due to stationarity, so one has:

$$\Psi(\tau) \equiv \Phi(\tau) \ . \tag{2.64}$$

If we imagine $A(t)$ to be a physical time signal, like kinetic energy, electric current, temperature, then the correlation function $\Phi(\tau)$ has a clearer meaning than the less intelligible $\Psi(\tau)$: Eq. (2.63) measures the third moment of that quantity's variation after a finite time τ.

In Sections 3.3.2 and 4.5.1 we will investigate the behaviour of the ATCFs for the specific cases of the Lorenz96 model and the Sabra model, respectively. These studies have shown that the numerical computation of ATCFs is a delicate matter: since we are considering the difference of two TCFs, many cancellations of terms with opposite sign occur. In addition, spurious behaviour in the case of finite-size statistics (i.e. any numerical study) is often observed. These issues are discussed in Appendix D.

2.3.3 Response Functions (RFs)

Closed systems are not very common in nature: even less so are isolated systems, where not only matter but also energy cannot be exchanged with the external environment. Instead, the physical reality abunds of open systems, ranging from very large spatial extensions (Earth's atmosphere, but also solar systems and galaxies) to microscopic scales (cells, nanoprocessors). All of them are often subject to external perturbations, originating from the interaction with the outside environment and possibly causing a change of state in the system. After the displacement from the previously occupied state - which could have been an equilibrium state or a NESS - the system, if left undisturbed, tends to relax to the original stationary state[2]. In general the characterization of this relaxation process is not easy, but the hypothesis of weak perturbations allows to derive a meaningful relation connecting the deviation of a dynamical variable from its steady-state value to suitable correlation functions of that variable, computed on the unperturbed system. Systems weakly displaced from equilibrium are studied in the framework of *linear response theory*, and the relation between displacements - measured by RFs - and time correlations goes under the name of *Fluctuation-Dissipation Relation* (FDR) [53, 54, 16]. A concise description of both linear response theory and FDRs will follow in the next Paragraph, while in the present one the focus is on defining and pointing out the main features of RFs.

Response functions were originally introduced in the context of Hamiltonian systems [55]. Generally speaking, one can consider [16] a system described by the Hamiltonian $\mathcal{H}(\boldsymbol{P}, \boldsymbol{Q}, t) = \mathcal{H}_0(\boldsymbol{P}, \boldsymbol{Q}) - \mathcal{F}(t)A(\boldsymbol{P}, \boldsymbol{Q})$, where $\mathcal{H}_0(\boldsymbol{P}, \boldsymbol{Q})$ is the

[2]If the system can be in different possible steady states, e.g. dynamical systems with multiple attractors, the external perturbation could make the system jump from a steady state to another.

time-independent part, $(\boldsymbol{P}, \boldsymbol{Q})$ are the usual conjugated canonical variables, and the second term represents a time-dependent perturbation to the unperturbed Hamiltonian $\mathcal{H}_0$. In particular, $\mathcal{F}(t)$ is an applied field that couples to $A(\boldsymbol{P}, \boldsymbol{Q})$[3], and the linear response regime holds if $\mathcal{F} \ll 1$. Let us suppose to be interested in the effect of this external perturbation on an arbitrary function $B(\boldsymbol{P}, \boldsymbol{Q})$ of the phase-space variables. The deviation from its equilibrium value at time t will be called $\Delta B(t) = B'(t) - \langle B \rangle$, with B' indicating its value in the perturbed system. In the linear regime, some calculations (that can be found in the next Paragraph) show that the average of the displacement $\Delta B(t)$ can be written in the form:

$$\langle \Delta B(t) \rangle_p = \int dt' R(t, t') \mathcal{F}(t') \ . \tag{2.65}$$

The brackets $\langle \cdot \rangle_p$ formally indicate an average taken on the perturbed phase-space probability distribution, that can be expressed in terms of the equilibrium canonical distribution under the present assumptions. Here $R(t, t')$ is the RF, sometimes also called "generalized susceptibility". Of course, Eq. (2.65) represents the first term, linear in $\mathcal{F}$, of a Taylor expansion in which $\mathcal{O}(\mathcal{F}^2)$ terms and higher-order ones have been neglected.

The definition (2.65) implicitly provides a physical interpretation for $R(t, t')$ [26]. First of all, one notices that $\langle \Delta B(t) \rangle_p$ is a functional of $\mathcal{F}(t)$, thus the first nonvanishing term of the Taylor expansion of such functional at time t reads

$$\int dt' \, \frac{\delta \langle \Delta B(t) \rangle_p}{\delta \mathcal{F}(t')} \, \mathcal{F}(t') \ , \tag{2.66}$$

in which $\delta / \delta \mathcal{F}(t')$ denotes a functional derivative computed at time t'. Hence:

$$R(t, t') = \frac{\delta \langle \Delta B(t) \rangle_p}{\delta \mathcal{F}(t')} \ , \tag{2.67}$$

i.e. the RF represents the change in the average displacement at time t due to a change in the external disturbance at time t'.

Let us now move from generic perturbations to more specific cases. One instance is represented by "impulsive" disturbances, namely $\mathcal{F}(t) = \mathcal{F}_0 \delta(t - t_0)$. Inserting this form into (2.65) yields: $\langle \Delta B(t) \rangle_p = R(t, t_0) \mathcal{F}_0$. The RF is proportional to the average displacement when the perturbation is an impulse, and all other responses can be interpreted as linear combinations of this special case. There are two properties that follow from physical considerations. First, the response depends only on the time displacement from the instant when the disturbance happened, and not on the absolute times:

$$R(t, t') = R(t - t') \ . \tag{2.68}$$

Second, the system cannot respond before the disturbance is applied, a property known as *causality*:

$$R(t - t') = 0 \qquad \text{if} \ \ t - t' \leq 0 \ . \tag{2.69}$$

[3]For example, $\mathcal{F}$ might be an electric field that couples to the instantaneous dipole moments of the molecules in the system, in which case A is the total dipole, or polarization, of the system.

These properties transform Eq. (2.65) into:

$$\langle \Delta B(t) \rangle_p = \int_{t_0}^{t} dt' R(t-t') \mathcal{F}(t') \ , \tag{2.70}$$

having assigned time t_0 to the beginning of the perturbation.

However, there exist various systems that lack an Hamiltonian structure, whose evolution is often described by Ordinary or Partial Differential Equations (ODEs and PDEs, respectively). In such cases the definition of a RF slightly changes, even though it retains the usual significance [16]. For the sake of generality, now the perturbation is considered to act on a stationary state, that can be even of nonequilibrium type. For instance, let us consider a chaotic dynamical system, described by the ODE $\dot{\boldsymbol{x}} = f(\boldsymbol{x})$. Given an impulsive perturbation $\delta\boldsymbol{x}(0)$ of the state of the system $\boldsymbol{x}(0)$ at time 0, one can consider the Taylor expansion of the difference between the perturbed and unperturbed trajectories at time t, $\delta\boldsymbol{x}(t) = \boldsymbol{x}'(t) - \boldsymbol{x}(t)$. Component-wise, it reads:

$$\delta x_i(t) = \sum_j \frac{\partial x_i(t)}{\partial x_j(0)} \delta x_j(0) + \mathcal{O}(|\delta\boldsymbol{x}(0)|^2) \ . \tag{2.71}$$

Averaging over the initial conditions one obtains the following RF:

$$R_{j,i}(t) = \left\langle \frac{\partial x_i(t)}{\partial x_j(0)} \right\rangle \ . \tag{2.72}$$

The functions with $i = j$ are named *diagonal* (or *self*) RFs, while if $i \neq j$ they are called *non-diagonal* (or *cross*) RFs. While the former give valuable indications about the de-correlation times, the latter are particularly interesting in nonequilibrium settings because the influence of a perturbation on quantities other than the perturbed one allows to recognize the presence of statistical fluxes and to infer dependencies between degrees of freedom [12, 11]. We will see these non-diagonal RFs in action in Sections 3.3.3 and 4.5.2. In numerical settings, when one can actively manipulate the system, it is customary to perform perturbations of fixed amplitude such that the previous formula, substituting the derivative with the ratio of finite differences, amounts to:

$$R_{j,i}(t) = \frac{\langle \delta x_i(t) \rangle}{\delta x_j(0)} \ . \tag{2.73}$$

The numerical computation is straightforward. After perturbing the variable x_j at time $t = t_0$ with a small perturbation δx_j, one follows the separation $\delta\boldsymbol{x}(t|t_0)$ between perturbed and unperturbed trajectories up to a prescribed time $t_1 = t_0 + \tau$. At time $t = t_1$ the variable x_j on the reference trajectory is again perturbed with the same amplitude, and a new sample of $\delta\boldsymbol{x}(t|t_1)$ is obtained up to $t_2 = t_1 + \tau$. Repeating this procedure $M \gg 1$ times, and considering the average over initial conditions as an arithmetic average over these consecutive realizations, one evaluates for the variable x_i the following RF:

$$R_{j,i}(\tau) = \frac{1}{M} \sum_{k=0}^{M-1} \frac{\delta x_i(t_k + \tau | t_k)}{\delta x_j} \equiv \frac{\overline{\delta x_i}(\tau)}{\delta x_j} \ . \tag{2.74}$$

In the presence of chaos the two trajectories separate exponentially in time, therefore the response is the result of a delicate balance of terms that grow in time in different directions. It is best in any case to avoid large values of τ, since the statistical errors in the RFs grow exponentially as well. Indeed, a rough estimate of the error stemming from (2.74) is [56]:

$$\mathrm{err}(R_{j,i}(\tau)) \sim e^{L(2)\tau/2}/\sqrt{M} \ , \tag{2.75}$$

where $L(2)$ is the generalized Lyapunov exponent of order 2 (the definitions of Lyapunov Exponents and some related concepts, such as Generalized and Finite-Size Lyapunov exponents, can be found in Appendix B). We are not constrained to perturb and measure only the explicit phase-space variables: also functions of $\boldsymbol{x}$ can appear in both numerator and denominator of Eq. (2.72), and the formula is to be interpreted as a functional derivative, like we saw in (2.67).

A case study part 2/3: RFs

Here we will examine again the model described at the end of Paragraph 2.3.1 in order to show the effectiveness of response functions to detect causal relationship among variables. The setup of the model remains the same as before. The case $\beta = a$ represents a minimal example in which the behavior of two quantities, y and z, is influenced by a common-causal variable x; as a consequence, y and z are correlated even though they are not in causal relationship. Decreasing β from that value, the link from y to x becomes more and more important, and a causal connection from the former to the latter is established. The RF of interest is:

$$R_t^{yz} = \frac{\langle \delta z_t \rangle}{\delta y_0} \ , \tag{2.76}$$

by means of which we analyze the average effect that a perturbation on y_t, of size $\delta y_0 = 0.01$, has on the variable z_t.

The causal behaviour we anticipated clearly emerges from Fig. 2.2, in which the responses (2.76) are computed at varying β. When $\beta = a$ the variable y has no influence on x, and consequently neither on z: this is revealed by the RF computed in this case (black, bottom curve), namely a perturbation on y has zero effect on z. As β decreases the causal link from y to x acquires a nonzero weight that increases as β is lowered down to $\beta = 0$. In the figure the increased strength of the causal link is revealed by the larger peaks assumed by the RFs at decreasing β.

2.3.4 Addendum: Linear Response Theory and Fluctuation-Dissipation Relation (FDR)

The study of fluctuations, and of their relation with the response to external perturbations, has led to fundamental discoveries throughout the XX century. After Einstein's studies on Brownian motion, Onsager [29] introduced his *regression hypothesis* stating that the relaxation of a macroscopic nonequilibrium perturbation follows the same laws that govern the dynamics of fluctuations in equilibrium systems. This principle already contained the seed of the Fluctuation-Dissipation Relation (FDR) which was later embedded into the *linear response theory* by Kubo [55].

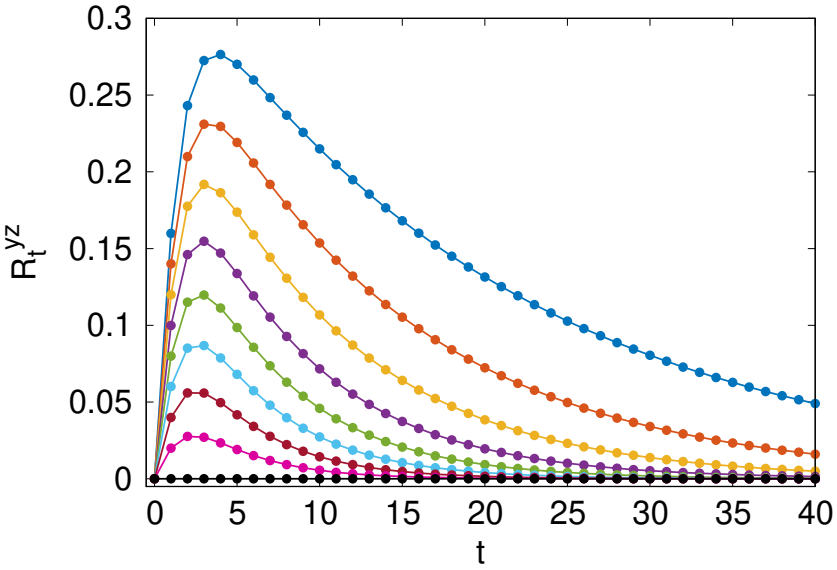

Figure 2.2. Response functions (2.76) at increasing β, from $\beta = 0$ (top, blue curve) to $\beta = a$ (bottom, black curve) with a step $\Delta\beta = a/8$. When $\beta = a$ the causal path from y to z is absent (see Fig. 2.1a), while this link is generated and increased in strength as β decreases to zero.

In the same Hamiltonian framework of Paragraph 2.3.3, the FDR expresses RFs in terms of time correlation functions computed at equilibrium. Remembering that the perturbed Hamiltonian is written as: $\mathcal{H}(\boldsymbol{P}, \boldsymbol{Q}, t) = \mathcal{H}_0(\boldsymbol{P}, \boldsymbol{Q}) - \mathcal{F}(t)A(\boldsymbol{P}, \boldsymbol{Q})$, Kubo's FDR reads as:

$$R_{A,B}(t) = \beta\langle \dot{A}(t')B(t)\rangle = -\beta\langle A(t')\dot{B}(t)\rangle \ , \tag{2.77}$$

where t' is the time of the perturbation, and angular brackets denote an equilibrium ensemble average.

The application of the FDR to real systems leads to meaningful relations among physical quantities. The first FDR, found long before the above general formula was obtained, is the celebrated Einstein relation between the diffusion coefficient D and the mobility μ for a colloidal Brownian particle. If V is the particle velocity - assuming 1D motion for simplicity - and the perturbing force is F, the mobility is defined by the relation: $\langle \Delta V\rangle = \mu F$, where the first term is the average deviation of the velocity caused by the disturbance. The Einstein relation reads:

$$\mu = \frac{D}{k_B T} \ , \tag{2.78}$$

and it provides a link between a property of the unperturbed system (the diffusion coefficient) and a measure of the system's reaction to a small perturbation (the mobility). Several similar relations exist that connect transport coefficients to equilibrium two-time correlations of a system. They are called *Green-Kubo relations*, and some of the most notable examples connect mobility to momentum time-correlation, shear viscosity to pressure tensor time-correlation, and electrical conductivity to electric current density time-correlation.

After Kubo's FDR, it was understood that a generalized FDR holds under rather general hypotheses for a vast class of systems with chaotic dynamics, also for non-Hamiltonian systems. To see this, let us consider a dynamical system described by the phase space vector $\boldsymbol{x} \in \mathbb{R}^N$, whose time evolution can be either deterministic or stochastic. We assume the system to be mixing, and the invariant probability distribution $\rho(\boldsymbol{x})$ to be smooth. The aim is to express the average response of a generic observable $B(\boldsymbol{x})$ to a perturbation $\boldsymbol{x} \to \boldsymbol{x} + \Delta\boldsymbol{x}$. The perturbed system is described by the distribution ρ', and expectation values with respect to the unperturbed and perturbed measures are denoted with $\langle\cdot\rangle$ and $\langle\cdot\rangle'$ respectively. Omitting the full derivation, which can be found e.g. in [16], the average deviation of B is expressed by:

$$\overline{\Delta B}(t) = -\sum_{j=1}^{N} \left\langle B(\boldsymbol{x}(t)) \frac{\partial \ln \rho(\boldsymbol{x})}{\partial x_j}\bigg|_{t=0} \right\rangle \Delta x_j(0) = \sum_{j=1}^{N} R_{x_j,B}(t) \Delta x_j(0) \ , \tag{2.79}$$

in which $\overline{\Delta B} = \langle B\rangle' - \langle B\rangle$, and the perturbation is applied at $t = 0$. The generalized FDR thus reads:

$$R_{x_j,B}(t) = -\left\langle B(\boldsymbol{x}(t)) \frac{\partial \ln \rho(\boldsymbol{x})}{\partial x_j}\bigg|_{t=0} \right\rangle \ . \tag{2.80}$$

Notice that the smoothness of ρ was necessary to compute the partial derivatives inside brackets. However many chaotic systems have strange attractors, whose invariant measure has a multifractal character, thus they are outside the range of validity of the generalized FDR. The problem can be circumvented by applying a small amount of noise that smoothens $\rho(\boldsymbol{x})$. Besides, projections from high-dimensional phase spaces to a low-dimensional one also allow to retrieve a smooth probability measure. It can be seen that Kubo's FDR for Hamiltonian systems reduces to a special case of the generalized FDR (2.80). Indeed, considering the usual canonical ensemble, one has that $\ln \rho = -\beta \mathcal{H}(\boldsymbol{P}, \boldsymbol{Q}) + \text{const}$. Using Hamilton's equation, the response on Q_k stemming from a perturbation on P_k becomes:

$$\frac{\overline{\Delta Q_k}(t)}{\Delta P_k(0)} = \beta \left\langle Q_k(t) \frac{dQ_k}{dt}\bigg|_{t=0} \right\rangle = -\beta \frac{d}{dt} \langle Q_k(t) Q_k(0)\rangle \ , \tag{2.81}$$

which is exactly Kubo's FDR (2.77).

A case study part 3/3: FDR

We will conclude here the study on the Gaussian linear model, Eq. (2.45) or (2.46), with a verification of the correspondence between response functions and a suitable combination of time correlations imposed by the FDR. It can be verified that in our model, but generally for Gaussian linear systems, the FDR amounts to:

$$R_t = C_t C_0^{-1} \ , \tag{2.82}$$

where $R_t^{ij} \equiv R_t^{s^{(j)} \to s^{(i)}}$, $C_t^{ij} = \langle s_0^{(j)} s_t^{(i)} \rangle$, indicating with $s^{(i)}$ the i-th component of the vector $\boldsymbol{s}$, and C_0 is the covariance matrix. The derivation of (2.82) can be found in App. A. We show in Fig. 2.3 the equivalence observed in our model between the

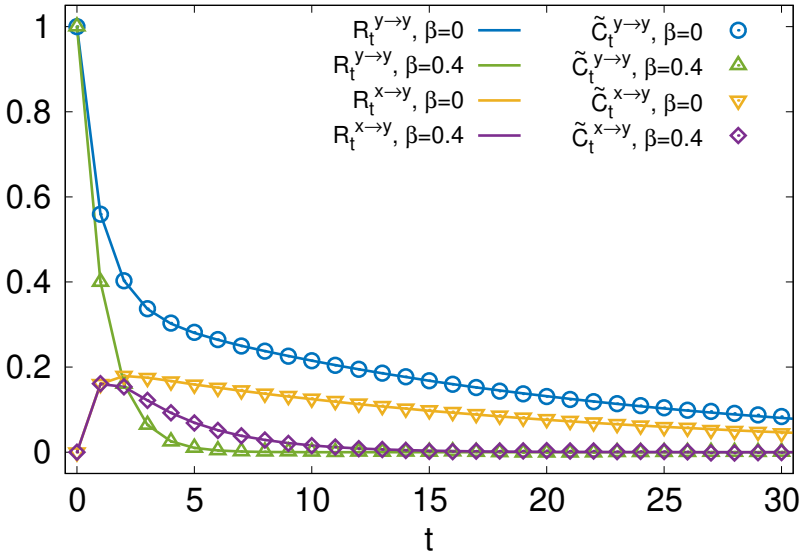

Figure 2.3. Test of the FDR. Colored lines: response functions. Symbols: combination of time correlations (matrix elements of $\tilde{C}_t \equiv C_t C_0^{-1}$). Either diagonal or non-diagonal matrix elements and equilibrium or nonequilibrium cases are shown, as in legend.

RFs and the combination of time correlations represented by the matrix product on the r.h.s. of (2.82). Colored lines are response functions, while symbols are matrix elements of $\tilde{C}_t \equiv C_t C_0^{-1}$: a perfect superposition of corresponding functions is clearly observed. Different cases are presented: diagonal and non-diagonal matrix elements, either in the equilibrium ($\beta = 0$) or the out-of-equilibrium ($\beta > 0$) case. This is to further remark that FDRs hold even far from statistical equilibrium.

Chapter 3

Nonequilibrium properties in the Lorenz96 model

In this Chapter a study on nonequilibrium properties of the two-scales Lorenz96 model is presented. Its importance in the context of geophysical phenomena, especially for studies about the predictability in atmospheric sciences, is highlighted in the first part, followed by an exposition of the main features observed by previous studies in both the single-scale and the two-scales versions of the model.

Then, the third Section contains the original work, devoted to a study of the nonequilibrium indicators that have been introduced in the previous Chapter. Interesting parallelisms are drawn between the model with forcing and linear damping, which is far from equilibrium, and the one without forcing and dissipation that is instead in statistical equilibrium.

3.1 The model and its context

The *predictability* of physical systems, characterized as the ability to predict the future state from present (but also past) observations, is a central problem in geophysical sciences. Different difficulties arise when tackling this topic. From a practical point of view, physical measurements cannot even provide an exact initial condition, since finite sensitivity in the instruments or truncation errors in computers always introduce a degree of uncertainty. This has dramatic consequences in *chaotic systems*, since an arbitrarily small variation of the initial condition causes the 'perturbed' trajectory to separate exponentially fast from the reference one. The evolution of real natural systems is indeed modelled - and approximated - by means of dynamical equations which often show a chaotic behaviour. This hinders the predictability of such systems: the "true" future state can be anyone among a plethora of diverging-in-time points stemming from very similar initial conditions. Furthermore, real systems are never really deterministic in their evolution, because the presence of some randomness in the evolution process (and in the modelling equations) must often be taken into account. For instance, a thorough discussion about the importance of thermal noise for correctly describing turbulence can be found in [57].

It is natural to associate the word "predictability" with the weather, since the

type of scientific predictions that most affect our everyday lives are, without a doubt, weather forecasts. However the atmosphere is a very complex system: its state is determined, zone by zone, by a large number of physical variables (such as pressure, temperature, wind velocity, air density) whose coupled evolution is described by complicated PDEs. The atmosphere is also a *multiscale* system [17]: its overall behaviour is the combined result of dynamical effects which range from sub-millimeter scale up to synoptic scales - of the order of thousands of kilometers. Even fluid turbulence displays this complex multiscale character, as will be described in the following Chapter. The chaotic nature of the atmosphere, accompanied by the difficulties met when trying to perform faithful numerical studies of its patterns, can only allow a finite predictability window before the errors exceed a chosen tolerance value. For this reason weather forecasts are considered accurate enough for a time window of 1-2 days, whereas they become much less reliable for larger time windows.

Quantitative estimations of the predictability times have historically relied on Lyapunov exponents [58] (see Appendix B). If the initial state of a system is known with (infinitesimal) accuracy δ, and we are interested in how long the state of the system can be predicted within a tolerance Δ, then the exponential amplification of the initial error provides the following estimate for the predictability time:

$$T_p(\delta, \Delta) = \frac{1}{\lambda_1} \ln\left(\frac{\Delta}{\delta}\right) \sim \frac{1}{\lambda_1} , \tag{3.1}$$

where the first Lyapunov exponent λ_1 appears. However, in multiscale systems the above naive estimate fails to account for the complex hierarchy of timescales involved, since λ_1 can only describe errors of the fastest scales. It proves necessary to analyze differently the various stages of the error evolution, in which different timescales alternate in dominating the overall behaviour [59]. In order to do so, the concept of Finite-Size Lyapunov Exponents (FSLEs) [60] was introduced. A concise description of these objects can be found in Appendix B.

Lorenz's interest in the predictability of geophysical fluid systems is evidenced by his celebrated 1969 paper [61], in which he aimed at determining quantitatively the range of predictability of Earth's atmosphere. From pairs of solutions originating from nearly identical initial conditions, he studied the ensemble-averaged error of the kinetic energy for different scales of motion, in which by "error" one means the difference in kinetic energy between the two solutions. The problem posed by the presence of different scales is substantial, since tiny errors on the smallest scales influence the uncertainty measured at the largest scales, the latter giving the predominant contribution to the overall error. In practice, the equation for the evolution of the error was derived from a model of a two-dimensional fluid in an infinite plane, suitably discretized in Fourier space. It is easy to notice how the modelization of complex dynamical phenomena is a very widespread topic in Lorenz's scientific production [25]: ever since the famous Lorenz63 model [62], whose influence on the fields of dynamical systems, geophysics and statistical mechanics are unprecedented, different other studies followed in which the behaviour of nontrivial physical systems was reduced, by means of simplifying assumptions, to a description in terms of much more tractable equations.

His 1996 work [8] can be considered as a convergence of the above-mentioned interests: the study of predictability of the atmosphere, but introducing and making

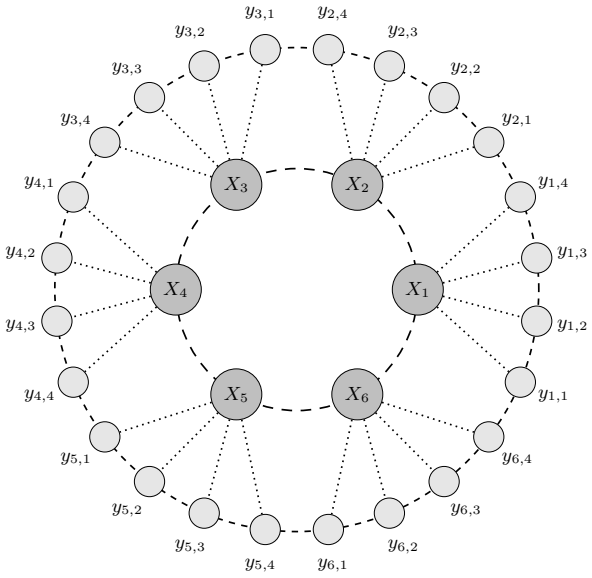

Figure 3.1. Schematic representation of the two-scales L96 model for $N = 6$ and $K = 4$.

use of a "rather crude" (in his own words) model of its dynamics. This model became known as Lorenz96, and in the following it will be abbreviated as L96. The single-scale L96 model is described by N variables $X_1, \ldots, X_N$ evolving according to the equations:

$$\frac{dX_n}{dt} = -X_{n-2}X_{n-1} + X_{n-1}X_{n+1} - \nu X_n + F \qquad n = 1, \ldots, N \ . \tag{3.2}$$

Periodic boundary conditions are imposed, namely: $X_{n+pN} = X_n,\ p \in \mathbb{Z}$. Broadly, the $\{X_n\}$ can be thought of as scalar atmospheric variables, such as temperature or vorticity, measured in N equidistant sites along a mid-latitude circle. The system is formally homogeneous, since cyclic site-translations do not change the dynamics. The resemblance with a geophysical system is confined to the presence of external forcing (F, independent on n), dissipation (the linear damping) and nonlinear interactions mimicking advection (the quadratic terms). The parameter $\nu = \{0, 1\}$, absent in the original formulation by Lorenz, can be used to turn on and off the damping term. The nonlinear terms conserve the total energy

$$\mathcal{E} = \frac{1}{2}\sum_{n=1}^{N} X_n^2 \ , \tag{3.3}$$

since it is easily shown that:

$$\frac{d\mathcal{E}}{dt} = \sum_{n=1}^{N} \left(F X_n - \nu X_n^2 \right) \ , \tag{3.4}$$

so that in absence of forcing and dissipation the total energy is a conserved quantity.

In the same publication, Lorenz introduced an extension of the previous model having two distinct timescales and a different spatial structure. Besides the X_n's,

further NK variables $y_{n,k}$ appear where $k = 1, \dots, K$, so that the coupled equations now read:

$$\frac{dX_n}{dt} = X_{n-1}(X_{n+1} - X_{n-2}) - \nu_1 X_n + F - \frac{hc}{b}\sum_{k=1}^{K} y_{n,k} \tag{3.5a}$$

$$\frac{dy_{n,k}}{dt} = cby_{n,k+1}(y_{n,k-1} - y_{n,k+2}) - c\nu_2 y_{n,k} + \frac{hc}{b}X_n \ . \tag{3.5b}$$

The periodic boundary condition $y_{n+pN,k} = y_{n,k},\ p \in \mathbb{Z}$ holds here as well, whereas on the second index we have the following connection rule: $y_{n,k+pK} = y_{n+p,k}$, which means that $y_{n,K}$ is the left neighbour of $y_{n+1,1}$, while $y_{n,1}$ is the right neighbour of $y_{n-1,K}$ for arbitrary n. In Fig. 3.1 we represent a sketch of the mutual dispositions and interactions among variables. Also Eq. (3.5b) displays an advection-like term and dissipation, while lacking an explicit forcing term. The coupling between X's and y's is mediated by the last term of both Eqs. (3.5), stating that a variable X_n directly interacts, with a coupling strength h, with the K variables $y_{n,k}$ having that same first index. It can be thought as a parametrization of the dynamics occurring at a spatial and temporal scale unresolved by the X variables. Also here fictitious viscosities ν_1, $\nu_2 = \{0, 1\}$ have been added. The parameters b and c quantify the disparity in amplitudes and timescales between the two scales: the variables y will fluctuate c times faster and show typical amplitudes that are b times smaller than those of the X's. For this reason the X's are often dubbed "slow" variables while the y's are "fast" variables. Let us notice that the fast variables are dynamically invariant only for translations of multiples of K sites (see Fig. 3.1), i.e. for $y_{n,k} \to y_{n,k+iK} = y_{n+i,k}$ with $i \in \mathbb{Z}$: otherwise stated, the invariance is for cyclic permutations of the first index while keeping the second fixed. Hence the two-scales L96 model is inhomogeneous. Here the total energy reads:

$$E = \frac{1}{2}\sum_{n=1}^{N}\left(X_n^2 + \sum_{k=1}^{K} y_{n,k}^2\right) \ , \tag{3.6}$$

so that its balance equation is

$$\frac{dE}{dt} = \sum_{n=1}^{N}\left(FX_n - \nu_1 X_n^2 - c\nu_2 \sum_{k=1}^{K} y_{n,k}^2\right) \ . \tag{3.7}$$

The forms of the coupling terms are chosen in order to give no contribution to the total energy balance, even though the coupling in Eq. (3.5b) must necessarily provide energy to the y's to balance the friction term and obtain a stationary state. In other terms, the main role of the coupling is to favor energy transfer between the two scales.

The L96 model, due to the simplified but mathematically-nontrivial structure, extended its influence beyond its original scope: either as the core of novel research or as a case study for applying new concepts, the model was employed likewise in physics [63, 64, 65, 66, 35], mathematics [67, 68, 69, 34] and geosciences [70, 71, 33].

3.2 Main features

In this Section we focus on the dynamical properties of the L96 model, noting the similarities with real geophysical flows and describing the types of solutions (fixed points, periodic or chaotic motions) they display when the parameters are varied. The properties that we will examine first refer to the single-scale model and to the structure of its evolution equation, while some additional features of the two-scales model are presented in the second part.

Single-scale L96 model

It can be readily verified by substitution that a trivial steady solution of (3.2) is: $X_1 = \cdots = X_N = F$. It had already been noticed by Lorenz in his first study [8] that the nature of the solutions depended parametrically on the forcing F and the system size N: he pointed out, without showing quantitative proofs, that as the forcing $F > 0$ increases the system's steady solutions transition from stable fixed points to periodic cycles and later to a chaotic behaviour.

A preliminary information about the regimes encountered at varying F is provided by a linear stability analysis [31, 20]. Substituting $X_n(t) = F + x_n(t)$, with x_n indicating a perturbation around the steady state, into Eq. (3.2) yields, at linear order:

$$\frac{dx_n}{dt} = F(x_{n+1} - x_{n-2}) - x_n \ . \tag{3.8}$$

Given the periodic and discrete "spatial" structure of the model, it is fruitful to apply a discrete Fourier transform to these perturbations, a standard procedure in solid-state physics to study lattice vibrations, defined as:

$$\hat{x}_q = \frac{1}{N} \sum_{j=1}^{N} x_j e^{-2\pi i j q/N} \ , \tag{3.9}$$

where $i = \sqrt{-1}$. This transformation entails that perturbations around the steady state, in liner approximation, assume a wave-like form. In terms of these Fourier coefficients (3.8) becomes:

$$\frac{d\hat{x}_q}{dt} = a_q \hat{x}_q \ , \tag{3.10}$$

with:

$$a_q = \left[\left(e^{2\pi i q/N} - e^{-4\pi i q/N} \right) F - 1 \right] \ . \tag{3.11}$$

Linear stability analysis then tells us that the steady state becomes unstable if $\mathrm{Re}(a_q) > 0$ for some q, that is when:

$$\cos(2\pi q/N) - \cos(4\pi q/N) > 1/F \ . \tag{3.12}$$

As expected, the instability condition only depends on the number of sites and on the forcing. One can compute that the factor $[\cos(2\pi q/N) - \cos(4\pi q/N)]$ has a maximum positive value equal to $9/8$ when $\cos(2\pi q/N) = 1/4$. This means that the steady solution becomes unstable with respect to waves of "wavelength" $N/q = 2\pi/\arccos(1/4) \simeq 5$ sites when $F > 8/9$.

The property of the single-scale L96 model that contributed substantially to its success in the geophysics community is the presence of a behaviour analogous to that of barotropic flows [20]. If we write x_j in the wave-like form

$$x_j = \sum_{q=1}^{N} A_q \exp\left(i\frac{2\pi jq}{N} - i\omega(q)t\right) \tag{3.13}$$

and substitute it into the linearized equation (3.8) we obtain the following dispersion relation:

$$\omega(q) = i\left[\left(e^{2\pi iq/N} - e^{-4\pi iq/N}\right)F - 1\right] \ . \tag{3.14}$$

The imaginary part $\mathrm{Im}\{\omega(q)\}$ determines the linear stability of the wave, as already shown, while $\tilde{\omega}(q) \equiv \mathrm{Re}\{\omega(q)\}$ gives us the pulsation at varying q. The latter reads:

$$\tilde{\omega}(q) = -\left[\sin\left(\frac{2\pi q}{N}\right) + \sin\left(\frac{4\pi q}{N}\right)\right]F \ . \tag{3.15}$$

The phase velocity of the wave packet (3.13) is computed as $V(q) = \tilde{\omega}(q)/q$, whereas the group velocity is:

$$V_{gr}(q) = \frac{d\tilde{\omega}(q)}{dq} = -\frac{2\pi F}{N}\left[\cos\left(\frac{2\pi q}{N}\right) + 2\cos\left(\frac{4\pi q}{N}\right)\right] \tag{3.16}$$

Indicating the direction of positive V's as "eastward" and the opposite as "westward", it is readily seen that at varying q/N all four combinations of positive and negative phase and group velocities can be obtained. Particularly interesting in geophysics is the regime showing westward phase velocity and eastward group velocity: the former feature is characteristic of Rossby waves, a type of large-scale dispersive waves that emerges in shallow fluids on a rotating sphere (e.g. the atmosphere and the oceans), whereas the latter is observed in flows in the β-plane approximation[1] [20]. Such velocities are observed in the following domain:

$$\left(0.1489 < \frac{q}{N} < \frac{1}{3}\right) \bigcup \left(0.5904 < \frac{q}{N} < \frac{2}{3}\right) \ , \tag{3.17}$$

and from the previous discussion one sees that, at the critical value $F = 8/9$, the first wave losing linear stability ($q/N \simeq 1/5$) falls into this interesting regime. This opposite direction of the characteristic velocities is well documented: Lorenz and Emanuel [31] showed that, starting from the initial condition $X_n = F \ \forall n \neq m$ and $X_m = F + \varepsilon$ for a single site m, the slightly-perturbed flat profile develops oscillatory disturbances as time grows, where the individual maxima progress westward and the "center of activity" (e.g. the center of the wave packet) moves eastward.

Several numerical studies have been performed about the transition to chaos when varying F and N. In a subsequent study [25] Lorenz observed that the steady solutions, after the well-known stable fixed points observed for $F < 8/9$, become periodic above that threshold and assume a chaotic nature if $F > 5$ (as long as $N \geq 12$). Karimi and Paul [65] studied spatio-temporal chaos in the model by

[1] This procedure consists in locally approximating a curved surface with small radius of curvature (like Earth's surface) by a tangent plane.

computing the fractal dimension[2] for different values of F and N. For a small forcing $F = 5$ they found alternating windows of periodic and chaotic dynamics with increasing system size, where the periodic windows occur at nearly regular intervals. On the other hand, an intermediate forcing $F = 10$ yields chaotic dynamics for all system sizes explored ($5 \leq N \leq 50$). The transitions between dynamical regimes were mathematically formalized later by van Kekem and Sterk [72] studying bifurcation events in the model at varying $F > 0$: they concluded that no evident pattern seems to arise in bifurcations at different N's.

In conclusion, the single-scale L96 model shows a rich variety of dynamical behaviours that strongly depend on the size of the system and on the magnitude of the external forcing. While some of the transitions between regimes have been understood from a mathematical standpoint, the largest part of them can be found only from numerical parametrical studies. A diagram showing where the bifurcations take place at varying F and N can be found in [72]. Yet, a law predicting whether the model's solutions will be periodic or chaotic is still unknown.

Two-scales L96 model

The study of stable solutions for the two-scales model is not as straightforward as for the single-scale case. First of all, no fixed points are known besides the trivial one $(\{X_n\}, \{y_{n,k}\}) = (0, \dots, 0)$. A linear stability analysis along the lines of the single-scale model, or other analytical approaches, do not seem to be viable options.

Information about the nature of solutions can be gathered only from numerical inspection of the parameter space. Key observations are made by Lieb-Lappen and Danforth [73]: numerical simulation performed for different combinations of N and K (only a rather restricted number of them were considered), and also tuning the coupling parameter h, displayed the existence of both regular and highly chaotic regimes. The regularity is particularly enhanced by increasing the number of fast variables K interacting with each slow one. Frank et al. [32] extended considerably the parametric study, and showed that diminishing the coupling from the customary value $h = 1$, showing a chaotic evolution, a regular region was observed around $h \simeq 0.5$, while going further below the system is led to a strongly-chaotic regime, with the largest Lyapunov exponent increasing as h approaches zero. On the other hand, the regularity for large K observed by the former study is lost for an even larger number of small variables ($K \gtrsim 30$): this value makes the system revert to a chaotic evolution. In summary, parameters h and K display an intermediate region of stability separating two chaotic regions above and below it, while the observed behaviour does not change appreciably when the number of slow variables

[2] Introduced to define the complexity of a fractal structure, the fractal dimension D_λ is often computed using a linear interpolation formula by Kaplan and Yorke in terms of the spectrum of Lyapunov exponents $\lambda_1 \geq \cdots \geq \lambda_N$. The formula reads:

$$D_\lambda = K + \sum_{i=1}^{K} \frac{\lambda_i}{|\lambda_{K+1}|} \ ,$$

where K is the largest integer such that the sum of the first K Lyapunov exponents is non-negative. The fractal dimension of a dynamical system is considered as an approximate value of the number of degrees of freedom acting in the system.

N is increased. These results should make clear that the two-scales model shows a very complex dynamical behaviour, that probably would not have been discovered without resorting to numerical analysis.

Important observations about decorrelation and relaxation times for the slow and fast scales are made in Paragraphs 3.3.1 and 3.3.3, as part of the original work presented hereafter for the two-scales model.

3.3 Nonequilibrium indicators in the viscous and inviscid two-scales Lorenz96 model

The chief interest of the present study is to characterize time-irreversible properties as revealed by two effective indicators of the absence of statistical equilibrium: Asymmetric Time-Correlation Functions (ATCFs) [15], analyzed in Paragraph 2.3.2, and Response Functions (RFs) [53, 16], introduced in 2.3.3. Both of them, but especially RFs, allowed for a deeper insight into the transfer properties (in the form of travelling waves) observed in the model, and into the interactions between slow and fast variables. There are several reasons for choosing the L96 model for such a study: the presence of nonlinear interactions between variables hinders the use of the solid theoretical framework built for linear systems, thereby making necessary the use of numerical simulations. Since we have access to the explicit evolution equations, one can choose to study the "standard" model, namely a driven dissipative system that is far from statistical equilibrium, or else the "reversible" model, where damping and external forcing are put to zero and the total energy is a global conserved quantity, so the system is in statistical equilibrium in the microcanonical sense. In the following we will refer to the original model as "viscous" or "irreversible" L96, and to the model with $F = \nu_1 = \nu_2 = 0$ as "inviscid" or "reversible" L96. In this respect, it becomes especially interesting to analyze the differences between the two above-mentioned indicators when they refer to the former or the latter version of the model. Furthermore, dynamical and statistical features of the inviscid L96 model are much less studied than its viscous forced counterpart (some analysis can be found in [20, 34]), so this study is a relevant addition to the existing literature.

The following Paragraphs are structured as follows. In 3.3.1 the basic statistical properties of the system (i.e. pdf's and time autocorrelation functions) are investigated. Then, Paragraph 3.3.2 includes our results on ATCFs, while 3.3.3 examines different types of responses to external perturbations of the energy.

3.3.1 Low-order statistics: pdf's and autocorrelation functions

In the whole study we used the following parameters for Eqs. (3.5): $c = 5$, $b = 10$, $h = \nu_1 = \nu_2 = 1$, $F = 10$, $N = 30$ and $K = 5$, in order to place the system in the chaotic regime [32]. The inviscid model is recovered by putting $F = \nu_1 = \nu_2 = 0$. Further specifics on the numerical simulations are described in Appendix C.

In its inviscid version, despite the non-Hamiltonian structure, the system evolves on a $(D-1)$-dimensional surface, where $D = N(K+1)$, having constant energy E determined by the initial conditions and defined in (3.6). Hence, all statistical properties of the system are described by the microcanonical ensemble. Furthermore,

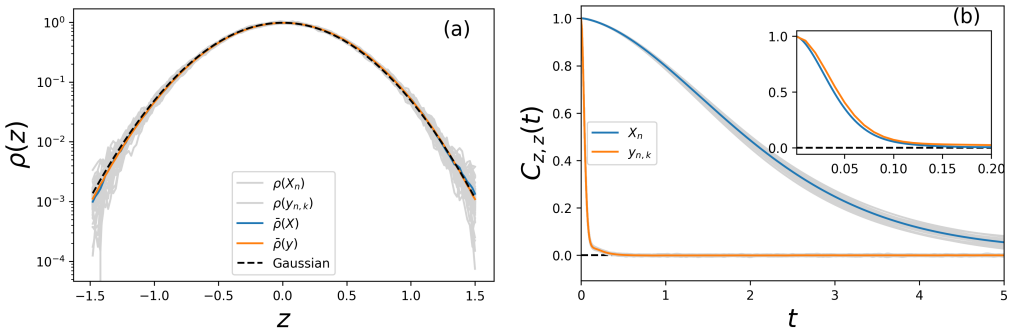

Figure 3.2. Inviscid (or reversible) system. (a): Probability density functions $\rho(z)$, where z denotes both fast and slow variables. Light grey lines indicate pdf's obtained from single-variable trajectories at different values of n and k, while blue and orange lines denote the pdf's averaged on the two latitude circles, namely $\bar{\rho}(z) = \frac{1}{M}\sum_{n=1}^{M}\rho(z_n)$ for $z = X, y$ and $M = N, NK$, respectively. Gaussian distribution is represented by a black dashed line. (b): Time autocorrelation functions $C_{z,z}(t)$. The blue curve is the average autocorrelation computed on all slow variables, and the orange curve the same for fast variables. The inset shows the nice collapse obtained when the time axis of the blue curve is rescaled by a factor bc.

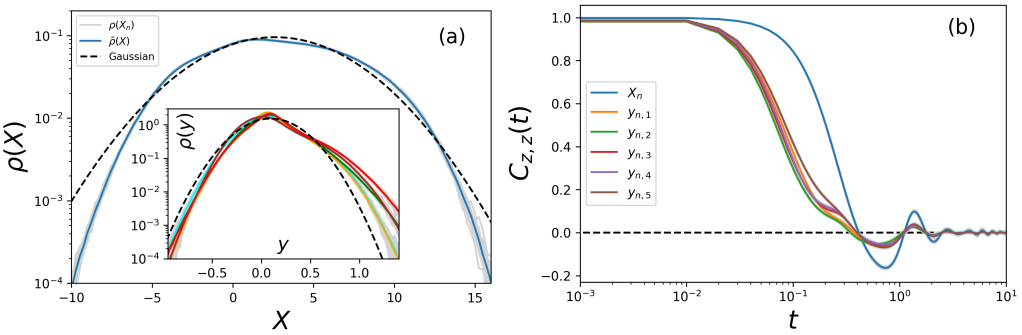

Figure 3.3. Viscous (or irreversible) system. (a): Probability density functions $\rho(z)$ for $z = X$ (main plot) and $z = y$ (inset). Light grey lines of both panels indicate pdf's obtained from single-variable trajectories, whereas the blue line in the main panel is the pdf averaged on all the N slow variables. Colored plots in the inset, with colors shared with panel (b), represent pdf's averaged over the slow indices n at fixed fast index k. Gaussian distributions are represented by black dashed lines. (b): Semilog plot of the time autocorrelation functions $C_{z,z}(t)$, averaged over the latitude circles, for $z = X_n$ (blue) and $z = y_{n,k}$ (each color representing a different index $k = 1, \ldots, K$).

since E is quadratic in X and y the equipartition theorem holds, i.e.

$$\langle X_n^2 \rangle = \langle y_{n,k}^2 \rangle = \frac{E}{N(K+1)} = \frac{E}{D}\,, \tag{3.18}$$

with the angular brackets representing an ensemble average on the constant-energy hypersurface. The dynamics is still chaotic like in the viscous forced case, and a computation of the largest Lyapunov exponent λ_1 with the Benettin-Galgani-Strelcyn procedure [74] gave the value $\lambda_1 \simeq 3.7$. For comparison, the forced viscous model shows a maximum exponent $\lambda_1 \simeq 5.5$. Each variable is distributed according to a normal distribution with variance E/D, as can be seen from Fig. 3.2a. The

equivalence of the variables must be understood only as regards the static statistical properties of the system, such as the average energy. From a dynamical point of view, however, the variables X_n and $y_{n,k}$ evolve on different time scales, as clearly highlighted by Fig. 3.2b, which shows the normalized time autocorrelation functions

$$C_{z,z}(t) \equiv \frac{\langle z(t_0)z(t_0+t)\rangle - \langle z(t_0)\rangle^2}{\langle z^2(t_0)\rangle - \langle z(t_0)\rangle^2} \ . \tag{3.19}$$

Ensemble averages may be replaced by temporal averages with respect to t_0 invoking ergodicity and assuming statistical stationarity, and $z = \{X_n, y_{n,k}\}$ indicates a generic variable of the system. Since in the inviscid case the system is subject only to advection-like interactions, and these terms in the equations for the y's are bc times larger than those of the X's, the ratio between the two time scales is of the same order of magnitude of bc. This is evident in the inset of Fig. 3.2b, where the slow-variable autocorrelation is plotted as a function of the rescaled time $t\,/\,bc$, showing a nice collapse onto the fast-variable curve.

The behavior of the viscous system is rather different from the inviscid case: the total energy is no longer a constant of motion and, at long times, it fluctuates around a stationary value that is determined by the balance between forcing and dissipation. This causes the system to behave irreversibly and the statistical properties are no longer described by an equilibrium statistical ensemble. In this situation the equipartition theorem does not hold, and fast and slow variables cease to be equivalent even with regard to static properties. These considerations are illustrated in Fig. 3.3a, which shows the probability distributions for both X_n (main plot) and $y_{n,k}$ (inset). First, it emerges that both variables are skewed and clearly non-Gaussian [64]. Furthermore, from comparing the horizontal scales, it can be seen that the y variables have a standard deviation approximately b times smaller than the typical fluctuations of the X variables, as imposed by construction in the model. Regarding the dynamical behavior, the autocorrelation functions (Fig. 3.3b) of both X and y display, at later stages, oscillations with the same frequency and phase. However, the autocorrelation functions of the y's decay roughly c times faster than the correlations of the X's. The short-time behaviour is due to the fact that the characteristic dissipation times of X and y differ by exactly a factor of c, but at larger times the slower timescales will drive the fast variables via the coupling term in Eq. (3.5b), and consequently induce low-frequency oscillations like those of the slow variables.

As we will see in the next Paragraph, the properties of the model mentioned above will play a crucial role in interpreting the behavior of the indicators which are typically considered to reveal time-reversal symmetry breaking.

3.3.2 Time irreversibility

In this Paragraph, we would like to measure deviations from equilibrium (or from time-reversibility) by defining suitable ATCFs, introduced in Paragraph 2.3.2. Our aim is to study the difference observed in the ATCFs $\Psi(\tau)$, defined in Eq. (2.62), when measured both in the inviscid model with $F = 0$ and in the viscous one with $F = 10$. The type of asymmetric time correlation functions used in this study are,

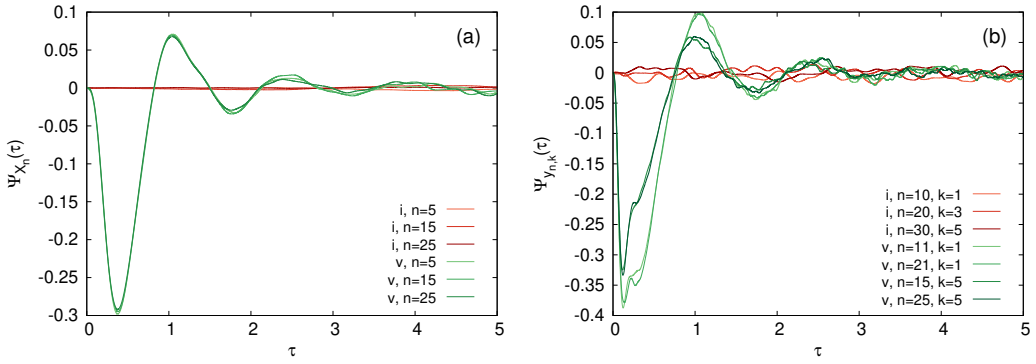

Figure 3.4. ATCFs in the inviscid (red palette, labelled with 'i') and viscous (green palette, labelled with 'v') two-scales L96 model for different n's. (a) Correlations of slow variables, Eq. (3.20) with $z = X_n$. (b) Correlations of fast variables, Eq. (3.20) with $z = y_{n,k}$. Non-overlap between leftmost ($k = 1$) and rightmost ($k = K$) fast variables, for arbitrary n, is evident. Statistics: $2 \cdot 10^5$ samples.

in non-dimensional form:

$$\Psi_z(\tau) = \frac{\langle z^2(t)z(t+\tau)\rangle - \langle z(t)z^2(t+\tau)\rangle}{\langle z^2(t)\rangle^{3/2}} \ , \tag{3.20}$$

where again $z = \{X_n, y_{n,k}\}$ is a generic variable. They represent the lowest-order type of non-symmetric time correlations that are "local" in terms of $X_n(t)$ or $y_{n,k}(t)$. The denominators need to be even moments of the variables, because odd-order ones vanish in the inviscid case.

The difference between the two systems clearly emerges in Fig. 3.4, representing in panel (a) the functions (3.20), for $z = X_n$, for both viscous and inviscid models and in panel (b) the functions (3.20), for $z = y_{n,k}$, for the same cases. The large fluctuations experienced by the forced dissipative model are a clear sign of deviation from equilibrium, and the peculiar damped oscillations can be understood as a superposition of many complex exponentials of the type (3.13) [31, 20]. As expected, the symmetry of slow variables under cyclic translation of the indices is reflected in the almost-perfect superposition of the correlations in the viscous case. For the fast variables there is cyclic symmetry as well but only for translations modulo K, as emerges in Fig. 3.4b.

Let us notice that the differences in typical magnitudes and timescales between X's and y's are lost in these time correlations: the peak amplitudes and oscillation frequencies are almost identical in the viscous case. Similarity in the peaks amplitudes is a simple consequence of the normalization, while the coincidence of timescales after a few decorrelation times was a trend already found in Fig. 3.3b for $C_{z,z}(\tau)$, and it can be explained in the same way.

We computed also sixth-order ATCFs, of the kind $\Psi_{z^2}(\tau)$, representing asymmetric time correlations of the "local" energies. The qualitative behaviour is rather similar to Fig. 3.4 so we avoid showing them here. However, the signals appear more noisy since larger statistics are needed for computing higher-order moments. This similarity is interesting because these asymmetric correlations are formally equivalent to third-order moments of local-energy differences in time [75, 41], functions that

are investigated for the Sabra model in Paragraph 4.5.1 and Appendix D. Therefore the initial negative trend shown by $\Psi_{z^2}(\tau)$, similar to that displayed by the green curves in both Figs. 3.4, would represent an initial energy loss for variable z. Yet this implies that both fast and slow variables lose energy at small times, while the total energy is observed to remain stationary. Further simulations allowed to better understand this odd behaviour: third-order moments of the time variations of X_n^2 or $y_{n,k}^2$, at a fixed n, appear to be balanced in sign by the analogous quantity computed for $\sum_{k=1}^{K} y_{n,k}^2$. This explanation is still rather vague and speculative, and what we found may just be the effect of trivial cancellations when expanding the powers of the polinomials: further investigation on this matter are necessary, so we shall not delve into more details.

3.3.3 Energy response functions

This Paragraph is dedicated to the other class of powerful nonequilibrium indicators, able to determine causal interactions [12] and transition asymmetries [11]: *non-diagonal RFs* (see Paragraph 2.3.3). Our aim here is to investigate the relaxation behaviour of a perturbation acting locally on a single variable X_n or $y_{n,k}$. This relaxation will propagate to all the variables interacting directly or indirectly with the perturbed one, but the way in which the redistribution occurs provides useful information about the statistical properties of the system. As will be clear shortly, both the long-time behaviour of the RFs and the transients leading to it are able to discriminate between equilibrium and nonequilibrium, and highlight statistical fluxes where present. Of course the effectiveness of RFs for this type of study depends on the choice of the right observables.

The general form of the RFs we will employ is that of Eq. (2.73), recalling that also functions of the phase space can be used. A reasonable choice could be to consider the local energies,

$$E_{X_n} = X_n^2/2 \qquad E_{y_{n,k}} = y_{n,k}^2/2 \ , \tag{3.21}$$

as the perturbed and measured observables of the RFs. The reason for such a choice is that it is physically easier to imagine a perturbation that increments or decreases the energy of a system, while a perturbation displacing directly the X_n's or $y_{n,k}$'s could give problematic interpretations. In order to ease the notation, we will indicate as subscripts of the RFs only the indices of the variables, namely: $R_{m\,;n}(t) \equiv R_{E_{X_m}\,;E_{X_n}}(t)$ and $R_{m,j\,;n,k}(t) \equiv R_{E_{y_{m,j}}\,;E_{y_{n,k}}}(t)$. The indices before of after the semicolon makes clear if a fast or a slow variable is involved. Thus, the focus will be on functions like:

$$R_{m\,;n}(t) = \frac{\overline{\delta E_{X_n}}(t)}{\delta E_{X_m}} \tag{3.22}$$

$$R_{m,j\,;n,k}(t) = \frac{\overline{\delta E_{y_{n,k}}}(t)}{\delta E_{y_{m,j}}} \ , \tag{3.23}$$

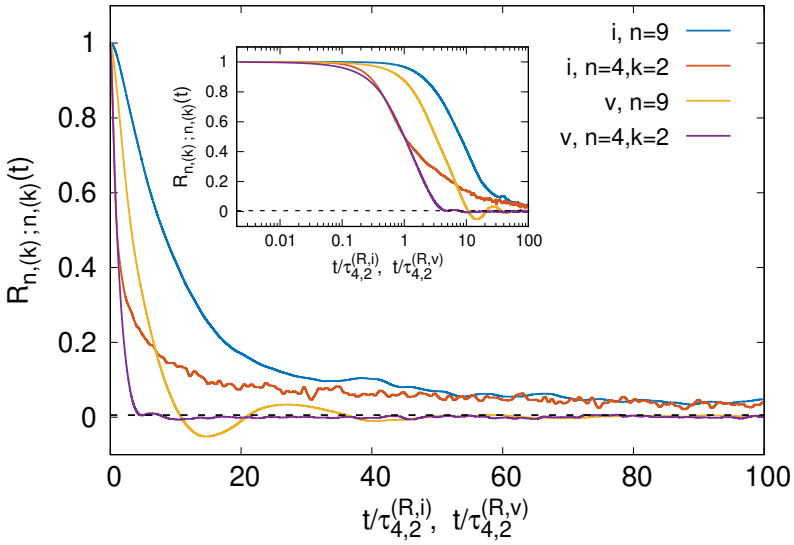

Figure 3.5. Diagonal RFs for the local energies of fast and slow variables, in both inviscid (labelled as 'i') and viscous (labelled as 'v') systems. Black dashed line: predicted equilibrium asymptote $\sim [N(K+1)]^{-1} = 1/180$. Time rescaled with the relaxation times of the fast variables in inviscid ($\tau^{(R,i)}_{4,2}$) and viscous ($\tau^{(R,v)}_{4,2}$) cases. Their ratio is: $\tau^{(R,i)}_{4,2}/\tau^{(R,v)}_{4,2} \simeq 3.7$. Inset: same as main panel but in semilog scale. Here and in all following plots the average is over 10^5 realizations.

measuring intra-scale properties, or like:

$$R_{m\,;n,k}(t) = \frac{\overline{\delta E_{y_{n,k}}}(t)}{\delta E_{X_m}} \tag{3.24}$$

$$R_{m,j\,;n}(t) = \frac{\overline{\delta E_{X_n}}(t)}{\delta E_{y_{m,j}}} \ , \tag{3.25}$$

measuring inter-scale properties. The (positive-signed) perturbations are performed in the following way:

$$X'_m = \mathrm{sgn}(X_m)\sqrt{X_m^2 + 2\,\delta E_{X_m}} \tag{3.26}$$

and similarly for $y_{m,j}$. Here δE_{X_m} is the amplitude of the perturbation, chosen to be of the order of typical fluctuations of that energy [76], namely equal to the standard deviation of E_{X_m}. This procedure ensures that the perturbation is independent of X_m and it always increases its energy. Let us remark that, since disturbances are not infinitesimal, we are outside the regime of linear response theory.

Diagonal (or self-) RFs provide quantitative information about the relaxation time of the initial perturbation: usually one can define the relaxation time $\tau^{(R)}_m$ (in the same compressed notation) as the time a diagonal response function $R_{m\,;m}(t)$ takes to cross a chosen threshold, e.g. 1/2. In Fig. 3.5 the four different kinds of self-RFs are shown, with time measured in terms of the relaxation times of the perturbation on $E_{y_{4,2}}$ in both inviscid and viscous systems, named respectively $\tau^{(R,i)}_{4,2}$ and $\tau^{(R,v)}_{4,2}$. The relaxation is slower in the inviscid model: not only $\tau^{(R,i)}_{4,2}$ is almost 4 times bigger

than $\tau_{4,2}^{(R,v)}$, but comparing the relaxation times between slow and fast variables of same-type systems we find $\tau_9^{(R,i)}/\tau_{4,2}^{(R,i)} \simeq 8.0$, whereas $\tau_9^{(R,v)}/\tau_{4,2}^{(R,v)} \simeq 3.2$. (see blue and yellow curves in Fig. 3.5). The different relaxation times are appreciated better in the inset, where a logarithmic time axis is employed. The comparison between the characteristic time scales of temporal autocorrelation functions of the variables and diagonal responses of the energies deserves some discussion. In the viscous case, both the ratio of slow-to-fast-variables decorrelation times and the energy relaxation time of a slow variable divided by that of a fast variable are close to the value of c. In the inviscid system, instead, the ratio between the time scales of the energy self-RFs is approximately 10, while for the variables autocorrelations a ratio of about $bc = 50$ was estimated in Paragraph 3.3.1 (see Fig. 3.2 and related discussion). Even though FDRs cannot be invoked, since neither we are in the linear regime nor we are looking at time correlations and responses on the same observables (namely, correlations of z and response functions of z^2), it is nonetheless interesting to note how differently multiscale systems behave with respect to time-dependent statistical properties when one switches from a conservative to a dissipative dynamics.

There is a clear difference in the asymptotic behaviour of equilibrium and non-equilibrium RFs. While the viscous responses relax to zero, meaning that the perturbation will eventually die out and the perturbed energy will recover its unperturbed value, the inviscid ones reach a common positive value. As a matter of fact, equilibrium statistical mechanics tells us that a perturbation on a conservative system will carry it away from the hypersurface in phase space where the dynamics was constrained, to a new "perturbed" hypersurface. Assuming that the asymptotic state is a new equipartition configuration, then the long time value of all inviscid RFs reads: $R_{m,(j);n,(k)}(t) \xrightarrow{t\to\infty} [N(K+1)]^{-1}$. This value is reported in Figs. 3.5 and 3.6 as a black dashed horizontal line. Due to the slow dynamics the establishment of a new equipartition state takes a very long time, so even our longest computations were not able to get close to the expected asymptotic value. Also inviscid nondiagonal responses display the same asymptote: in Fig. 3.6 the average spreading of an energy perturbation, performed respectively on a slow (Fig. 3.6a) and a fast (Fig. 3.6b) variable, are represented. Also instances of inter-scale RFs are included as blue solid lines.

We will now focus on the RFs in the viscous system. We saw in Section 3.2 that, in the linear regime of the single-scale L96, small fluctuations around the steady state propagate like waves with definite phase and group velocities [31, 20]. Even though the extension of this result to the two-scales model is made more difficult by the coupling terms, one may expect analogous (or at least similar) behaviours to be found even in this case. The nonlinear terms in the equations (3.5) imply that, if the slow variables display waves propagating with a given phase velocity direction, then the fast ones will be characterized by waves moving in the opposite direction. We will now see that RFs help to visualize in an alternative way the propagation of waves that are triggered by the initial perturbation.

Figures 3.7 shows intra-scale energy RFs for slow (first row) and fast (second row) variables, when measured in the westward (left column) or eastward (right column) direction, with the usual rescaled times. The most stricking feature is the almost perfect similarity between the westward slow responses in panel (a) and eastward fast

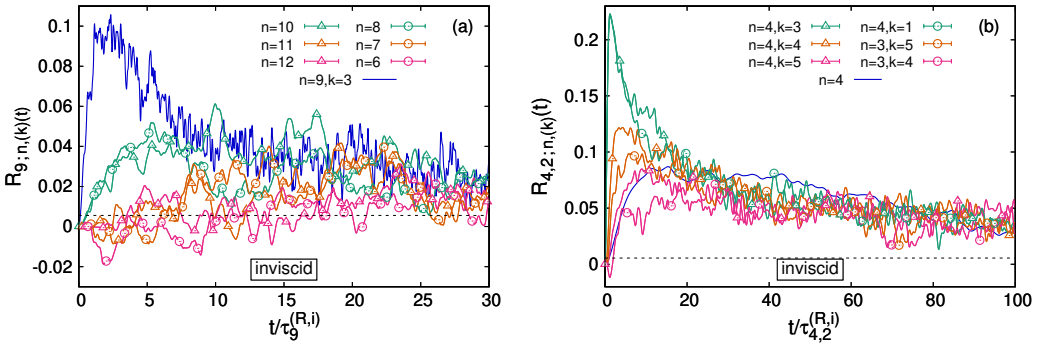

Figure 3.6. Nondiagonal RFs for the local energies in the inviscid system. Responses with same distance from the perturbed variable share the same color coding. (a) Perturbation on the energy of a slow variable. (b) Perturbation on the energy of a fast variable. In both panels, time is rescaled with the relaxation time of the perturbed variable. Triangles: intra-scale responses measured eastward. Circles: intra-scale responses measured westward. Blue solid line: inter-scale response of the corresponding (same n) variable. Black dashed line: same asymptote as Fig. 3.5.

responses in panel (d): the functions show positive peaks that become more damped and delayed as one gets further away from the perturbation. As highlighted in the insets the speed of propagation is constant: the time to reach a site at a distance d is linear in d. On the other hand, panels (b) and (c), showing respectively eastward slow responses and westward fast responses, show a less clear behaviour with both positive and negative peaks at short times, even though some qualitative similarities are observed. This coherent behaviour of the RFs in the direction of a statistical flux, accompanied by incoherence in the opposite direction, is also observed in turbulent shell models [41] and will be treated in Section 4.5. It is possible that the unclear behaviour in the "upstream" direction (opposite to that of wave propagation) may be due to a superposition of perturbation-induced fluctuations. Considering for instance a perturbation on a slow variable, the upstream response is influenced by both fluctuations that have travelled upstream remaining in the same scale but also by those that have passed to the faster scale, moved "downstream" up to a point and then returned to the slow scale.

Let us remark, in passing, that the response functions closest to the perturbation display non-zero initial time derivatives. This is a simple consequence of the evolution equations (3.5). Taking for instance the X_n's, it can be shown that:

$$\dot{R}_{m;n}(t)|_{t=0} = \begin{cases} \pm C\overline{\left[\frac{X_n X_{n+p}}{X_m}\right]} & \text{if } \; n = m-1, m+1, m+2 \\ 0 & \text{otherwise} \end{cases} , \tag{3.27}$$

where C is a positive constant and $p = \pm 1, \pm 2$. Now, in the viscous model the pdf's of the X_n are shifted towards positive values, as can be appreciated in Fig. 3.3a: actually in the single-scale model it can be computed analytically that $1/N \sum_n \overline{X_n}$ lies in the range $[0, F]$ [31]. We may then suppose that also products and ratios of X's, taken at different sites but at equal time, will be positive on average, therefore the mean value on the r.h.s. of (3.27) is positive and the sign of the time derivative

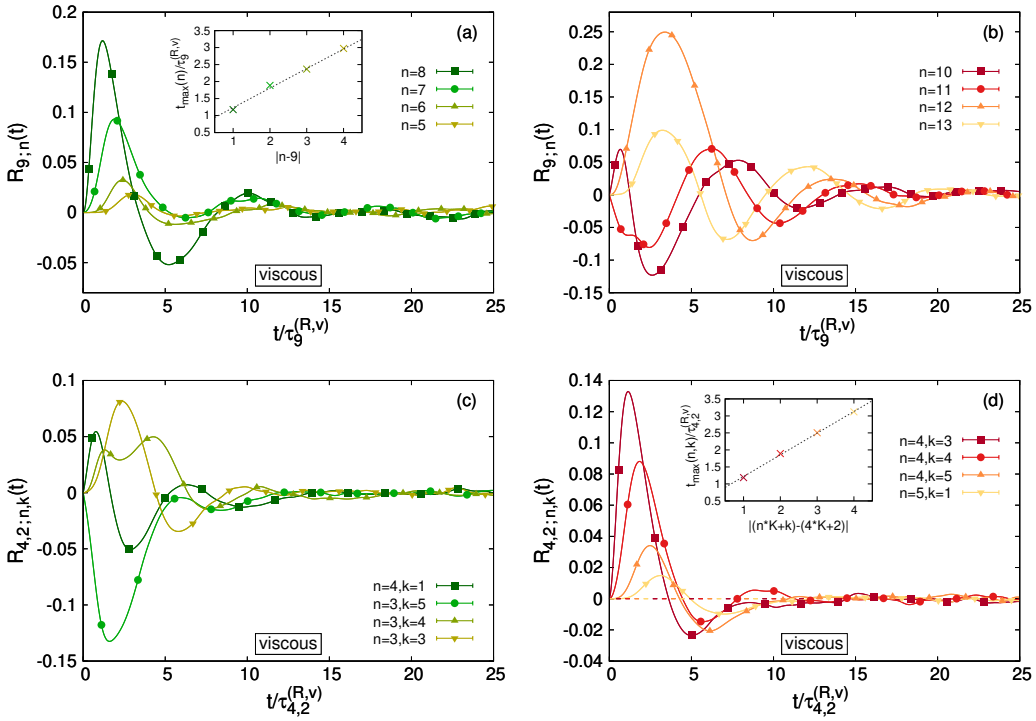

Figure 3.7. Nondiagonal energy RFs in the viscous system. Westward and eastward responses are represented separately. (a) Westward RFs for the perturbation on a slow variable. (b) Eastward RFs for the perturbation on the same slow variable. (c) Westward RFs for the perturbation on a fast variable. (d) Eastward RFs for the perturbation on the same fast variable. Time axis is rescaled like in Fig. 3.6. Insets in panel (a) and (d) show the (rescaled) times at which the maxima are reached, as a function of the distance from the perturbation. The dashed lines are linear best fits.

is determined by the $\pm$ before C, which comes from the nonlinear term and merely depends on the relative position of n with respect to m.

When studying inter-scale RFs some care must be taken, especially when the two scales are characterized by different amplitudes and timescales. In such cases some form of rescaling is needed for comparing RFs with perturbation and measure on different variables. The rescaled functions one can choose are:

$$\tilde{R}_{m,(j)\,;\,n,(k)}(t) = \frac{\delta E_{X_m(y_{m,j})}}{\langle E_{X_n(y_n,k)}\rangle} R_{m,(j)\,;\,n,(k)}(t) = \frac{\overline{\delta E_{X_n(y_{n,k})}}(t)}{\langle E_{X_n(y_n,k)}\rangle} \,. \tag{3.28}$$

They measure the relative energy deviation of a chosen variable caused by a perturbation on the energy of another (or the same) variable. We show in Fig. 3.8 how the inter-scale response functions (3.24) and (3.25) appear after the rescaling (3.28). It is evident that a finite perturbation on a fast variable has almost no effect - in percentage - on the corresponding slow one, while an energy fluctuation on a slow variable has a visible effect on the corresponding fast variables. Moreover, the maximum responses for the fast variables are attained at a time comparable with the relaxation time of the slow variable, $\tau_9^{(R,v)}$ (red vertical dashed line). Of course a generic perturbation, even infinitesimal, has a drastic consequence on any chaotic

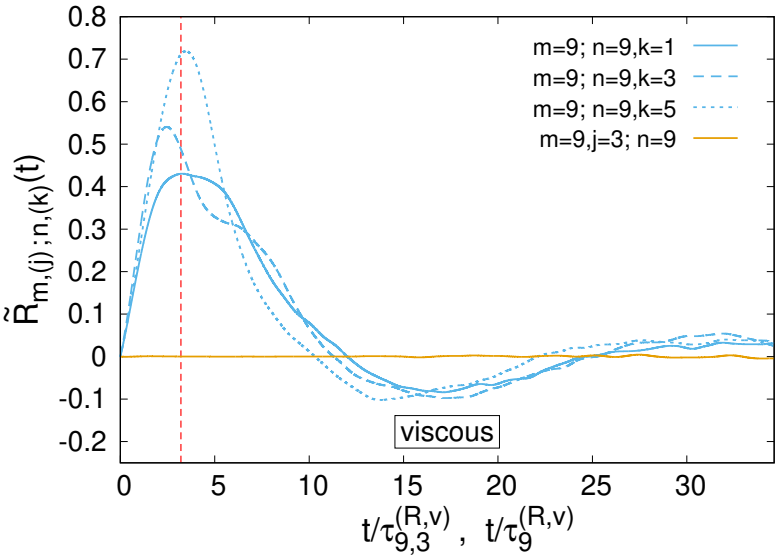

Figure 3.8. Rescaled inter-scale RFs (3.28) in the viscous system. Azure plots show the effect of a slow-variable energy perturbation on three of its corresponding fast variables, the orange one the effect of a fast-variable perturbation on its corresponding slow variable. The time axis is rescaled with $\tau_{9,3}^{(R,v)}$ for the azure plots and with $\tau_{9}^{(R,v)}$ for the orange one. The red vertical dashed line corresponds to $t = \tau_{9}^{(R,v)}$.

system if one waits long enough. The purpose of rescaled RFs is rather to visualize the interplay between different timescales, and how much influence one has on the other.

These results should make clear that, in order to give meaning to the measurement of a response function, one needs to know which degree of freedom has been initially perturbed, and possibly know the dynamical features (amplitude, timescale) of such variable. In order to further prove this point, we show in Fig. 3.9 two RFs of the total energy E, defined in Eq. 3.6, when a perturbation of same amplitude is performed on a slow or on a fast variable, namely:

$$R_{m,(j);E}(t) = \frac{\overline{\delta E}(t)}{\delta E^{(m,(j))}} \,. \tag{3.29}$$

The common perturbation has a strength: $\delta E^{(m,(j))} = \sqrt{\delta E_{X_m}\, \delta E_{y_{m,j}}}$, where δE_{X_m} and $\delta E_{y_{m,j}}$ are the perturbations previously used respectively for slow and fast variables in Figs. 3.7 and 3.8. The key observation here is that the two functions are subject to two perturbations of equal amplitudes (same denominator) and measure responses of the same quantity, yet they showcase very different relaxation behaviour: a faster relaxation is associated to the initial perturbation on the fast variable. That is to say that measuring the induced fluctuations of a physical quantity cannot provide much information about the physics of the system if one does not know where the perturbation causing the fluctuations came from (i.e. which observable was perturbed).

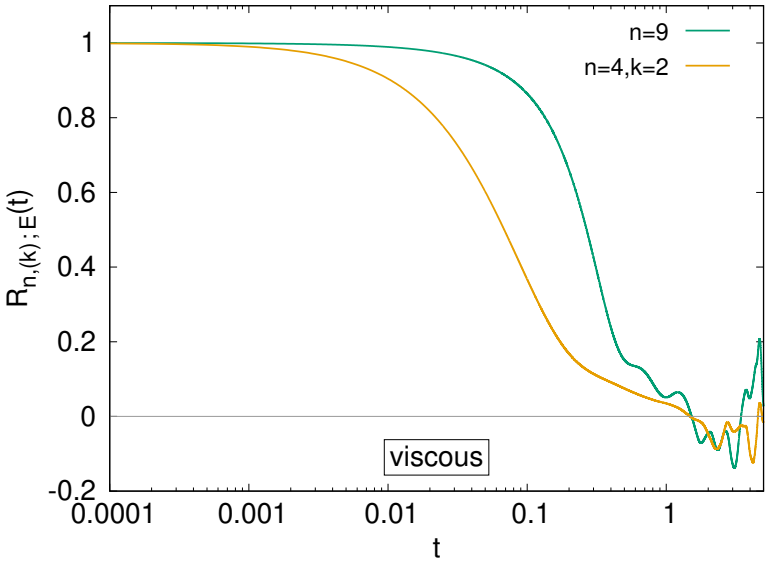

Figure 3.9. Response functions of the total energy E, Eq. (3.6), to two equal perturbations performed on E_{X_9} (green curve) and $E_{y_{4,2}}$ (orange curve), displayed in semilog axes.

3.4 Conclusion

In the study presented in this Chapter we have studied in details two common indicators, namely asymmetric time-correlation functions and response functions, of time-reversal symmetry breaking in the two-scales Lorenz96 model, a system usually taken as a paradigm for the evolution of geophysical flows. We have shown that such time correlations successfully discriminate the statistical state of the system. In the inviscid case, their behaviour is dominated by statistical errors causing modest fluctuations around zero as expected for an equilibrium system. In the forced and viscous case, instead, these correlations show a pronounced peak at small times followed by damped oscillations, revealing the nonequilibrium nature of the dynamics.

We then focused on studying the responses to impulsive external perturbations of the local energies. It has been shown that, apart from providing useful information about the transport phenomena in the system, the asymptotic behavior of the responses provides clear indications on the presence of temporal asymmetries. Indeed, in the inviscid case all the response functions converge to the same non-vanishing constant as expected from a system evolving on a constant-energy phase-space hypersurface. On the other hand, in the viscous system the energy of the perturbed system, after a transient, returns to fluctuate around the value it had in the unperturbed dynamics. The response functions also highlight the presence of traveling waves in both slow and fast variables, propagating with constant speed but in opposite directions. The study of inter-scale responses then allowed us to elucidate some aspects of multiscale systems. In particular, due to the different scales presented by the variables, it has been observed that a finite perturbation of a fast variable induces negligible fluctuations (in percentage) in the slow variables,

while perturbations of the slow variables cause macroscopically relevant fluctuations of the fast variables. Although the particular coupling between the slow and fast scales certainly plays a role, this characteristic is expected to be typical of many geophysical systems.

Finally, by considering the response of global variables (such as the total energy of the system) to local perturbations of fixed amplitude we provided evidence of the impossibility of predicting the behaviour of the system without detailed knowledge of either its dynamics or the procedure adopted to produce the fluctuation. It is equally questionable to use results and features from time correlation functions, such as decorrelation times, to gain information about the relaxation following an external perturbation. This consideration sheds light on some of the practical difficulties that must be faced when studying complex systems, such as the climate, where it is impossible to directly perturb the system (except by considering computational models), and in which macroscopic fluctuations generally arise from the simultaneous occurrence of many different physical processes.

An interesting perspective is to apply the tools investigated here to probe a more genuine geophysical system, if not directly experimental records. Indeed, asymmetric time correlation functions offer important information about the statistics of the system that can be used in the context of stochastic parametrization [24]. The response functions may be more difficult to obtain, but nevertheless they may provide useful insights about transport properties and causal dependencies of the system under investigation.

Chapter 4

Nonequilibrium in turbulent shell models

This Chapter starts introducing some basic ideas on hydrodynamic turbulence from both a mechanical and statistical point of view. The purpose is to give enough background to better understand the topics presented in the second part, namely in Section 4.5, which constitutes the original part of the Thesis.

Specifically, we shall first introduce the cornerstone equation of fluid dynamics, the Navier-Stokes equation, along with its main features and symmetries. It is then pointed out how the truncated Euler equation, which is the unforced inviscid version of the Navier-Stokes equation, can be qualified as a system in statistical equilibrium. After that, the statistical approach to turbulence will be introduced, stressing the importance of the Fourier-space representation. The Richardson cascade picture and statistical theory due to Kolmogorov, called K41 theory, are then presented with their most notable results, focusing next on the phenomenon that K41 could not explain: intermittency. Finally, it will be seen that the difficulties encountered in those equations can be reduced by resorting to simplified dynamical systems, able to reproduce both turbulent and inviscid phenomenology: the shell models. Particular emphasis is placed on the Sabra shell model, which is the one used in our work.

The second part deals with the original research project. The purpose is the understanding of how the persistent nonequilibrium state reached by 3D forced turbulence, known as "turbulent energy cascade", is reflected in the behaviour of nonequilibrium descriptors which are not only able to discriminate between statistical equilibrium and its absence, but can add physical insights to the phenomenon. The two descriptors, or indicators, used in this work are the ATCFs, first introduced by Pomeau in the 80's, and nondiagonal RFs. Both have been introduced and discussed in Section 2.3. In order to perform numerical studies we used the Sabra shell model, which retains the principal features of turbulence while reducing greatly the computational complexity.

4.1 Fluid mechanics: history and main properties

The highly peculiar behaviour of fluids have been captivating scientists since ancient times: the first methodical study on the properties of fluids at rest is attributed to

the greek scientist Archimedes of Syracuse (ca. 287 – ca. 212 BC), who formulated the law bearing his name for the buoyancy force exerted on a body immersed in a fluid. Much more recent studies (Torricelli and Pascal, XVII century) brought a definition and formalization of concepts such as the hydrostatic pressure.

However it is rather the behaviour of fluids in motion, which is observed everywhere in nature, that appears more mesmerizing and intriguing. Mere observations made clear that such flows can be split in two categories or regimes: the chaotic and disordered motion observed in the majority of fluids, named *turbulent*, and the regular and smooth one called *laminar*. Since laminar flows are just rare occurrences, most efforts have been directed towards the study of turbulence phenomenology. Let us point out that, as we will see shortly, both regimes are actually described by the same dynamical laws: the discriminating factor between them is the relative importance (magnitude) of different terms appearing in the equation.

The quest to fully understand and predict properties of fluid motion, which started centuries ago by Newton and Bernoulli, proved to be extremely challenging, and it still is nowadays.

The cornerstone law which describes the flow of a viscous fluid is the celebrated Navier-Stokes (NS) equation, according to which the evolution of the velocity field $\boldsymbol{u} = \boldsymbol{u}(\boldsymbol{r}, t)$, satisfies [19]:

$$\begin{cases} D_t \boldsymbol{u} \equiv \partial_t \boldsymbol{u} + \boldsymbol{u} \cdot \boldsymbol{\nabla} \boldsymbol{u} = -\boldsymbol{\nabla} p/\rho + \nu \Delta \boldsymbol{u} + \boldsymbol{f} & (4.1) \\ \boldsymbol{\nabla} \cdot \boldsymbol{u} = 0 & (4.2) \end{cases}$$

Here $D_t \equiv \partial_t + \boldsymbol{u} \cdot \boldsymbol{\nabla}$ is called material or advective derivative, and represents the rate of change, computed in the laboratory frame, of a fluid element moving along (advected by) the flow. Then, $p = p(\boldsymbol{r}, t)$ is the local fluid pressure, $\rho = \rho(\boldsymbol{r}, t)$ the fluid density, ν the kinematic viscosity and $\boldsymbol{f} = \boldsymbol{f}(\boldsymbol{r}, t)$ a generic external forcing per unit mass, which is typically a stirring force which injects energy at large length scales. The constraint $\boldsymbol{\nabla} \cdot \boldsymbol{u} = 0$ ensures the incompressibility of the flow, namely that the density ρ of each moving fluid element does not change in time. There are further external constraints imposed on the flow, namely boundary conditions, which depend on the specific problem at hand. They can be adherent to real fluid, like a no-slip boundary condition on a wall, or more abstract, like the infinite-volume limit or periodic boundary conditions.

Despite being of a very complicated nature from a mathematical standpoint [1] , the NS equation merely represents Newton's 2nd law - again, in the frame of reference moving with velocity $\boldsymbol{u}$. The l.h.s. of (4.1) is the acceleration experienced by the small portion of fluid when it is subject to the forces (per unit mass) displayed on the r.h.s. The first term is the pressure force exerted by adjacent fluid elements, acting perpendicularly to the surface of the considered fluid volume. The second is the contribution by viscous forces, which basically quantifies the friction between two elements sliding one with respect to the other and acts tangentially to the surface. It is a dissipative force converting irreversibly the kinetic energy of the fluid into heat.

[1] It is certainly known among mathematicians and physicists that the proof of existence and uniqueness of global solutions, for all times, for the 3D NS equation is one of the Millennium Prize Problems, and is still an open problem. For info see: `https://en.wikipedia.org/wiki/Millennium_Prize_Problems`.

Both terms can indeed be expressed in terms of a single *stress tensor* $\tilde{\boldsymbol{\sigma}}$: the pressure force can be computed from its diagonal components, while the viscous one from the non-diagonal entries. Finally, the third term can be any external volume force, for instance due to gravity or to a propeller. A source of energy plays a fundamental role if one is interested in measuring stationary properties of the flow. In the absence of viscosity and external forcing, Eq. (4.1) becomes the *Euler equation*:

$$\partial_t \boldsymbol{u} + \boldsymbol{u} \cdot \boldsymbol{\nabla} \boldsymbol{u} = -\boldsymbol{\nabla} p/\rho \ , \tag{4.3}$$

which describes the dynamics of an ideal fluid.

It is common knowledge that the presence of symmetries in a system of interest considerably facilitates the understanding of its mechanical properties, thanks to the relationship between continuous symmetries and conserved quantities formalized by Noether's theorem. As a consequence it proves quite useful to seek symmetries in the NS equation (4.1) [6]. In order to put ourselves in the most "symmetric" configuration, let us consider a fluid without boundaries. Since this could cause convergence problems at infinity, one considers instead a fluid in a *periodic box* of linear size ℓ (i.e. a torus $\mathbb{T}^3$ if we assume 3 space dimensions), meaning that the velocity field $\boldsymbol{u}(\boldsymbol{r}) = \boldsymbol{u}(x, y, z)$ satisfies the periodic boundary conditions:

$$\boldsymbol{u}(x + m\ell, y + n\ell, z + q\ell) = \boldsymbol{u}(x, y, z) \ , \quad m, n, q \in \mathbb{Z} \ , \quad x, y, z \in [0, \ell) \ . \tag{4.4}$$

The unbounded-space limit can be recovered by letting $\ell \to \infty$. The main symmetries of the NS equation are [6]:

- *space translation*: $\boldsymbol{r} \longrightarrow \boldsymbol{r} + \boldsymbol{r'}$, $\boldsymbol{r'} \in \mathbb{R}^3$;
- *time translation*: $t \longrightarrow t + \tau$, $\tau \in \mathbb{R}$;
- *Galilean transformation*: $\boldsymbol{r}, \boldsymbol{u} \longrightarrow \boldsymbol{r} + \boldsymbol{v}t, \boldsymbol{u} + \boldsymbol{v}$, $\boldsymbol{v} \in \mathbb{R}^3$.

Another symmetry exists, the one under scaling, that deserves special attention since from a physical perspective it leads to a crucial concept in turbulence. For the Euler equation (4.3) it reads:

- *scaling transformation*: $\boldsymbol{r}, \boldsymbol{u}, t \longrightarrow \lambda \boldsymbol{r}, \lambda^h \boldsymbol{u}, \lambda^{1-h} t$, $\lambda \in \mathbb{R}^+, h \in \mathbb{R}$.

The presence of the viscous term, though, limits its range of validity: in the NS equation (4.1) the scaling symmetry only holds if $h = -1$. However, as pointed out by Frisch [6], the "full" scaling symmetry for any $h \in \mathbb{R}$ is restored at small scales in the regime of *fully-developed turbulence*, corresponding to the limit $\nu \to 0$. As we shall see in Paragraph 4.3.2, Kolmogorov's theory predicts a scaling exponent $h = 1/3$. We would like now to apply scaling transformations to make the NS equation non-dimensional, i.e. measure time, length, velocity and so on in terms of arbitrary reference scales. Choosing a length scale L and a velocity scale U, one can define non-dimensional quantities in the following way:

$$\boldsymbol{r'} = \frac{\boldsymbol{r}}{L} \ , \quad \boldsymbol{u'} = \frac{\boldsymbol{u}}{U} \ , \quad t' = \frac{U}{L} t \ , \quad p' = \frac{p}{\rho U^2} \ , \quad \boldsymbol{f'} = \frac{L}{U^2} \boldsymbol{f} \tag{4.5}$$

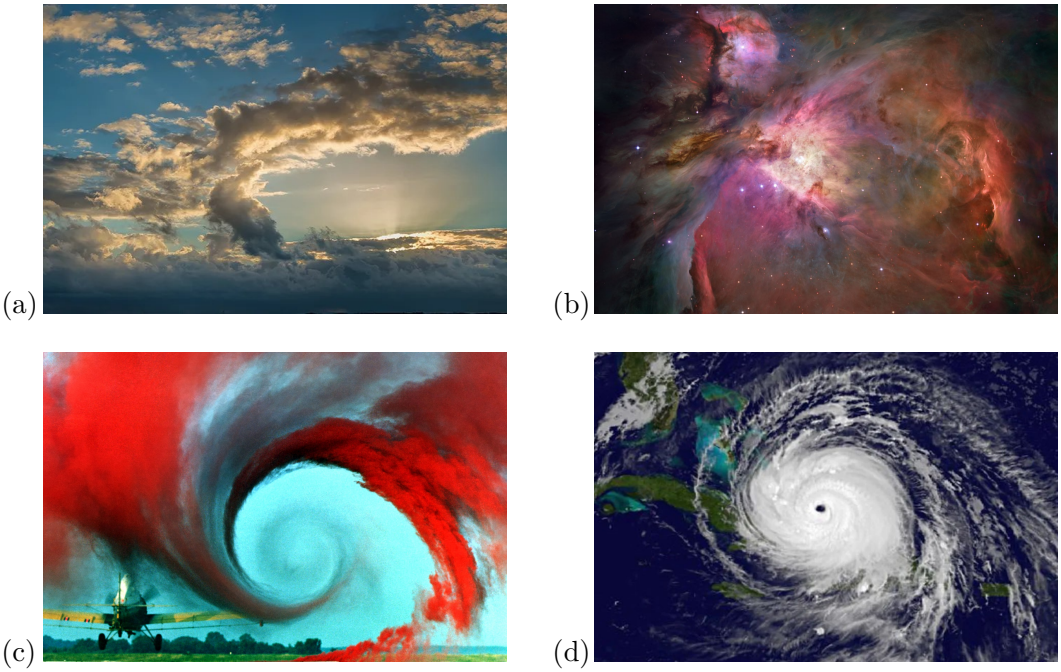

Figure 4.1. Manifestations of self-similarity in real-world turbulence. Disregarding the different sizes and velocities of the phenomena, there is evident visual similarity between clouds (a) and nebulae (b), but also between vortices in air (c) and hurricanes (d)[2].

which produce the following non-dimensional NS equation:

$$D_{t'}\boldsymbol{u}' = -\boldsymbol{\nabla}' p' + \frac{1}{\mathrm{Re}}\Delta'\boldsymbol{u}' + \boldsymbol{f}' \tag{4.6}$$

where $\boldsymbol{\nabla}'$ and Δ' involve derivations with respect to x', y', z'. In this rescaled version only one non-dimensional parameter is left in the equation, the so-called *Reynolds number*:

$$\mathrm{Re} = \frac{LU}{\nu} \ . \tag{4.7}$$

Usually the generic scales L and U are considered with specific physical meaning, L representing a characteristic macroscopic length of the flow (e.g. diameter of the pipe, linear size of the container) and U the mean fluid velocity. In case no physical boundaries are present, one takes L as the length scale where energy is mostly injected, and U can also be the root-mean-square (rms) velocity of the velocity field. By dimensional analysis one sees that (4.7) measures the relative strength of the the inertial advective term with respect to the dissipative viscous term, namely $\mathrm{Re} \sim \frac{\boldsymbol{u}\cdot\boldsymbol{\nabla}\boldsymbol{u}}{\nu\Delta\boldsymbol{u}}$. The higher the Reynolds number, the more the inertia will keep the fluid in a state of motion, and the less the internal friction will be effective in bringing

[2]Source of photos: (a) `https://www.sciencefocus.com/planet-earth/what-gives-clouds-their-shape-a-scientist-explains`; (b) `https://hubblesite.org/contents/media/images/2006/01/1826-Image.html`; (c) `https://en.wikipedia.org/wiki/Wake_turbulence`; (d) `https://www.nasa.gov/centers-and-facilities/goddard/irma-atlantic-ocean/`.

the flow to rest. This is why high-Re fluids are of turbulent nature and low-Re ones are laminar. It follows from the definition (4.7) that the fully-developed turbulent regime can also be expressed as the limit $\mathrm{Re} \to \infty$.

The rescaled version (4.6) of the NS equation entails the famous *similarity law* in fluid mechanics [19]: two flows with different length scales, viscosity and nature will manifest similar behaviour in their evolution if they have the same Reynolds number. Otherwise stated, one can pass from one flow to the other by simply changing measurement units. In Figure 4.1 we show two instances of self-similarity: despite the enormous difference in time- and length-scales, the appearance of clouds does not differ much from the gas formations in a nebula, and the same goes comparing a vortex produced by the wing of an airplane with the shape of an hurricane.

Two parallel and somehow independent lines of research have developed in order to unravel the "turbulence problem" [77]. There is a statistical point of view, stemming from the influencial work of Taylor and Kolmogorov, whose interest lies in analyzing statistical properties of a turbulent flow. The relevance of such approach is demonstrated by the influence that the Kolmogorov theory [78, 79], often dubbed K41, still retains in modern research. About the topic of symmetries, it is observed that dynamical symmetries which get broken in a turbulent flow are restored in a statistical sense as Re grows [6]. The other point of view is the deterministic or dynamical one. The fluid is a mechanical system, effectively described by Newton's law, thus peculiar properties like coherent structures and vortices, should be investigated from a dynamical perspective. To this latter group one normally includes engineering applications and numerical modeling of physical, geophysical and environmental interest.

In the following Sections we will focus on the statistical mechanical approach to fluid dynamics, first for perfect (or ideal) fluids, where $\nu = 0$ and no energy input is present, and then in the turbulent case in which the scale separation between forcing and dissipation generates all the nontrivial effects observed in real fluids.

4.2 Ideal fluids and equilibrium statistical physics

There are fundamental differences between an ideal fluid, described by the Euler equation (4.3), and a viscous one, following the Navier Stokes equation (4.1). While the latter system, as we saw from the spectral representation in Section 4.3.1, is subject to an average energy flux directed from large to small scales, due to the presence of a large-scale source and a small-scale sink of energy, the former constitutes an isolated system and the total energy

$$E(t) = \int d\boldsymbol{r} |\boldsymbol{u}(\boldsymbol{r}, t)|^2 / 2 \tag{4.8}$$

is conserved at each time. Ideal fluids in two space dimensions possess another positive-definite conserved quantity, the enstrophy:

$$\Omega(t) = \frac{1}{2} \int |\boldsymbol{\omega}(\boldsymbol{r}, t)|^2 \, d\boldsymbol{r} \ , \tag{4.9}$$

where $\boldsymbol{\omega}(\boldsymbol{r}, t) = \boldsymbol{\nabla} \times \boldsymbol{u}(\boldsymbol{r}, t)$ is the fluid vorticity. In 2D the vorticity reads $\boldsymbol{\omega} = (0, 0, \omega)$: the only non-zero component is perpendicular to the xy plane of the fluid,

so vorticity is treated like a scalar. In physical terms, a large number of vortical structures with high angular velocity correspond to a large value of the enstrophy (in 2D or 3D). On the other hand, three-dimensional ideal fluids have a different second conserved quantity which is not positive-definite, the helicity:

$$H(t) = \frac{1}{2} \int \boldsymbol{u}(\boldsymbol{r}, t) \cdot \boldsymbol{\omega}(\boldsymbol{r}, t)\, d\boldsymbol{r} \ , \tag{4.10}$$

which represents the degree of chirality of the flow, or also how much the vortex lines are tangled [80]. We will now briefly discuss how perfect fluids can be studied in the framework of equilibrium statistical mechanics, and then some considerations about the difference between 2D and 3D will follow.

The study of equilibrium statistical mechanics in hydrodynamic models began in the 50's, with major independent contributions from Hopf, Lee and Kraichnan [37]. The NS equation in Fourier space (4.24) roughly resembles an evolution equation for non-linearly interacting modes. To retain only a finite number of them a truncation of the available wave vectors is needed, for instance those whose moduli fall in the range $(k_{\min}, k_{\max})$, alongside a discretization of $\boldsymbol{k}$-space [3]. As a result there will be a finite set of N interacting variables $\{y_a\}_{1 \le a \le N}$, whose evolution in phase space reads:

$$\frac{dy_a}{dt} = \sum_{\substack{b,c \\ b \neq a \neq c}}^{1,N} A_{abc}\, y_b\, y_c \tag{4.11}$$

where $A_{abc} = A_{acb}$ are constant coefficients. In Section 4.3 we will write the NS equation in Fourier representation, and one can notice that Eq. (4.11) is formally identical to the Fourier representation of the nonlinear term (see (4.23) below). By construction the phase-space flow is volume-preserving, i.e.

$$\sum_a \frac{d}{dy_a} \left(\frac{dy_a}{dt} \right) = 0 \ , \tag{4.12}$$

and the conservation of the total energy $\sum_a y_a^2$ is valid if: $A_{abc} + A_{bca} + A_{cab} = 0$. The incompressibility of phase-space flow and the presence of a global conserved quantity allows to exploit the microcanonical formalism of equilibrium statistical mechanics, which leads to concluding that the distribution of points in phase space is non-zero only on the hypersurface of constant total energy. This sharp constraint can be relaxed in the canonical ensemble, which yields a Gaussian distribution for the y's:

$$P(y) \propto \exp\{-\alpha \sum_a y_a^2\} \tag{4.13}$$

where α plays the role of an inverse temperature. A notable feature is that $\langle y_a^2 \rangle$ is independent of a, implying energy equipartition among the variables. From the definition (4.29) the energy spectrum will follow the power law $\tilde{E}(k) \sim k^2$, and the mean energy per unit mass will then be: $E \sim k_{\max}^3$. This means that a realistic ideal fluid described by the full Euler equation (with $k_{\max} \to \infty$) will never reach a state of statistical equilibrium.

[3] It is of course more convenient to get to this point by not taking the limit $L \to \infty$ after having performed the discrete Fourier transform of the Euler equation in a box of finite size L.

However energy is not the only conserved quantity: the presence of additional ones add further dynamical constraints in phase space and will thereby modify the equilibrium state. In 2D we can define the enstrophy as: $\Omega = \sum_a k_a^2 y_a^2$, where k_a is the wavenumber corresponding to the variable y_a. With two quadratic conserved quantities the canonical distribution is:

$$P(y) \propto \exp\{-\sum_a (\alpha + \beta k_a^2) y_a^2\} \tag{4.14}$$

which now gives an a-dependent second moment

$$\langle y_a^2 \rangle \propto \frac{1}{\alpha + \beta k_a^2} \ . \tag{4.15}$$

In this case, perfect energy and enstrophy equipartitions are recovered only in the cases $\beta = 0$ and $\alpha = 0$ respectively, yet energy equipartition appears in first approximation also for small k_a, where $\langle y_a^2 \rangle \sim \alpha^{-1}$, whereas in the range of large wave numbers one finds instead enstrophy equipartition: $\langle k_a^2 y_a^2 \rangle \sim \beta^{-1}$. This means that low-$k$ "modes" are dominated by energy, whereas large-k ones by enstrophy, so the spectrum will be peaked at low wavenumbers. In between a smooth transition between the k_a^0 and k_a^{-2} slopes of the modal energies is observed. It is worth mentioning that the possibility to have $\alpha < 0$ while ensuring the necessary constraint of a positive energy spectrum opens the way to the study of negative-temperature states, originally studied by Onsager [81] in a Hamiltonian system of point-vortices on a plane [82].

The situation in 3D is less straightforward: helicity is still quadratic but is not positive-definite - it is actually a pseudoscalar. Defining a linear combination of energy and helicity in truncated Fourier space, Kraichnan [83] showed that the velocity and helicity variances per unit volume associated to wavevector $\boldsymbol{k}$ are:

$$U(k) = \frac{2\alpha}{\alpha^2 - \beta^2 k^2} \qquad Q(k) = \frac{2\beta k^2}{\alpha^2 - \beta^2 k^2} \ , \tag{4.16}$$

and the integrability of the canonical probability distribution is ensured provided $\alpha > 0$ and $|\beta k_{\max}| > \alpha$. This implies that negative-temperature equilibrium states are not admitted in truncated 3D flows.

4.3 Statistical approach to fluid mechanics

4.3.1 Fluids in Fourier space

Before actually delving into statistical fluid mechanics it is quite necessary to delineate the advantages of recasting the NS equation in spectral representation.

When observing a liquid or gas in turbulent motion, the most striking feature that catches one's attention is the widespread presence of fluid structures changing shape and size in an sort of unpredictable fashion. For instance it is not rare to see some vortex-like structure forming, becoming smaller and smaller until disappearing. Depending on geometrical features of the flow, one could also witness vortices increasing progressively in size, maybe also merging. Such observations make clear

that the notion of *length scale* plays a central role in the study of turbulence phenomenology. As it turns out, the physics at the larger scales differs considerably from that at the smallest (molecular) scales, and it is natural to ask what happens at an intermediate range of scales between the two extremes.

When our system shows "regular" statistical properties, which we will introduce shortly, it is extremely useful to abandon the conventional formulation in coordinate space and instead work in *Fourier space*, where the wavevectors $\boldsymbol{k}$ and especially their moduli k offer a natural description of the length scales of our fluid.

At the conceptual basis of the K41 theory, which will be the topic of the next Section, lie two significant statistical features that the turbulent system ought to possess:

- **homogeneity**, meaning that the fluid is statistically invariant under space translations;
- **isotropy**, meaning that the fluid is statistically invariant under space rotations.

These properties are not only mathematical abstractions to facilitate computations: in a highly turbulent and spatially extended flow it is not unrealistic to suppose that the average measurements in one point in space are equivalent to those in another point, and the same should apply for measurements at different orientations (at least at sufficiently small scales).

Once again we exploit the simplification brought by considering our homogeneous turbulent flow to be cyclic within a box of size ℓ: in this way, filling the whole space with an infinite number of boxes, one constructs a periodic velocity field $\boldsymbol{u}(\boldsymbol{r},t)$ of period ℓ in all space directions. Such field can be expressed as a Fourier series, so that in 3D one has [77]:

$$\begin{aligned}\boldsymbol{u}(\boldsymbol{r},t) &= \left(\frac{2\pi}{\ell}\right)^3 \sum_{n_1,n_2,n_3=-\infty}^{+\infty} e^{(i2\pi/\ell)(n_1x+n_2y+n_3z)}\ \tilde{\boldsymbol{u}}_B(n_1,n_2,n_3,t) = \\ &= \left(\frac{2\pi}{\ell}\right)^3 \sum_{n_1,n_2,n_3=-\infty}^{+\infty} e^{(i2\pi/\ell)\boldsymbol{k}\cdot\boldsymbol{r}}\ \tilde{\boldsymbol{u}}_B(\boldsymbol{k},t)\ ,\end{aligned} \tag{4.17}$$

where $(n_1,n_2,n_3)\in\mathbb{Z}^3$ and having introduced the wavevector

$$\boldsymbol{k} = \left(\frac{2\pi}{\ell}n_1, \frac{2\pi}{\ell}n_2, \frac{2\pi}{\ell}n_3\right)\ . \tag{4.18}$$

$\tilde{\boldsymbol{u}}_B(\boldsymbol{k},t)$, where the pedix B stands for 'box', is the discrete Fourier transform of the periodic velocity $\boldsymbol{u}(\boldsymbol{r},t)$. In the limit $\ell\to\infty$, namely when the box occupies the whole space and hence the flow is not necessarily periodic, the series becomes an integral and we get the definition of the (inverse) integral Fourier transform:

$$\boldsymbol{u}(\boldsymbol{r},t) = \left(\frac{1}{2\pi}\right)^3 \int d\boldsymbol{k}\ e^{i\boldsymbol{k}\cdot\boldsymbol{r}}\tilde{\boldsymbol{u}}(\boldsymbol{k},t)\ , \tag{4.19}$$

which can be inverted to give:

$$\tilde{\boldsymbol{u}}(\boldsymbol{k},t) = \int d\boldsymbol{r}\ e^{-i\boldsymbol{k}\cdot\boldsymbol{r}}\boldsymbol{u}(\boldsymbol{r},t)\ . \tag{4.20}$$

From here on, quantities like $\tilde{f}$ denote the Fourier transform of the corresponding quantity f in coordinate space. Since the field $\boldsymbol{u}(\boldsymbol{r},t)$ is real, then its Fourier transform is such that $\tilde{\boldsymbol{u}}^*(\boldsymbol{k},t) = \tilde{\boldsymbol{u}}(-\boldsymbol{k},t)$, where the asterisk denotes complex conjugation.

Let us now consider the NS equation (4.1) with the incompressibility condition (4.2). The purpose is to write its equivalent formulation in Fourier space [77]. Since partial differentiation with respect to r_j $(j = 1, 2, 3)$ becomes multiplication by ik_j when passing to Fourier space, and similar relations apply to the operators $\boldsymbol{\nabla}$ and Δ, one easily sees that the divergence-free constraint becomes:

$$\boldsymbol{k} \cdot \tilde{\boldsymbol{u}}(\boldsymbol{k},t) = 0 \ . \tag{4.21}$$

This implies that the spectral velocity lies in a plane perpendicular to $\boldsymbol{k}$. In turn, terms like $\partial\tilde{\boldsymbol{u}}/\partial t$ and $\nu k^2\tilde{\boldsymbol{u}}$ belong to that plane, while the pressure gradient $i\boldsymbol{k}\tilde{p}$ is parallel to it, so the latter will not appear in our sought equation. The term which is less straightforward to write in Fourier representation is $\boldsymbol{u}\cdot\boldsymbol{\nabla}\boldsymbol{u}$, but we know in advance that we shall consider only its projection onto the plane perpendicular to $\boldsymbol{k}$. To this end let us introduce the projection operator

$$P_{ij}(\boldsymbol{k}) = \delta_{ij} - \frac{k_i k_j}{k^2} \tag{4.22}$$

such that $P_{ij}(\boldsymbol{k})a_j$ (from here on, Einstein notation on repeated indices is considered) represents the i-th component of the projection of $\boldsymbol{a}$ onto the plane normal to $\boldsymbol{k}$. It follows that the transform of the advection term $u_j\,\partial u_i/\partial x_j$ reads:

$$ik_m P_{ij}(\boldsymbol{k}) \int_{\boldsymbol{p}+\boldsymbol{q}=\boldsymbol{k}} d\boldsymbol{p}\ \tilde{u}_j(\boldsymbol{p},t)\tilde{u}_m(\boldsymbol{q},t) \ , \tag{4.23}$$

where the constraint on the allowed wavevectors in the integral derives from the rule that multiplications become convolutions in Fourier space.

We can finally write the component-wise, Fourier-space equivalent of the incompressible NS equation (4.1)-(4.2):

$$\begin{cases} \left(\dfrac{\partial}{\partial t} + \nu k^2\right)\tilde{u}_i(\boldsymbol{k},t) = -ik_m P_{ij}(\boldsymbol{k}) \displaystyle\int_{\boldsymbol{p}+\boldsymbol{q}=\boldsymbol{k}} d\boldsymbol{p}\ \tilde{u}_j(\boldsymbol{p},t)\tilde{u}_m(\boldsymbol{q},t) + \tilde{f}_i(\boldsymbol{k},t) & (4.24) \\ k_i\tilde{u}_i(\boldsymbol{k},t) = 0 & (4.25) \end{cases}$$

Let us notice that the nonlinear advection term in coordinate space has become an interaction among triads of Fourier modes $\tilde{\boldsymbol{u}}(\boldsymbol{k},t)$, $\tilde{\boldsymbol{u}}(\boldsymbol{p},t)$ and $\tilde{\boldsymbol{u}}(\boldsymbol{q},t)$ such that:

$$\boldsymbol{k} = \boldsymbol{p} + \boldsymbol{q} \ . \tag{4.26}$$

It follows that the spectral representation of the flow makes explicit the interaction between different scales of the fluid, which is fundamental in the description and modelling of all transfers occurring from large to small scales and viceversa. All these processes take place only if the triangular relation (4.26) between wavevectors is satisfied. We will see in Section 4.4 how Eq. (4.24) represents the basis for building an extremely simplified model which speeds up considerably computer simulations while retaining the most relevant statistical features of a turbulent fluid.

A very useful quantity to compute in Fourier space is the *energy spectrum*, which indicates how the energy is distributed among different Fourier modes - or generally among different length scales. Let us consider a small portion of wavevector-space, say a parallelepiped of sizes dk_j $(j = x, y, z)$, volume $d\boldsymbol{k}$ and with a corner situated at $\boldsymbol{k}$. Its energy content per unit mass at time t is: $1/2\ |\tilde{\boldsymbol{u}}(\boldsymbol{k}, t)|^2 d\boldsymbol{k}$. We therefore define its ensemble average as:

$$d\tilde{E}(\boldsymbol{k}, t) = \frac{1}{2}\langle|\tilde{\boldsymbol{u}}(\boldsymbol{k}, t)|^2\rangle d\boldsymbol{k} \ , \tag{4.27}$$

where with the brackets $\langle\cdot\rangle$ we indicate a statistical average upon a large collection of independent realizations [77]. Let us point out that $\langle|\tilde{\boldsymbol{u}}(\boldsymbol{k}, t)|^2\rangle$, often called $\tilde{U}(\boldsymbol{k}, t)$ in the literature, is the Fourier transform of the 2nd order velocity correlation function $U(\boldsymbol{r}', t) = \langle\boldsymbol{u}(\boldsymbol{r} + \boldsymbol{r}', t)\boldsymbol{u}(\boldsymbol{r}, t)\rangle$. Due to isotropy, $\tilde{U}$ only depends on the modulus of the wavevector $\boldsymbol{k}$. Integrating (4.27) over all Fourier space yields the mean kinetic energy per unit mass:

$$E(t) = \frac{1}{2}\int_0^\infty \langle|\tilde{\boldsymbol{u}}(k, t)|^2\rangle\ 4\pi k^2\, dk \ , \tag{4.28}$$

We then define the energy spectrum $\tilde{E}(k, t)$ as the kinetic energy density in a spherical shell of internal radius k and width dk, such that the total energy per unit mass is also expressed as $E(t) = \int_0^\infty \tilde{E}(k, t)\ dk$. It follows from (4.28) that:

$$\tilde{E}(k, t) = 2\pi k^2\langle|\tilde{\mathbf{u}}(k, t)|^2\rangle \ . \tag{4.29}$$

In Fourier space the redistribution of energy among spectral components takes the form of a constant average energy flux, directed from large to small scales. This term comes out naturally in the spectral energy balance relation, which we will now describe. It is convenient to start from the evolution in time of the energy spectrum (4.29), in the isotropic case for the sake of simplicity. Computing its time derivative, and exploiting (4.24) one finds the following law:

$$\frac{\partial\tilde{E}(k, t)}{\partial t} = -\langle\tilde{T}(k, t)\rangle - \nu k^2\tilde{E}(k, t) + \langle\tilde{F}(k, t)\rangle \ . \tag{4.30}$$

The first term on the r.h.s. is the average non-linear energy transfer across wavenumber k, which reads [84]:

$$\langle\tilde{T}(k, t)\rangle = \frac{k^3}{2\pi}\int_0^\infty \left[\sin(kr') + 3\frac{\cos(kr')}{kr'} - 3\frac{\sin(kr')}{(kr')^2}\right] B_{ll,l}(r')\, r'^2\, dr' \ , \tag{4.31}$$

having defined the triple correlation

$$B_{ll,l}(r') = \langle u_l^2(\boldsymbol{r}) u_l(\boldsymbol{r} + \boldsymbol{r}')\rangle \tag{4.32}$$

written in terms of u_l, the projection of the velocity field along the r' direction. Instead $\langle\tilde{F}(k, t)\rangle$ is the average injection rate of spectral energy.

At this point one can write an *energy budget* relation for the energy contained in a spherical shell in Fourier space of radius K. Integrating the balance equation (4.30) from 0 to K one gets:

$$\frac{\partial}{\partial t}\left[\int_0^K \tilde{E}(k,t)\,dt\right] = -\int_0^K \langle\tilde{T}(k,t)\rangle\,dk - \nu\int_0^K k^2\,\tilde{E}(k,t)\,dk + \int_0^K \langle\tilde{F}(k,t)\rangle\,dk = \\ = -\langle\tilde{T}_K(t)\rangle - \nu\langle\tilde{\Omega}_K(t)\rangle + \langle\tilde{F}_K(t)\rangle\ . \tag{4.33}$$

Above we have introduced the notation according to which a quantity with index K is its integral computed up to wavenumber K, e.g. its low-pass-filtered version [6]. The dissipative term in the above relation depends on the enstrophy, defined in coordinate space in Eq. (4.9). In Fourier space its ensemble average, again in the homogeneous isotropic case, reads:

$$\langle\Omega(t)\rangle = \int_0^\infty k^2\tilde{E}(k,t)\,dk\ . \tag{4.34}$$

On the other hand $\langle\tilde{T}_K(t)\rangle$ is the *average spectral flux of energy*, namely the average rate at which energy flows (in the outward direction) through a spherical surface of radius K and unit area.

Taking the limit $K\to\infty$ of (4.33) we obtain an energy balance equation for the whole k-space. Assuming that for long times the total energy reaches a statistically stationary value, and considering that the integrated transfer term equals zero due to energy conservation (no energy can be transferred out of the whole Fourier space), then (4.33) yields:

$$\langle\tilde{F}_\infty(t)\rangle = \nu\langle\tilde{\Omega}_\infty(t)\rangle \equiv \varepsilon\ , \tag{4.35}$$

where we used the notation: $\tilde{A}_\infty(t) = \lim_{K\to\infty}\tilde{A}_K(t)$.

Thus, over long enough times, the average injection rate of energy balances the average dissipation rate, named ε. Furthermore, if the scale (or wavenumber) separation between injection and dissipation is very large then the average spectral flux is constant in the spectral range between these (inverse) scales, and equal to ε. Such range with constant energy flux, where forcing and dissipation are negligible, is called *inertial range*. When this balance condition is reached the energy spectrum assumes a characteristic power-law shape in the inertial range, a feature observed in experiments and explained by Kolmogorov in his 1941 theory.

4.3.2 Turbulent energy cascade and Kolmogorov theory

Understanding and possibly predicting the behaviour of fluids in turbulent motion becomes paramount in the field of climate physics, especially so in the study of weather predictions. In that context, the main aim is making forecasts of the near-future state of the atmosphere, as described by a vast number of atmospheric variables: namely, starting from accurate measurements of the current state, compute the future states by evolving the deterministic, yet chaotic, equations. At the same time, investigating statistical properties can lead to a better understanding of other features, such as steady states, spectral properties and fluxes [20].

The role of L. F. Richardson in this field is of utmost importance. Despite his main interest lied in the practical computation of weather forecasts, he was well aware of Reynolds' work on average properties of turbulent flows. In his famous treatise "Weather Prediction by Numerical Process" he explained the dynamical behaviour of eddies with the following poem-like phrase:

> *[...] big whirls have little whirls that feed on their velocity, and little whirls have lesser whirls and so on to viscosity – in the molecular sense.*

This refrain has indeed become a quite common way to give an intuitive understanding of the phenomenon called *turbulent cascade* [6].

This scenario, often referred to as *Richardson cascade*, indicates the mechanism of turbulent energy transfer occurring in 3D flows. This process moves the energy injected by generic driving forces at large scales (which usually correspond approximately to the linear size of the container) down to the small scales, where energy is converted into heat by molecular viscosity. The "intermediate" range of scales between these two extrema, where the effects of both forcing and dissipation are of lesser importance, is dominated by inertia in the form of nonlinear interactions between eddies. For this reason, these length scales constitute the *inertial range*. The more the injection and dissipation scales are further apart, the wider the inertial range is, and in turn the more turbulent the flow is. As a matter of fact, if ℓ_{in} is roughly the injection scale and ℓ_{out} the dissipative one, then the fully developed turbulent regime $\mathrm{Re} \to \infty$ is attained for the asymptotic limit of infinite scale separation: $\ell_{in}/\ell_{out} \to \infty$.

Experimental energy spectra showing power law decay in the inertial range, as already mentioned in the previous Section, have been observed since the early laboratory measurements. A mathematical justification of this behaviour was provided in the early 40's thanks to the work of Kolmogorov [78, 79], who is universally considered the father of statistical fluid mechanics. In the following we will outline the main aspects of his 1941 works, which became known as "K41 theory".

Of particular interest in K41 theory are the *velocity increments*:

$$\delta\boldsymbol{u}(\boldsymbol{r},\boldsymbol{r}',t) = \boldsymbol{u}(\boldsymbol{r}+\boldsymbol{r}',t) - \boldsymbol{u}(\boldsymbol{r},t) \ , \tag{4.36}$$

and their projection onto the increment direction, the so-called longitudinal velocity increments:

$$\delta u_l(\boldsymbol{r},\boldsymbol{r}',t) = \delta\boldsymbol{u}(\boldsymbol{r},\boldsymbol{r}',t)\cdot\frac{\boldsymbol{r}'}{r'} \ . \tag{4.37}$$

The purpose is understanding the statistics of these velocity differences at varying the distance r' between measurements. Assuming local homogeneity and isotropy implies the independence of average values from $\boldsymbol{r}$ and from the direction of $\boldsymbol{r}'$, therefore one has $\overline{\delta\boldsymbol{u}(\boldsymbol{r},\boldsymbol{r}',t)} = \overline{\delta\boldsymbol{u}(r',t)} = 0$, where we indicated with the overbar the expectation value over the p.d.f. of velocity increments. If the flow is also statistically stationary, the time dependence is dropped as well. Higher-order moments of the projected increment show more interesting properties, so let us introduce the *p-th order longitudinal structure function* as:

$$S_p(r') = \overline{[\delta u_l(r')]^p} \ . \tag{4.38}$$

At this stage Kolmogorov formulated two *similarity hypotheses* [78] to bring forward his study. The first hypothesis states that for locally isotropic turbulence the probability distributions of the velocity increments are uniquely determined by the viscosity ν and the average dissipation rate of energy ε. The second hypothesis adds that, if the separation r' is much larger than the scale ℓ_{out}, where dissipation dominates, then the p.d.f.'s only depend on ε and not on ν. These two assumptions are sufficient to determine a functional law for the second-order structure function in locally homogeneous isotropic turbulence:

$$S_2(r') = C\varepsilon^{2/3}(r')^{2/3} \ , \tag{4.39}$$

where C is a universal nondimensional constant. It is quite remarkable that the (nontrivial) derivation by Kolmogorov can be bypassed, and (4.39) readily obtained by simple dimensional analysis. The physical dimensions of ε and r are respectively $[\mathrm{L}]^2\,[\mathrm{T}]^{-3}$ and $[\mathrm{L}]$, and their only combination providing the dimensions $[\mathrm{L}]^2\,[\mathrm{T}]^{-2}$ of S_2 is the one appearing in (4.39). This power-law behaviour for the mean squared velocity difference matched quite nicely experimental measurements already performed at that time, and this further contributed to the success of Kolmogorov theory.

Closely related to this result is the prediction of the power-law shape of the energy spectrum $\tilde{E}(k)$ defined in (4.29). Indeed, the energy spectrum $E(k)$ is related to the Fourier transform of the velocity correlation function $\langle u(x)u(x+r')\rangle$. Associating to r' a wavenumber $k \sim 1/r'$, the following power-law behaviour naturally follows:

$$\tilde{E}(k) = C'\varepsilon^{2/3}k^{-5/3} \ , \tag{4.40}$$

with C' another nondimensional constant.

Another influential work published by Kolmogorov, again in 1941 [79], led to the celebrated "4/5 law", which is one of the few exact results in statistical fluid mechanics. Assuming as before homogeneous and isotropic turbulence, the law states that the third-order longitudinal structure function $S_3(r)$ is linked to the second-order one $S_2(r)$ by:

$$S_3(r) = -\frac{4}{5}\varepsilon r + 6\nu\frac{dS_2(r)}{dr} \ . \tag{4.41}$$

This is an exact result in the sense that no approximation - besides homogeneity and isotropy - has been introduced in the derivation. Yet this law is mostly known in the $r \gg \ell_{out}$ case, where the second term on the r.h.s. is negligible in comparison with the first so that:

$$S_3(r) \simeq -\frac{4}{5}\varepsilon r \ . \tag{4.42}$$

This law has quite important implications. The immediate one is that it explicitly provides a power-law behaviour for $S_3(r)$ with exponent equal to 1. Since this comes from an exact result, we expect this linear dependence to be observed even in real turbulence, at least in homogeneous and isotropic settings. Furthermore, considering that for large distances $S_3(r)$ is always negative, then the probability distribution of the velocity differences is negatively skewed. It is possible to show that the third-order structure function is directly related to the average energy flux in the

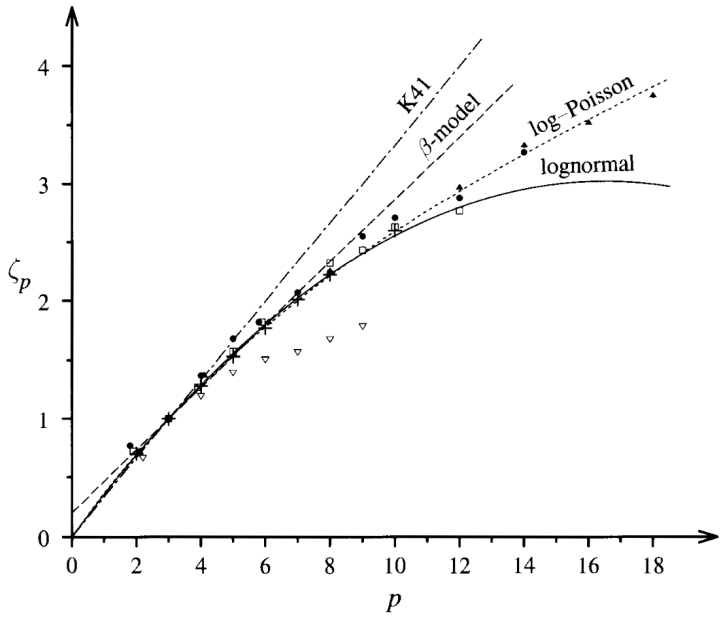

Figure 4.2. Anomalous exponents ζ_p of the structure functions for increasing order p. Symbols are measurements from different experiments. The dash-dotted line is the K41 linear prediction $\zeta_p \sim p/3$. The other lines are obtained from three predictive models, some of which will be mentioned later. Figure from [6].

inertial range, thus its constant sign is a manifestation of the transfer of energy in the cascade from large to small scales. From a statistical mechanics point of view, let us point out that a non-zero odd-order moment of a fluctuating quantity is often associated to the presence of a statistical current, and consequently to the absence of statistical equilibrium.

4.3.3 Beyond K41: intermittency and multifractality

Despite the success of Kolmogorov theory in predicting spectra and correlations in real turbulence, some of the predictions appeared to show some fallacies. For instance, trusting dimensional analysis one would find for the p-th order structure function the scaling law $\varepsilon^{p/3}\,(r')^{p/3}$, with the exponents growing linearly in p (the so-called Kolmogorov exponents). This dependence would imply a perfect self-similarity of the structure functions: two values of S_p measured at different space-separations r' are trivially linked by a simple rescaling of space and velocity. This is why K41 is often said to describe a fractal structure of turbulence. Results from experiments and numerical simulations revealed that the exponents of the structure functions are indeed *anomalous*, namely they present a nonlinear dependence on the order of the moment. As it can be appreciated in Figure 4.2, the anomalous exponents ζ_p deviate more and more from the linear Kolmogorov expectation as higher-order moments are considered.

This leads us to another feature of turbulence not accounted for by K41 theory: *intermittency*. Following Frisch [6], a random time-dependent function is said to be intermittent when it shows activity (e.g. evident fluctuations) during only a

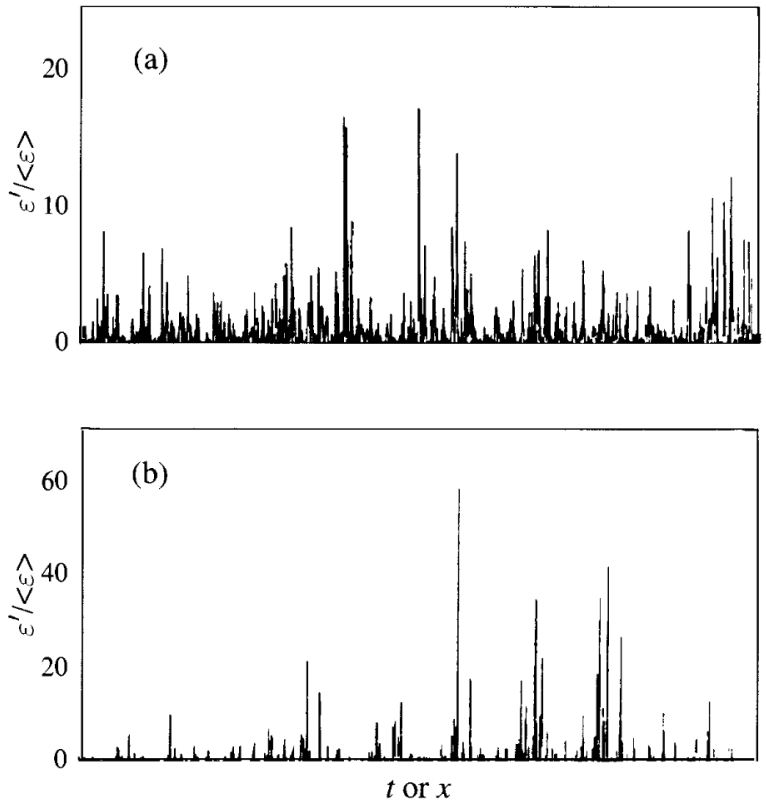

Figure 4.3. Time signals of the average local dissipation rate, normalized by its time-averaged value $\langle\varepsilon\rangle$. Panel (a) is obtained from measurements in a laboratory boundary layer at moderate Re, while panel (b) in the atmospheric surface layer at high Re. Here the space averages are actually computed on a line instead of a volume, for simplifying the experimental procedure. Time and space intervals, on the horizontal axis, are considered on the same footing under Taylor's frozen-flow hypothesis [6]. Figure from [6].

fraction of the time, and the activity decreases as the scale under consideration gets smaller. In the context of turbulence, the most revealing dynamical quantity is the instantaneous dissipation rate of energy. One can write an evolution equation for the energy of a fluid element by just computing the scalar product of the NS equation (4.1) with the velocity field $\boldsymbol{u}(\boldsymbol{r},t)$. Taking the space average, on a small volume V, of the viscous term one obtains the average local dissipation rate ε':

$$\varepsilon'(t) = -\frac{1}{V}\int_V d\boldsymbol{r}'\,\nu\,\boldsymbol{u}(\boldsymbol{r}',t)\cdot\Delta\boldsymbol{u}(\boldsymbol{r}',t)\ . \tag{4.43}$$

After integration by parts and the introduction of the vorticity $\boldsymbol{\omega} = \boldsymbol{\nabla}\times\boldsymbol{u}$, this quantity can be recasted as [40]:

$$\varepsilon'(t) = \frac{1}{V}\int_V d\boldsymbol{r}'\,\nu\,|\boldsymbol{\omega}(\boldsymbol{r}',t)|^2\ . \tag{4.44}$$

Observing a time series of the local energy dissipation rate one notices sudden bursts of the signal separated by longer periods of quiescence, as reported in Figure

4.3. The two panels show two experimental time series of $\varepsilon'(t)$ from a laboratory and an atmospheric flow. At higher Reynolds number (panel (b)) the intermittency of the bursts is more evident. It is necessary to remark that intermittency is not a property confined to the dissipation range: the energy transfers dominating the inertial range are not smooth processes, but occur in bursts in a similar way. But intermittency is not only a temporal phenomenon: the activity is strongly localized also in space, so that one can also talk of spatial intermittency. Spatio-temporal intermittency was first pointed out by Landau [6], who argued that the similarity hypotheses in K41 theory did not take into account the non-universality of the average dissipation rate ε, caused by the random nature of the energy transfer mechanisms. In particular he also mentioned the existence of strong localization of vorticity in limited regions, which is a clear manifestation of spatial intermittency. Landau's remark led Kolmogorov to revise his previous work and present the K62 theory [85]. Regarding the local space average of the energy dissipation, defined in (4.43), Kolmogorov added the further assumption (often referred to as "third Kolmogorov hypothesis") that its logarithm follows a normal distribution if $V^{1/3} \ll L$, where L is the macroscale of the fluid. Also, the variance of such distribution is given by: $\sigma^2 = A + \mu \ln(L/V^{1/3})$, where A and μ are two constants. This modification to the theory yields a correction to the exponents of the structure functions, since:

$$S_p^{(K62)}(r) \sim r^{\frac{p}{3}+\frac{1}{18}\mu p(3-p)} \ . \tag{4.45}$$

Intermittency, introduced as a dynamical mechanisms, has natural consequences on the statistical properties of turbulent flows, which emerge especially when investigating quantities depending on space-time intervals such as the longitudinal velocity increments (4.37). Experiments and simulations show that the computed p.d.f.'s of the velocity increments differ in a substantial way when decreasing the spatial separation r. For large r, of the order of the largest scale of the system, the shape is indistinguishable from a Gaussian with zero mean, however as r becomes smaller the tails of the distribution become heavier and heavier, and for very small separation the p.d.f. becomes similar to a stretched exponential [4]. As a matter of fact, it is customary to associate intermittency to the non-gaussianity of the probability distributions, due to rare but strong dissipative events which increase the tails of the p.d.f.'s.

The anomalous exponents ζ_p presented in Figure 4.2 defied physical interpretation. The existence of a single scaling exponent $h = 1/3$ such that $\delta u_l(r) \sim r^h$ appears inconsistent with the strong fluctuations experienced by the energy dissipation, and is further disproved by the anomalous exponents $\zeta_p \neq p/3$ of the structure functions. While dissipation range intermittency seems to be better understood in terms of singularities of the solutions of the NS equation at complex times [86], the same phenomenon in the inertial range is more elusive.

Among the first studies which tried to understand intermittency at the level of the energy cascade is the so-called *beta model* by Frisch, Sulem and Nelkin [87]. The idea at its core is, similarly to Richardson, to consider the energy cascade as a "multi-step generative process": calling l_0 the scale of the largest eddy, at step n

[4] In Figure 4.6 an instance of the gradual change in the shape of the distribution functions is represented, from numerical simulations performed on a shell model.

the eddies are assumed to have typical sizes $l_n = l_0 r^n$, with $0 < r < 1$. Such eddies generate the eddies at step $n+1$ of sizes l_{n+1}. Whereas in the Richardson cascade the eddies are always space-filling at each step, in the beta model the fraction of volume occupied at step $n+1$ is only a fraction β of the volume occupied at step n. Repeating Kolmogorov analysis with the added hypothesis that a part of the volume is inactive, one can find the following scaling for the structure functions:

$$\zeta_p^{(\beta)} \sim r^{\frac{p}{3}+(3-D)(1-\frac{p}{3})} \ , \tag{4.46}$$

where $(3-D) \equiv \ln\beta / \ln r$. However the anomalous exponents provided by this model are again linear in the order p, so there is no agreement with the concave shape, which emerges from experimental data.

It was understood that a smooth curved line for ζ_p could not be obtained with a single scaling exponent h, and neither with a finite number of h's. Therefore, the novel idea of Parisi and Frisch [38] was to assume a continuum of scaling exponents, ranging from h_{min} to h_{max}. Before delving into this theory, it is important to point out that the scaling exponent h is what mathematicians call the Hölder exponent which appears in the Hölder continuity condition for a function f: $||f(x) - f(y)|| \leq C||x-y||^h$. A physical restatement of this condition, applied to our context, is that the velocity field develops a singularity of order $h > 0$ at a point $\boldsymbol{r}$ if:

$$\lim_{\boldsymbol{r}\to\boldsymbol{r}'} \frac{||\boldsymbol{u}(\boldsymbol{r}) - \boldsymbol{u}(\boldsymbol{r}')||}{||\boldsymbol{r}-\boldsymbol{r}'||^h} \neq 0 \ . \tag{4.47}$$

The Kolmogorov estimate $h = 1/3$ implies that the velocity field is not smooth, but only Hölder continuous of order 1/3, making the existence of singularities possible. Mandelbrot [88] proposed that singularities are concentrated on a set $A \in \mathbb{R}^3$ having non-integer (fractal) Hausdorff dimension. Let us define the set of points in which we have a singularity of order h as $S(h)$, and the Hausdorff dimension of such set as $d(h)$. In fully developed turbulence $d(h)$ is not a trivial function of h: sets of point associated to different singularity exponents will have different dimensions. Moreover the ensemble of all fractal sets $S(h)$ at varying h form a hierarchical structure, since if $h < h'$ then $S(h) \subset S(h')$: this ensemble, in the literature, is called *multifractal* set, and the model developed by the two authors based on this formalism became known as *multifractal model*.

At this point it would be useful to link the Hausdorff dimension $d(h)$ to the anomalous exponents ζ_p of the longitudinal structure functions. In order to do so we can adopt a probabilistic viewpoint, and consider that the probability of a point $\boldsymbol{r}$ to develop a singularity with exponent h - namely that $||\boldsymbol{u}(\boldsymbol{r}) - \boldsymbol{u}(\boldsymbol{r}')|| \overset{r\to r'}{\sim} ||\boldsymbol{r}-\boldsymbol{r}'||^h$ - goes to zero as $||\boldsymbol{r}-\boldsymbol{r}'||^{3-d(h)}$ when $||\boldsymbol{r}-\boldsymbol{r}'|| \to 0$ [5]. From this, one could write the structure functions as:

$$\langle(\delta u(r))^p\rangle \propto \int d\mu(h) \left(\frac{r}{\ell_{in}}\right)^{3-d(h)} (\varepsilon r)^{ph} \ , \tag{4.48}$$

where $d\mu(h)$ is a measure on the region where $d(h) > 0$, and ℓ_{in} is again the scale of energy injection. The integral can be evaluated with the saddle-point method, leading

[5] The reason for this non-intuitive relation between the probability of a singularity occurrence and the "codimension" $(3-d(h))$ is made very clear by Frisch's pedagogical explanation in [6, section 8.5.1].

for the multifractal model to the prediction $S_p^{(\mathrm{MF})}(r) \sim r^{\zeta_p^{(MF)}}$ where, neglecting small corrections:

$$\zeta_p^{(\mathrm{MF})} = \min_h \{ph + 3 - d(h)\} \ . \tag{4.49}$$

In this theory, the anomalous exponents are the Legendre transforms of the codimension of the set $S(h)$. This definition assures the convexity property observed in experimental data, since Legendre transforms are inherently convex. An explicit formula for (4.49) cannot be found unless an expression for the dimension $d(h)$ is known. This is the main drawback of this model, since experiments can have no access to this quantity (besides, of course, computing it via inverse Legendre transform by using the ζ_p's measured from the velocity increments), nor it can be, at least currently, derived from first principle, i.e. from the NS equation. It is noteworthy that the structure function of order p is determined by a single value of h, the one whose set $S(h)$ of singular points has Hausdorff dimension satisfying the minimization constraint of the transform.

Benzi, Paladin, Parisi and Vulpiani [89] then generalized the beta model to take into account such multifractal structure, presenting the *random beta model*. The progressive rarefaction of the active regions by a factor β, as the cascade progresses, is still valid, but now $\beta = \beta_n^{(i)}$ is a random variable independently extracted, at each step n of the cascade and for each eddy i present at that step, from a probability distribution $P(\beta)$. Using the constancy of the energy flux in the inertial range to build a recursive equation for the velocity at step n, it is possible to compute the predicted exponents of the structure functions:

$$\zeta_p^{(\text{rand-}\beta)} = \frac{p}{3} - \log_2 \left\{ \int d\beta P(\beta) \beta^{1-p/3} \right\} \ . \tag{4.50}$$

The authors showed that, with the fairly simple p.d.f. $P(\beta) = x\,\delta(\beta - 1/2) + (1-x)\,\delta(\beta - 1)$ and choosing the free parameter $x = 1/8$, a good fit with the experimental data is obtained. Naturally there is no reason to prefer this bimodal $P(\beta)$ to any other, as well as that specific value of x.

Ten years later, another phenomenological model attempted to explain intermittent corrections to the scaling laws. The study by She and Leveque [90] starts by defining the p-th order energy dissipation structures at inertial-range scale r by: $\varepsilon_r^{(p)} = \langle \varepsilon_r^{p+1} \rangle / \langle \varepsilon_r^p \rangle$, where ε_r is the energy dissipation rate averaged in a ball of size r, as that of K62 theory [85]. The endpoints of this hierarchical structure are $\varepsilon_r^{(0)} = \langle \varepsilon_r \rangle$ and $\varepsilon_r^{(\infty)}$, where the latter is the most intermittent structure, assumed to be an isolated filament. Under the assumption that the scaling of $\varepsilon_r^{(p+1)}$ only depends on $\varepsilon_r^{(p)}$ and $\varepsilon_r^{(\infty)}$, the solution of a recursive relation leads to:

$$\varepsilon_r^{(p)} \sim r^{\tau_p} \ , \tag{4.51}$$

in which:

$$\tau_p = -(2/3)p + 2[1 - (2/3)^p] \ . \tag{4.52}$$

Since K62 theory provides the following relation between the exponents τ_p of the average dissipation rate and those of the structure functions ζ_p:

$$\zeta_p = p/3 + \tau_{p/3} \ , \tag{4.53}$$

one ends up finding:

$$\zeta_p^{(\mathrm{SL})} = \frac{p}{9} + 2\left[1 - \left(\frac{2}{3}\right)^{p/3}\right] . \tag{4.54}$$

The advantage of the present model is that it has no free parameters, but it substantially relies on the correctness of K62 theory.

The models that have been introduced in the last decades in order to predict the intermittent statistics of the turbulent energy cascade are phenomenological: they make strong assumptions on the underlying nature of the process, based on observations or on reasonable hypotheses. A major open problem in turbulence is whether it is possible to explain intermittency from first principles, i.e. starting from the dynamics of the Navier Stokes equation.

4.4 Shell models

Hydrodynamic turbulence is fundamentally a multiscale phenomenon: the nontrivial dynamical behaviour is to be traced to the interactions taking place among fluid structures characterized by different length and time scales. For instance, our atmosphere sees the coexistence of giant coherent structures, hundreds of kilometers in size, like hurricanes and cyclones, with tiny fluctuations just above the molecular scale. As already stated in Section 4.1, in order to properly speak of turbulence there must be a considerable separation - several orders of magnitude - between the largest and smallest scales.

This poses a serious problem in Computational Fluid Dynamics (CFD). The optimal space discretization using a mesh of points should require both a highly refined grid for capturing the sub-millimeter physics and, at the same time, a giant extent of the whole mesh for studying the largest structures which carry most of the energy. Performing these computations is unfeasible even for modern computers: state of the art Direct Numerical Simulations (DNSs) have reached $8192^3 \sim \mathcal{O}(10^{11})$ grid points, corresponding to $\mathrm{Re} \sim \mathcal{O}(10^6)$, whereas in atmospheric turbulence the Reynolds number can be even 1000 times larger. Each of these grid points must store relevant physical information (velocity components, but also density and temperature) and computations are continually performed on them - principally spatial derivatives.

Also time discretization is necessary for reproducing the dynamics of relevant observables, and a similar issue arises here as well. The time step cannot be too large since the dynamics of the fastest eddies would not be reproduced accurately, aside from numerical instabilities. The errors would propagate to larger and slower structures [61], making the whole simulation of the fluid completely unphysical. On the other side, the time evolution must be continued long enough, otherwise the large structures would not change appreciably. In this respect, long-time behaviours are measured in terms of the *large eddy turnover time*, whose duration can be quite long: in atmospheric boundary layers it ranges from several minutes to over an hour. Reliable statistics can be gathered only if the modelled fluid has evolves for many large eddy turnover times. The bottom line is that CFD based on the NS equation is a serious challenge, requiring huge computational power and state-of-the-art hardware (cluster computers, GPUs) not available in all facilities.

It is also true that physicists often aim at understanding and predicting the behaviour of complex natural phenomena, with either known or unknown dynamical equations, by means of models which are simplified, but yet preserving the main physics. In principles, models should reproduce the most crucial parts of the observed physical system, even if that means disregarding other aspects which are deemed secondary, but at the same time they must introduce simplified equations for permitting better analytical and computational investigations. Notable examples of physical modelling include: the Lorenz63 model, which transformed the nontrivial dynamics of thermal convection in the atmosphere in a system of three ODEs; the Lotka-Volterra equations, describing the population dynamics of predators and preys; the Ising model, reproducing some magnetic properties in solid matter using two-state variables. Indeed, scientists interested in atmospheric physics often test new ideas and approaches on simple models like the Lorenz63 and the Lorenz96 - the latter of which has been thoroughly discussed in Chapter 3 - before moving to more faithful but complex models.

The need for simplification is especially felt in turbulence: the mathematics involved in the NS equation is far from being tractable, and in Fourier space there is not much simplification since we find an enormous number of nonlinear interactions between modes. This hinders the possibility to analyze features like cascades, asymptotic features and intermittency. A turning point for the modelization of turbulent systems arrived in the 1970's from the Soviet school, where the *shell models* [22, 39, 40] were conceived.

The basic idea of shell models is to consider a discrete, finite set of N wavenumbers $k_n,\ n = 1, \dots, N$, which can be seen as radii of Fourier-space spherical shells. These wavenumbers are exponentially-spaced as:

$$k_n = k_0 \lambda^{n-1} \tag{4.55}$$

where k_0 is the radius of the smallest shell, and $\lambda > 1$ is a free parameter, which determines how fast the growth of Fourier-space shells is. In Figure 4.4 a schematic representation of the spherical shells is provided. The mostly used value is $\lambda = 2$, however other studies have been conducted with alternative values since it was noticed that $\lambda = 2$ does not allow the triangle relation $\boldsymbol{k} = \boldsymbol{p} + \boldsymbol{q}$ between wavevectors belonging to interacting modes. To each shell is associated a single shell variable (or velocity) $u_n(t)$, either real or complex, which is a surrogate of the velocity fluctuations observed at scales $\sim k_n^{-1}$. Even though there is no direct mathematical relation between the real-space velocity field $\boldsymbol{u}(\boldsymbol{r}, t)$ or its Fourier transform $\tilde{\boldsymbol{u}}(\boldsymbol{k}, t)$ and the shell velocities $u_n(t)$ just defined, a possible physical meaning can be attributed to the latter by considering them as shell-averaged Fourier coefficients, like:

$$u_n(t) \quad \longleftrightarrow \quad \frac{1}{k_{n+1} - k_n} \int_{k_n}^{k_{n+1}} \tilde{u}(k, t)\, dk \ , \tag{4.56}$$

or else like shell-averaged velocity differences:

$$u_n(t) \quad \longleftrightarrow \quad \frac{1}{k_{n+1} - k_n} \int_{k_n}^{k_{n+1}} \Big[u(r + k^{-1}, t) - u(r, t) \Big]\, dk \tag{4.57}$$

(here we considered velocity fields as scalars, just to convey the idea).

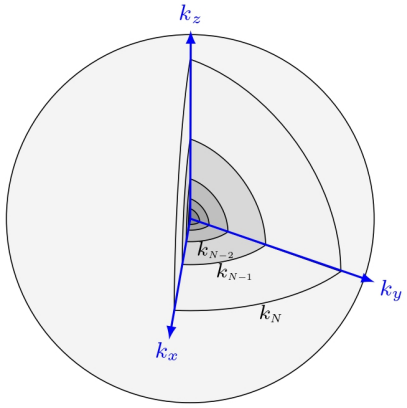

Figure 4.4. Subdivision of Fourier space into spherical shells, whose radii grow according to the exponential law (4.55).

Once we have this reduced set of variables reminiscent of the Fourier-transformed velocity field, it is necessary to provide dynamical equations resembling the structure of the NS equation. In this respect, the presence of triad interactions in the spectral representation (4.24) of the NS equation suggests that the evolution equation of the shell variable u_n should contain a term of the kind $a_n u_{n'} u_{n''}$, with a_n a generic shell-dependent constant which is determined using symmetries and conservation laws of the NS equation. Also, the forcing and dissipative terms can be taken of the same form as (4.24), which in our new variables read f_n and $-\nu k_n^2 u_n$ respectively. To sum it up, all shell models are described by a finite set of ODEs having the following structure:

$$\dot{u}_n(t) = I(\{u_m\}_{m=1,\dots,N}) + D(u_n) + F(u_n) \ , \tag{4.58}$$

in which one recognizes on the r.h.s. the interaction, dissipative and forcing terms. We assumed the most general coupling, with variable u_n interacting with all the other ones.

Examining the different shell models proposed since the 1970's, one can observe that the principal features which discriminate them are:

- the type of shell variables: in the first models the velocities were real numbers, while the latter ones employed complex variables (doubling the number of d.o.f.) because they yielded more realistic results, e.g. chaotic dynamics instead of fixed points;

- the number of shell variables per shell: while most studies have been performed on models with a single variable per shell there have been cases where multiple shell velocities per shell were considered, trying to add a minimum spatial structure into the simplified model;

- the interaction term: besides the constraints imposed by the inviscid invariants, there is enough freedom in the form of the interaction term between triplets

of shell variables (e.g. nearest-neighbors, next-to-nearest-neighbors, or longer-range interactions) [6] .

4.4.1 A tentative history of shell models

In this Section we quickly present, in chronological order, the different minimal turbulent models which have been proposed during the years, all of which would be known as shell models [22, 40]. There is no claim to delineate a complete historical account, but only to track the evolution which these models experienced and to reveal the different features listed in the above bullet points.

1. In 1971 Obukhov [91] first proposed a model with a structure similar to modern shell models, but with no intention to approximate the NS equation. A set of velocities $u_n \in \mathbb{R}$ associated to discrete wavenumbers k_n evolves according to the equation:

$$\dot{u}_n = a_{n-1}u_{n-1}u_n - a_n u_{n+1}^2 - \nu_n u_n \delta_{n>M} + f\delta_{n,1} \ . \tag{4.59}$$

   The first two terms on the r.h.s. represent nonlinear advection, the third is the viscous dissipation acting only on large wavenumbers (beyond k_M) and the fourth is the forcing which injects energy only on the first variable. The advection term conserves the kinetic energy $\sum_n u_n^2/2$: this can be verified by multiplying (4.59) by u_n, summing over all n's and seeing that in absence of forcing and viscosity the r.h.s is zero. However this model does not satisfy Liouville's theorem, namely $d\dot{u}_n/du_n \neq 0$: the phase space flow is not incompressible.

2. In 1973 Gledzer [92] studied a similar model, differing from Obukhov's in the next-to-nearest neighbors interactions and the validity of Liouville's theorem - the latter condition obtained by imposing the independence of the r.h.s. on u_n. The equations read:

$$\dot{u}_n = A_n u_{n+1}u_{n+2} + B_n u_{n-1}u_{n+1} + C_n u_{n-2}u_{n-1} - \nu_n u_n \delta_{n>M} + f_n \ . \tag{4.60}$$

   The lower and upper boundary conditions are: $u_{-1} = u_0 = 0$ and $u_{N+1} = u_{N+2} = 0$. Again the generic coefficients A_n, B_n and C_n can be chosen to conserve two inviscid invariants [7], the energy $E = \sum_n u_n^2/2$ and, for instance, the enstrophy $H = \sum_n k_n^2 u_n^2/2$ as happens in 2D inviscid flows.

3. One year later, in 1974, Desnyansky and Novikov[93] performed a study using a simple model with nearest-neighbors interactions, which evolved according to:

$$\dot{u}_n = k_n \left[u_{n-1}^2 - 2u_n u_{n+1} - 2^{1/3}C(u_{n-1}u_n - 2u_{n+1}^2)\right] - \nu k_n^2 u_n + f_n \ . \tag{4.61}$$

[6] The locality of interactions in the inertial range has been proved in 3D: it is a direct consequence of the k^{-m} shape of the energy spectrum in that range, provided that $1 < m < 3$ [37]. Then, in shell models reproducing 3D turbulence, using nearest-neighbors interactions among shells is not an extreme simplification since they give the major contribution to the energy transfer.

[7] Range-2 interactions between shell variables allow an additional conservation law to be imposed on the nonlinear terms: this will be clearer in the following treatment of the Sabra model in section 4.4.2.

The parameter C is not fixed and determines the scaling behaviour of u_n: for $C < 1$ one recovers the Kolmogorov 5/3 spectrum, while for $C > 1$ the spectrum is not integrable for $k_n \to 0$. Let us point out that, for any value of C, the Kolmogorov scaling $u_n \sim k_n^{-1/3}$ is a stable fixed point of the dynamics, a result which is in contradiction with the anomalous exponents of structure functions. Regardless, this type of model - and generalizations of it - found much popularity in the mathematics community, where it is also called "dyadic model".

4. More than a decade later, in 1989, Ohkitani and Yamada [94] proposed a fundamental change in the Gledzer model (4.60) by using complex shell variables. The resulting model, known as Gledzer-Ohkitani-Yamada (GOY) model, is described by the equations:

$$\dot{u}_n = i\left[A_n u^*_{n+1}u^*_{n+2} + B_n u^*_{n-1}u^*_{n+1} + C_n u^*_{n-2}u^*_{n-1}\right] - \nu k_n^2 u_n + f\delta_{n,4} \ , \quad (4.62)$$

the asterisk indicating complex conjugation. The same zero-valued boundary of the Gledzer model is enforced by imposing $B_1 = C_1 = C_2 = 0$ and $A_{N-1} = A_N = B_N = 0$. Energy conservation is retrieved by assigning the following values to the coefficients:

$$A_n = k_n \ , \quad B_n = -\beta k_{n-1} \ , \quad C_n = (\beta - 1)k_{n-2} \ , \quad (4.63)$$

where $\beta \in \mathbb{R}$ is a free parameter. A second conserved quantity H is present, its explicit form depending on the value of β:

$$H = \sum_{n=1}^{N} k_n^\alpha |u_n|^2 \ , \quad \text{where } \alpha = -\log_\lambda(\beta - 1) \ , \quad (4.64)$$

where λ was defined in (4.55). For instance, choosing $\lambda = 2$, the value $\beta = 5/4$ yields $\alpha = 2$, so that H has the physical dimension of enstrophy. More generally, for $\beta > 1$ the exponent α is a real number (positive if $\beta < 2$), so the second invariant is positive-definite. Instead for $\beta < 1$ the exponent α is a complex quantity:

$$\alpha = -\left[\log_\lambda(1-\beta) + i\pi \log_\lambda e\right] \equiv \mathrm{Re}(\alpha) + i\,\mathrm{Im}(\alpha) \quad \text{if} \quad \beta < 1, \quad (4.65)$$

and the second invariant becomes: $H = \sum_n (-1)^n k_n^{\mathrm{Re}(\alpha)} |u_n|^2$. The physical dimension of helicity is obtained by using $\beta = 1/2$, which corresponds to $\mathrm{Re}(\alpha) = 1$, even though defining an helicity in a model without spatial structure is not straightforward. The success of this model follows from its chaotic behaviour, which is a necessary ingredient to obtain broken scale invariance and anomalous exponents of the structure functions.

5. Nevertheless the GOY model still exhibited some shortcomings (see next section): this motivated L'vov and coworkers to adopt, in 1998, an "improved" shell model renamed Sabra [9]. The main features of such model will be presented in the next Section, since the Sabra model is the one chosen in our numerical studies.

Clearly the history does not end with the Sabra model. Many are the reduced hydrodynamic systems employed in the past decades which are inspired by the original shell models: some have a drastically changed structure, like hierarchical tree models [95], whereas others originated from the will to investigate other phenomena, such as magnetohydrodynamics [96], passive scalar advection [97], helicity in 3D turbulence [98], thermal convection [99] and split cascade [100].

4.4.2 The Sabra shell model

As anticipated, the popular GOY model had some inherent spurious properties, which needed to be removed in order to better reproduce the statistical features of an hydrodynamic system.

In shell models the structure functions are defined as:

$$S_p(n) = \langle |u_n|^p \rangle \ , \tag{4.66}$$

the brackets indicating a time average computed on the stationary state. Their anomalous scaling is a fundamental property, which then must be reproduced by shell velocity moments. In other words, the structure functions (4.66) should scale with shell wave number k_n, in the inertial range, as:

$$S_p(n) \sim k_n^{-\zeta_p} \ , \tag{4.67}$$

where ζ_p is the p-th order anomalous exponent. However, the GOY model presented visible periodic oscillation around the expected power law behaviour. This periodicity is due to the presence of second order correlations between variables in shells separated by multiples of three, i.e.: $\langle u_n u^*_{n+3m} \rangle \neq 0,\ m \in \mathbb{Z}$. Such spurious effect is found also for higher-order correlations, therefore the scaling behaviour is spoiled in the GOY model if the issue is not properly taken into account.

L'vov et al. [9] realized that some minor changes in the nonlinear terms of the GOY equations (4.62) allowed to eliminate the period-three oscillations. The equations of motion of the new model, named Sabra, read:

$$\dot{u}_n = i \left[a k_{n+1} u^*_{n+1} u_{n+2} + b k_n u^*_{n-1} u_{n+1} - c k_{n-1} u_{n-2} u_{n-1} \right] - \nu k_n^2 u_n + f_n \ . \tag{4.68}$$

Let us first point out that both the GOY and Sabra model reproduce the same structure of the NS equation in Fourier space (4.24). In particular the quadratic terms in (4.62) and (4.68) are reminiscent, in form and physical dimensions ($\sim iku_nu_m$), of the triad interaction terms found in the original equation.

Unless explicitly stated, the features we are going to present in the following are shared between GOY and Sabra models. The free coefficients a, b, $c \in \mathbb{R}$ are constrained by the usual conservation laws: multiplying (4.68) by u^*_n and summing from $n = 1$ to $n = N$ one finds that the total energy is constant in time if and only if: $a + b + c = 0$. One of the three coefficients, e.g. a, can be eliminated by dividing the whole Sabra equation by it and absorbing the common factor in the other terms - rescaling thus the time variable, the coefficients b and c, the viscosity and the forcing amplitude. The remaining coefficients are then related by:

$$1 + b + c = 0 \ , \tag{4.69}$$

so there is still a free parameter left. Imposing the conservation of a second global quantity $H = \sum_n k_n^\alpha |u_n|^2$ one obtains, in an analogous way:

$$1 + b\lambda^\alpha + c\lambda^{2\alpha} = 0 \ . \tag{4.70}$$

Defining $z = \lambda^\alpha$ [101], we can solve the quadratic equation $1 + bz + cz^2 = 1 + bz - (1+b)z^2 = 0$, where we used (4.69), and obtain the two solutions:

$$\begin{cases} z_1 = 1 \\ z_2 = -(1+b)^{-1} \end{cases} \implies \begin{cases} \alpha_1 = 0 \\ \alpha_2 = -\log_\lambda(-b-1) \end{cases} \tag{4.71}$$

The first solution corresponds to the energy: this was expected because we already used the relation derived from energy conservation to eliminate c from the quadratic equation. The second solution, the same written without proof in (4.64) with the change of notation $b = -\beta$, denotes the second quadratic invariant, which can be enstrophy-like or helicity-like depending on the value of b, as found varying β in the GOY model.

It is easy to construct an energy balance equation. Defining the kinetic energy of shell n as:

$$e_n = u_n u_n^*/2 \tag{4.72}$$

we can compute its time derivative and get the energy budget for that shell:

$$\dot{e}_n = -t_n + d_n + i_n \ . \tag{4.73}$$

The transfer t_n, dissipation d_n and injection i_n terms read, respectively:

$$t_n = \Delta_{n+1} + b\Delta_n - (1+b)\Delta_{n-1} \ , \tag{4.74}$$

$$d_n = -\nu k_n^2 u_n u_n^* \ , \tag{4.75}$$

$$i_n = \mathrm{Re}\{f_n u_n^*\} \ . \tag{4.76}$$

In (4.74), Δ_n couples consecutive shell variables in the following way:

$$\Delta_n = k_n \mathrm{Im}\{u_{n-1}^* u_n^* u_{n+1}\} \ . \tag{4.77}$$

Its average actually plays an important role in the statistical theory of the model. Specifically, in [9] the authors define the third-order structure function for the Sabra model as:

$$S_3(n) = \langle \Delta_n \rangle / k_n \ . \tag{4.78}$$

This implies that, provided Kolmogorov's 4/5 law is valid, the quantity Δ_n is shell-independent in the inertial range.

It is evident that the difference between the Sabra and GOY equations, respectively (4.68) and (4.62), resides only in the choice of complex conjugation for the shell velocities in the three advection terms. This is because the relation between phases of consecutive shell velocities generated in the GOY model the spurious periodic correlations discussed before: the modified version of the coupling in the Sabra model leads to new phase relations and to the disappearence of unphysical long-range correlations [9]. More explicitly, if we take the phase transformation $u_n \to u_n e^{i\theta_n}$,

the GOY equations will be invariant under the transformation if $\theta_{n-1}+\theta_n+\theta_{n+1}=0$, while for the Sabra model the relation reads $\theta_{n-1}+\theta_n-\theta_{n+1}=0$. Both equations can be solved recursively once θ_1 and θ_2 are given, but the former displays a period-three solution, e.g. $\theta_n=\theta_{n-3}$, which in turn generates oscillations of the same period in the structure functions. The phase relation for the Sabra model does not present this annoyance, so the only nonzero correlation functions are the short-range ones.

Let us finally notice that all shell models also allow to study a reduced, simplified version of the truncated Euler equation, which we discussed in Section 4.2, by simply imposing $\nu=f_n=0$. That makes the system conservative, since in the energy balance equation (4.73) the only surviving term on the r.h.s. is the transfer term t_n, which neither creates nor dissipates kinetic energy. This will allow us to make comparisons between nonequilibrium indicators in the "regular" Sabra model and in the inviscid one, which are out-of-equilibrium and equilibrium systems, respectively.

Before concluding, it is worthwhile to state explicitly the chief advantages of employing shell models in dynamical and statistical studies of turbulence, and to show some visual proofs in support of the claims. As already mentioned, comparing the (truncated) NS equation with the shell model equations one easily realizes the enormous dimensional reduction enjoyed by the latter. For DNS halving the smallest measured spatial scale (grid spacing) means refining the grid by increasing the number of points by a factor 2^D, with D the spatial dimensionality of the system. On the other hand in shell models simply adding one variable u_{N+1} - i.e. two degrees of freedom - allows to measure velocity fluctuations at scale $l_{N+1}\sim l_N/\lambda$, where λ is the increment factor of the shell radii. This has the important consequence that the scale separation between the large forcing scales and the smallest dissipative ones can be increased without much effort, thereby attaining very high Reynolds numbers. For instance, the approach to fully-developed turbulence can be studied in shell models by increasing the extent of the inertial range adding further shells (but suitably tuning the viscosity for obtaining stable stationary states). Conversely this type of numerical study is unfeasible in DNS, even for the most powerful supercomputers. Remarkably, the most peculiar features of turbulence such as intermittency, dissipative anomaly, Kolmogorov's 4/5 law and direct/inverse cascades, are observed also in the hyper-simplified framework of the Sabra shell model. Even though it could be argued that some of these properties are strongly dependent on the spatial structure of the fluid, the multiscale nature of turbulent fluids makes sure, to some extent, that a set of coupled ODEs resembling the evolution of shell-averaged Fourier modes is effective enough in capturing the spectral properties of real turbulence. Of course interesting spatial features, e.g. vortices, coherent structures, plumes, are lost in the shell model description, where the spatial relationships are absent by construction: this is the reason why they are also called zero-dimensional models.

Figure 4.5 shows two instances of the "unreasonable effectiveness" of the Sabra shell model: in panel (a) the structure functions defined in (4.66), and in panel (b) the average energy flux out of shell M, which reads:

$$\langle \Pi_M \rangle = \sum_{n=1}^{M} \langle t_n \rangle = \langle \Delta_{M+1} \rangle + (1+b)\langle \Delta_M \rangle \ . \tag{4.79}$$

The structure functions reveal a very extended inertial range, covering the majority of the employed shells. A smooth power law behaviour is observed, followed by

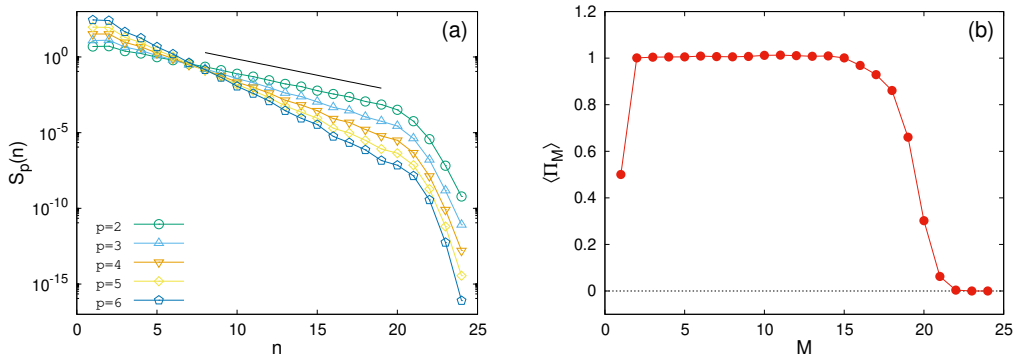

Figure 4.5. (a) Structure functions (4.66) from order $p = 2$ to $p = 6$. The inertial-range power laws in terms of k_n become linear trends when plotted against n in logarithmic y axis. The black line reproduces the scaling of $S_2(n)$ with the anomalous exponent $\zeta_2 = 0.71$ estimated in experiments and simulations. (b) Average energy flux out of shell M. The flux is positive and constant in the inertial range, equal to $\epsilon = 1$.

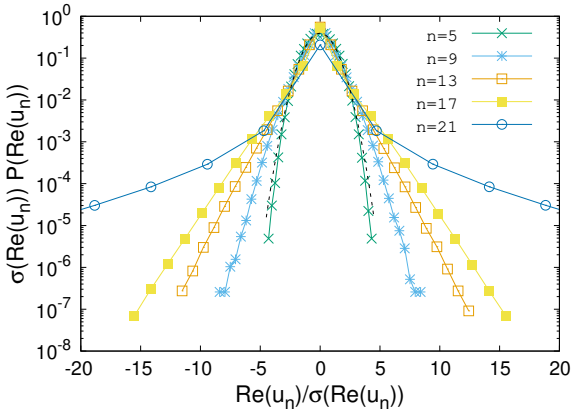

Figure 4.6. Rescaled p.d.f.'s of $\mathrm{Re}(u_n)$, with n ranging from the inertial to the dissipative range. Notice the tails becoming fatter as n increases. The black dashed line is a rescaled Gaussian with the same variance as shell $n = 5$.

the damping of the last shells by viscous effects. The anomalous scaling displays a very good agreement with experimental and numerical data: the black solid line represents the power law $k_n^{-\zeta_2} \simeq \lambda^{-n\zeta_2}$ plugging in the exponent measured in the numerical study [102], which is, surprisingly, also compatible with experimental estimates. The average energy flux is positive as expected from the direct energy cascade, and in the inertial range it is equal to the rate of energy injection (and dissipation) ϵ. In these simulation a forcing with constant input power equal to 1 was used on the first two shells, namely: $i_1 + i_2 = \varepsilon = 1$, where i_n is defined in Eq. (4.76). For details see Appendix C. Apart from the breaking of self-similar scaling, intermittency also emerges from the probability density functions of the degrees of freedom, which in our case are the real and imaginary parts of each shell velocity. In Figure 4.6 one clearly notices that, as the shell number increases, the tails of the p.d.f.'s become larger and larger because higher shells experience more the

effect of impulsive local bursts of energy dissipation. From the Gaussian shape shown by lower shells (larger length scales) there is a transition towards exponential-tailed distributions at higher n's, until reaching a stretched-exponential form $\sim \exp(-x^\alpha)$ with $0 < \alpha < 1$ for the largest shell displayed. The results in the figures come from simulations on the Sabra model with $N = 24$ shells and forcing on $n = 1, 2$. More details on the numerics, which are the same employed in most of the following studies, are reported in Appendix C.

4.5 Nonequilibrium indicators in the viscous and inviscid Sabra model

In this Section we present our results about the nonequilibrium nature of the viscous Sabra shell model, results which become more meaningful when compared with those of the analogous inviscid model, a system in statistical equilibrium. We shall first discuss in 4.5.1 the test of irreversibility by exploiting the non-symmetric time correlation functions introduced in Section 2.3.2. They will be tested for the viscous shell model forced at large scales (run-LSF) and for the inviscid shell model without forcing (run-Eq). This topic leads naturally to investigating the instantaneous rates of change of the shell energies, whose statistics is dealt with in a subsequent dedicated Paragraph. We then present in 4.5.2 the study on non-diagonal energy Response Functions (RFs) which are able to highlight in run-LSF the asymmetry between shell interactions and the consequent presence of an energy cascade, whereas in run-Eq they reveal energy equipartition as expected for a conservative system. Finally we introduce in 4.5.3 a Sabra model forced at intermediate scales (run-ISF), showing that the physics at scales larger than the forcing scale is akin to the inviscid model (equilibrium) while at scales smaller than the forcing we observe the usual non-equilibrium energy cascade.

4.5.1 Time irreversibility

As discussed in Sec. 2.3.2 in order to test the irreversibility of the turbulent energy cascade we focus on the energy signal $e_n(t) = |u_n|^2/2$ at shell n, and varying n in the cascade-dominated inertial range. In particular, we measure the ATCF Ψ (2.62) or, equivalently, Φ (2.63), which we rewrite here in nondimensional form as:

$$\Psi_{e_n}(\tau) = \frac{\langle e_n^2(t) e_n(t+\tau)\rangle - \langle e_n(t) e_n^2(t+\tau)\rangle}{\langle e_n^3(t)\rangle} \equiv$$

$$\equiv \Phi_{e_n}(\tau) = \frac{1}{3}\frac{\langle [e_n(t+\tau) - e_n(t)]^3\rangle}{\langle e_n^3(t)\rangle}\,. \tag{4.80}$$

Even though the two quantities are divided by non-dimensionalizing factors (here the average cubed energy of shell n) which in Eqs. (2.62) and (2.63) are absent, we decided not to change notation to simplify the comprehension. Again, let us remember that $\langle\cdot\rangle$ indicates time average over a stationary state. We also recall that the two different expressions should be formally equivalent for a stationary signal, but can be numerically different for finite statistics (see Appendix D).

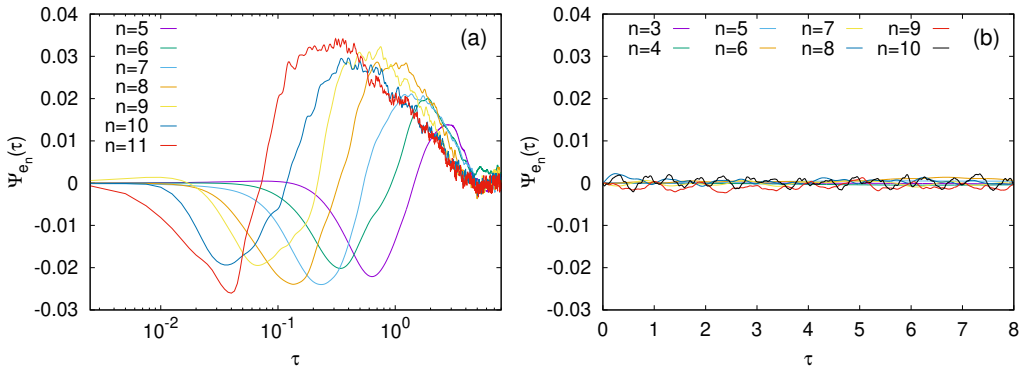

Figure 4.7. Asymmetric time-correlation functions $\Psi_{e_n}(t)$ at varying n as labeled. (a) Turbulent case, shells n in the inertial range. Different functions show a qualitatively similar behavior, and symmetry under time reversal is absent. Statistics: $6 \cdot 10^5$ samples. (b) Inviscid case, shells n as labeled in the range with energy equipartition. Small fluctuations around zero are compatible with $\Psi_{e_n}(t) = 0$. Statistics: $5 \cdot 10^5$ samples.

The inviscid unforced shell model reaches an equilibrium statistically stationary state characterized by detailed balance and zero net currents. In other words, forward and backward dynamics are indistinguishable. As a consequence we should expect that $\Psi_{e_n}(\tau) \equiv \Phi_{e_n}(\tau) = 0$. Conversely for the viscous forced shell model, owing to the presence of an energy flux from large to small scales (i.e. from small to large shells), the dynamics is irreversible and $\Psi_{e_n}(\tau) \equiv \Phi_{e_n}(\tau) \neq 0$. Such expectations are well verified as shown in Figure 4.7: apart from unavoidable fluctuations, $\Psi_{e_n}(\tau) = 0$ for the inviscid model (run-Eq, Figure 4.7(b)), while for the forced model is clearly different from zero (run-LSF, Figure 4.7(a)) for all measured shells and, actually, the nonequilibrium case displays several interesting features that we discuss in the following.

First of all, for small time lags $\Psi_{e_n}(\tau)$ is negative, but it becomes positive at larger τ and finally it approaches zero in an asymptotic fashion (not clearly visible in logarithmic time axis used in Figure 4.7(a)). This is consistent with the idea that energy decreases on a fast time scale and increases over a longer time scale (notice that by stationarity $\langle e_n(t+\tau)\rangle = \langle e(t)\rangle$). This is similar to the flight-crash events described in [75], but in that work they were studied in terms of the kinetic energy of a Lagrangian tracer particle, while here they are intended at the level of a single shell. The phenomenon by which the energy loss is faster than the energy gain is physically understood from the fact that the time scale of the shell decreases with the scale as $\tau_n \sim (u_n k_n)^{-1} \sim k_n^{-2/3}$, where in the last approximation we used Kolmogorov scaling. Therefore, it takes longer to receive energy from larger and slower scales (smaller n) than to transfer it to smaller scales (larger n).

The temporal behavior of $\Psi_{e_n}(\tau)$ is the result of several time-scales simultaneously at play, as already clear from Figure 4.7(a). Indeed one can see that the short time minima depends on the shell index n while the large-time decay is essentially independent of n, as the curves reach zero at about the same time. The presence of many time scales is even clearer by looking at Figure 4.8, showing that different rescaling of the time lags depending on the scale as k_n^β are needed to make either

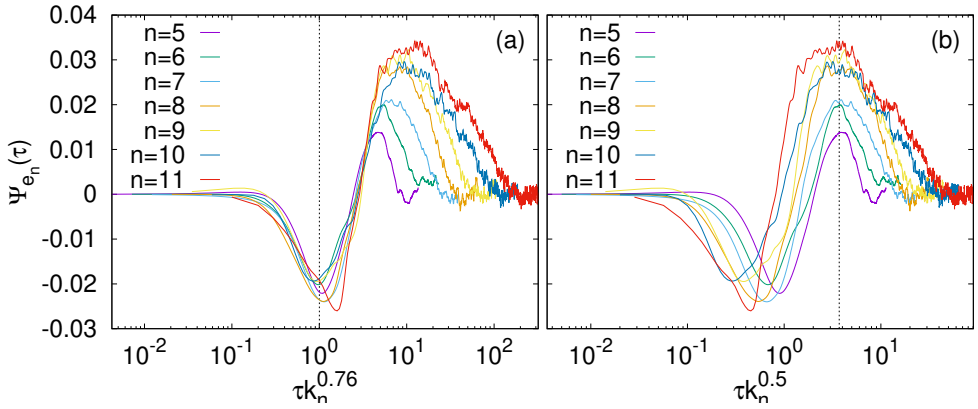

Figure 4.8. Same as Figure 4.7(a) with time rescaled by (a) $\tau_n = k_n^{-0.76}$ (see text for a discussion) and (b) $k_n^{-0.5}$, where 0.5 was chosen in such a way to line up the maxima. The vertical dashed lines are drawn to guide the eyes making clearer the line up.

the minima ($\beta \approx 0.76$, Figure 4.8(a)) or the maxima ($\beta \approx 0.5$, Figure 4.8(b)) line up. While we have no clear understanding of the latter exponent, the first one can be understood as follows.

As discussed in the following Paragraph and in Appendix D, at short times the following should hold:

$$\Psi_{e_n}(\tau) \equiv \Phi_{e_n}(\tau) \approx \frac{\langle \dot{e_n}^3 \rangle}{\langle e_n^3 \rangle} \tau^3 \,. \tag{4.81}$$

Equations (4.67) and (4.84) (see next Section) imply that $\langle \dot{e_n}^3 \rangle / \langle e_n^3 \rangle \sim k_n^{3-\zeta(9)+\zeta(6)}$. From our simulations we get $\zeta(6) \approx 1.70(2)$ and $\zeta(9) \approx 2.43(6)$. If we now re-scale τ in Eq. (4.81) with $\tau_n \sim k_n^{-\beta}$ by requiring that the expression does not depend on n we have $\beta = (3 - \zeta(9) + \zeta(6))/3 \approx 0.76(3)$, which is in good agreement with the numerical exponent that rescales the minima in Figure 4.8(a). We also notice that Ψ_{e_n} is the difference of two disconnected, single scale and multi-time correlation functions that, as thoroughly discussed in Ref. [103], should involve a whole hierarchy of fluctuating eddy-turnover times from the shortest up to the largest. In [103] the general framework of multi-time and multiscale correlation functions was discussed, into which the functions Ψ_{e_n} find their place: one can define suitable correlations involving energy at different shells and different times, which besides providing information on the irreversibility can also further characterize the physics of the energy cascade. However, this goes beyond the aim of this thesis and can be investigated possible future studies.

Power fluctuations

The negativity of $\Psi_{e_n}(\tau)$ for small τ can be further scrutinized by studying directly the $\tau \to 0$ limit. Indeed by expanding (4.80) for small τ (see Appendix D, where a discussion on the subtle numerical aspects related to the short time behavior of Ψ and Φ is also present) it is easy to realize that the initial-time behaviour means that $\langle \dot{e}_n^3 \rangle < 0$, while we know by stationarity that $\langle \dot{e}_n \rangle = 0$: this means that the statistics of $\dot{e}_n$ is negatively skewed, which confirms the fact that it is more probable

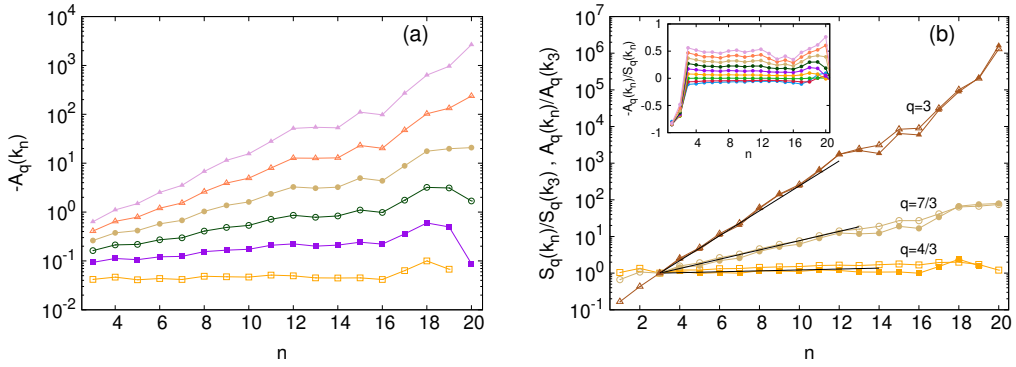

Figure 4.9. (a) Asymmetric moments $-\mathcal{A}_q(k_n)$ defined in (4.83) at varying the shell number $n = \log_2(k_n/k_0)$, for increasing $q = s/3$ with $s = 4, \ldots, 9$ (from bottom to top). The moments for $q < 1$ are positive (not shown) and $\mathcal{A}_1(k_n) = 0$ by stationarity. The lowest and highest shells are omitted. (b) Symmetric moments $\mathcal{S}_q(k_n)$ (empty symbols) and asymmetric ones $-\mathcal{A}_q(k_n)$ (filled symbols) rescaled by their value at $n = 3$ for three values of q, as labeled. The black solid lines display the prediction (4.84). Inset: the ratio $-\mathcal{A}_q(k_n)/\mathcal{S}_q(k_n)$, with $q = s/3$ for $s = 1, \ldots, 9$ from bottom to top. Statistics is computed on $2.5 \cdot 10^6$ samples.

to lose than to gain energy on short time intervals. This observation was originally made in [75] in the context of irreversibility of Lagrangian trajectories in turbulence, and further analyzed in [104] in both direct numerical simulations and in a shell model version of Lagrangian motion. In particular, in [104] a set of symmetric and asymmetric moments was introduced to probe the asymmetry of the distribution.

Here, following the mentioned work, we consider the moments:

$$\mathcal{S}_q(k_n) = \langle |\dot{e}_n|^q \rangle / \epsilon^q \tag{4.82}$$

$$\mathcal{A}_q(k_n) = \langle \dot{e}_n |\dot{e}_n|^{q-1} \rangle / \epsilon^q \tag{4.83}$$

where the normalization by ϵ^q is only to make the quantities nondimensional. These moments allow to probe the scaling behavior of both symmetric and asymmetric components of the power statistics. Numerical simulations show that $\mathcal{A}_q(k_n) > 0$ for $q < 1$ and < 0 for $q > 1$, whereas for $q = 1$ is zero by stationarity. Moreover, as shown in Figure 4.9(a), the asymmetric moments display a power law behavior, $-\mathcal{A}_q(n) \sim k_n^{\alpha(q)}$. To rationalize the exponents $\alpha(q)$ we can use dimensional analysis in the spirit of the multifractal model [6]. Noticing that $\dot{e}_n$ is energy divided by time, we can assume that for each shell one has to use its own characteristic eddy turnover time, that dimensionally can be estimated as $\tau_n \sim 1/(|u_n|k_n)$, so that

$$\langle \dot{e}_n^q \rangle \sim \langle |u_n|^{2q} k_n^q |u_n|^q \rangle \sim k_n^q S_{3q}(n) \sim k_n^{q-\zeta(3q)} , \tag{4.84}$$

where we used (4.66) and (4.67) in the last two steps. It should be noted that this argument is purely dimensional, thus it applies both to the symmetric and asymmetric moments. It is worth stressing that it is not obvious a priori that $\mathcal{S}_q(k_n)$ and $-\mathcal{A}_q(k_n)$ should scale in the same way, and neither that the asymmetric moment could be guessed with a dimensional argument. Indeed it depends on cancellations that, in principle, are very difficult to control or to guess. However, Figure 4.9(b)

shows that $\mathcal{S}_q(n)$ and $-\mathcal{A}_q(n)$ possess the same scaling behavior, and that it agrees perfectly with the dimensional prediction (4.84). In the inset the ratios between asymmetric and symmetric moments of different orders are plotted, showing that in the inertial range they are shell-independent quantities.

4.5.2 Energy response functions

In this Section we continue the investigation of nonequilibrium features in the Sabra model by means of time-dependent indicators, again comparing the results with those of its inviscid unforced counterpart. While the chosen asymmetric correlation functions studied in the previous Section were essentially local (in shells) quantities - even though we stress once more that their overall behaviour was due to a large hierarchy of timescales, e.g. shells - here we would like to gain additional information about the dynamical relationship between nearby shells. It is known that the spectral-space triad interactions are the source of the nontrivial transport properties generating, for instance, the energy cascade. Such cascade can be viewed as a symmetry breaking of the upscale vs. downscale coupling terms, favoring energy transfer towards large shells.

In order to detect this scale asymmetry between shells, we shall study non-diagonal RFs on the shell energies $e_n(t)$ of the type introduced in (2.73):

$$R_{m,n}(t) = \frac{\overline{\delta e_n}(t)}{\delta e_m(0)} \ , \tag{4.85}$$

where the first index refers to the perturbed shell and the second to the shell whose energy variation one measures. To fix the initial energy perturbation $\delta e_m(0)$ of each experiment we use the following rule for the shell velocity at $t = 0$:

$$u_m = \sqrt{2e_m}e^{i\theta_m} \quad \longrightarrow \quad u'_m = \sqrt{2(e_m + \delta_m)}e^{i\theta_m} \tag{4.86}$$

where θ_m is the phase of u_m, and $\sqrt{2e_m}$ its modulus. The constant δ_m quantifies the magnitude of the initial energy perturbation while keeping the phase of u_m fixed, and is such that: $\delta e_m(0) = \delta_m$. The phases are indeed crucial for the energy transfer [105]: for this reason we opted for not introducing any deviation in them. Moreover, we consider a non-infinitesimal perturbation similarly to [76]: specifically, we choose δ_m to be a finite fraction of the typical fluctuation of the shell energy, namely its standard deviation:

$$\delta_m = f\sigma_{e_n} = \frac{f}{2}\sqrt{\langle |u_n|^4 \rangle - \langle |u_n|^2 \rangle^2} \ , \tag{4.87}$$

in which $f \simeq 0.2$ was used.

In Figure 4.10 we compare the RFs $R_{m,n}$ with $n - m = \pm 1$ measured in the viscous model (run-LSF, panel a) and in the inviscid model (run-Eq, panel b). The functions in Figure 4.10(a) clearly display the asymmetry between degrees of freedom mentioned before: in the turbulent system the opposite sign of the "forward" (towards smaller scales) and "backward" (towards larger scales) RFs reveals the presence of an overall energy current, displacing energy on average from larger to smaller scales. The different amplitudes and relaxation times relate to the fact that

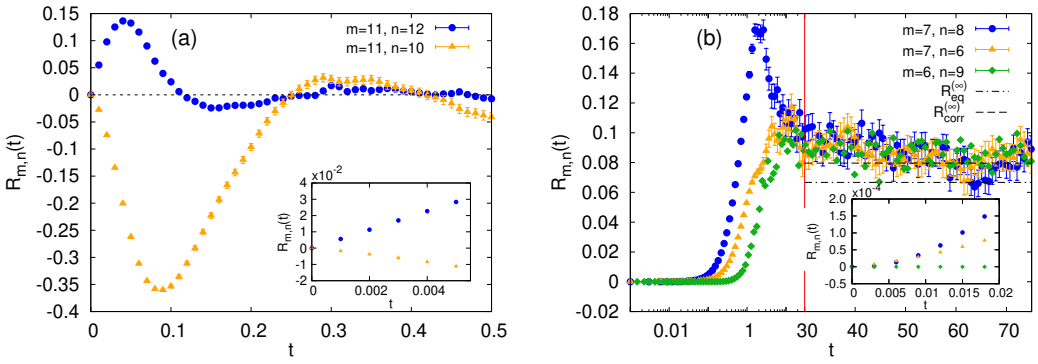

Figure 4.10. Non-diagonal energy RFs defined in (4.85), with error bars, measured at the neighboring shells of the perturbed one. (a) Turbulent Sabra model. Initial energy perturbation: $\delta_{m=11} \simeq 9.93 \cdot 10^{-3}$. (b) Inviscid Sabra model. The initial transient is plotted with logarithmic time axis up to the red vertical line, the later stages with a linear axis. Another RF has been added (green plot), with more distance between m and n, in order to show the common asymptotic value. The dot-dashed line shows $R_{eq}^{(\infty)}$ which is the value that would be reached if perfect energy equipartition occurs, the dashed line shows $R_{corr}^{(\infty)}$ which is the asymptotic value taking into account the boundary corrections (see Appendix E and main text). Initial perturbation $\delta_{m=6} = \delta_{m=7} \simeq 1.79 \cdot 10^{-3}$. The insets of both figures are enlargements of the initial-time range, showing respectively a non-zero and a zero first derivative at $t = 0$. In all figures statistics is computed on $5 \cdot 10^5$ realizations.

larger scales have larger amplitudes and are slower than the smaller scales. On the other hand, such an asymmetry is clearly lost in the inviscid system, as shown in Figure 4.10(b): the RFs are all positive, and after an initial transient they approach a common non-zero asymptotic value. This trend can be explained as follows. In the inviscid system the total energy $\sum_n e_n$ (but also helicity) is conserved, therefore our perturbation, which always increases the energy of the perturbed shell, brings the system to a larger constant-energy hypersurface in phase space. Assuming a perfect energy equipartition one can compute the expected long-time value $R_{\mathrm{eq}}^{(\infty)} = 1/N$. However, as discussed in Appendix E, boundary effects prevent perfect equipartition. Taking them into account one can compute a corrected asymptotic value, $R_{\mathrm{corr}}^{(\infty)}$, which fits better with the data as shown in Figure 4.10(b).

It is equally interesting to notice that short shell-distance RFs show non-zero initial time derivatives in the turbulent case, whereas they are zero in the inviscid system (see the insets of Figure 4.10). Briefly, this is due to the presence or absence, respectively, of energy cascades in the system, since these derivatives are related to the order-three correlator describing the energy flux through the shells. A thorough treatment on this point is present in Appendix F.

In order to obtain a more complete investigation of the turbulent cascade we also studied, in run-LSF, the response of shells further-apart from the perturbed one. Owing to the fact that the energy spectrum decays as a power law, in the main panel of Figure 4.11(a) we show the relative energy deviation,

$$\frac{\delta_m}{\langle e_n \rangle} R_{m,n} = \frac{\overline{\delta e_n}(t)}{\langle e_n \rangle} \ , \tag{4.88}$$

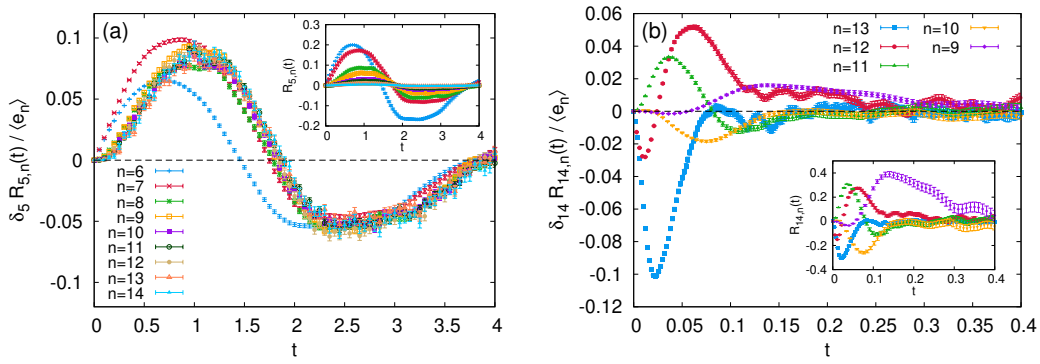

Figure 4.11. Relative energy deviation (4.88) at consecutive shells, with fixed perturbed shell m, in the turbulent shell model: (a) for shells $n > m = 5$, with $\delta_{m=5} \simeq 0.1$; (b) for shells $n < m = 14$ and $\delta_{m=14} \simeq 2.74 \cdot 10^{-3}$. The insets show the un-rescaled RFs. Statistics is computed on $5 \cdot 10^5$ iterations.

for $n > m$. The advantage of the relative deviation (4.88) is that it allows for normalizing the amplitude of the functions, making it possible to compare the responses of shells at different distances from the perturbed one. Figure 4.11(b) shows the same for shells smaller than the perturbed one. The insets represent the usual (non-normalized) RFs. The energy deviations in the forward direction nicely collapse onto the same curve, apart from the functions with $n - m = 1, 2$. These two are the only functions whose index n is in the same triad of consecutive shells as m, so a difference with the other functions can be expected. On the other hand, the energy deviations in the backward direction lack any kind of similarity between themselves, and their short-time value, before the relaxation, can be indeed positive (energy gain) or negative (energy loss) for different values of $n - m$. Unlike the forward functions, the backward ones show smaller amplitudes as the distance from the perturbed shell grows. Overall, a correct interpretation of the latter RFs requires a better understanding of how the different timescales involved, from the slowest to the one with shell index $\max\{m, n\}$, contribute to the energy deviation, in the same way as assumed for multi-time, multi-scale correlation functions [103].

4.5.3 Coexistence of equilibrium and nonequilibrium in the Sabra model with intermediate-scale forcing

So far we have discussed either the case of the inviscid, unforced shell model or the forced viscous one. We have shown how asymmetric energy correlations and energy RFs can reveal the breaking of time reversal and scale symmetry, both induced by the energy flux from the scales of forcing down to the smaller scales. Of course, at scales smaller than the forced ones the direct energy cascade is expected in 3D turbulence: this has been understood since the pioneering work of Richardson and Kolmogorov.

Less studied is the statistical behaviour of the modes whose length scales are instead *larger* than the forcing scales, modes which are figuratively situated upstream of the cascade source. Since such scales are not directly influenced neither by the forcing nor by the viscous damping, and considering the direction of the cascade,

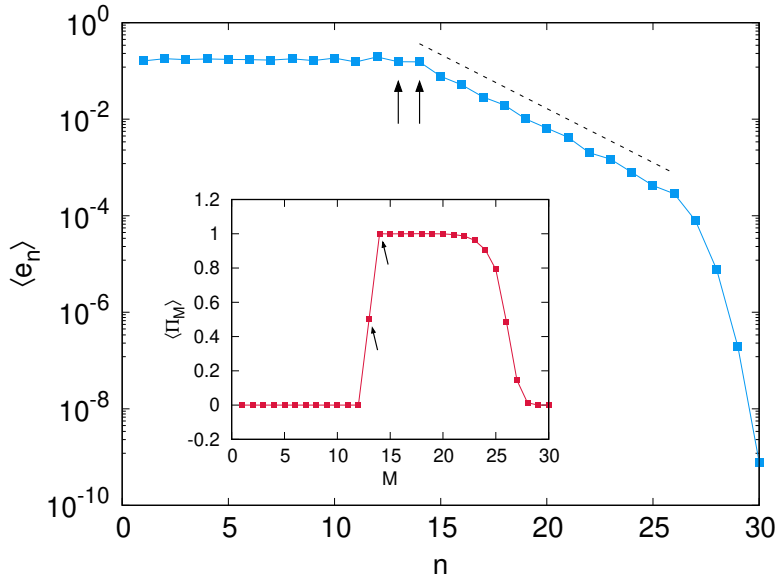

Figure 4.12. Energy spectrum $\langle e_n \rangle$ for the Sabra shell model with forcing at intermediate scales. The three regimes of energy equipartition, power-law scaling and viscous damping can be identified. The dashed line corresponds to the scaling $\langle e_n \rangle \sim k_n^{-\zeta(2)}$, with $\zeta(2) \approx 0.74(4)$ obtained from the large-scale forcing configuration. Inset: average flux $\langle \Pi_M \rangle$ out of shell M, as in (4.79). There is a clear transition from zero to positive outward flux. The small arrows in both figures indicate the forced shells. Statistics: 10^6 samples.

it has been conjectured that the physics of these large scales should be akin to the equilibrium one [6]. Numerical [106, 107, 108] and experimental [109] studies indeed seem to confirm that many aspects of the scales above the injection scale are well captured by absolute equilibrium theory [83]. Recent studies [110, 111], however, seem to point to the fact that deviations from equilibrium can be detected in direct numerical simulations. In particular in [111] the authors show that the third order velocity structure function is not zero (as a Gaussian-equilibrium statistics would have prescribed), but decays as the second power of the scale. This observation is substantiated by an inspection of the Kàrmàn-Howarth-Monin equation [6], which ultimately shows that such deviations can be ascribed to non-local interactions that, however, are absent by construction in the shell model. On the other hand, the k-dependence of the energy spectrum at large scales appears to be determined by the momentum injected by the forcing: for instance in [110] it is claimed that a solenoidal, localized-in-space forcing would yield a large-scale spectrum not compatible with absolute equilibrium.

All the above discussed works motivated us to investigate the behaviours of asymmetric correlations and energy response functions at scales smaller and larger of the forcing scale. In order to accomplish this, we now study the Sabra model with $N = 30$ shells forced at intermediate scales (i.e. shells n_f and $n_f + 1$, with $n_f = 13$) such that a big enough range of shells was provided both above and below the forced ones (see Appendix C for further technical details about run-ISF).

Figure 4.12 shows the energy spectrum $\langle e_n \rangle$ in the main panel, and the average

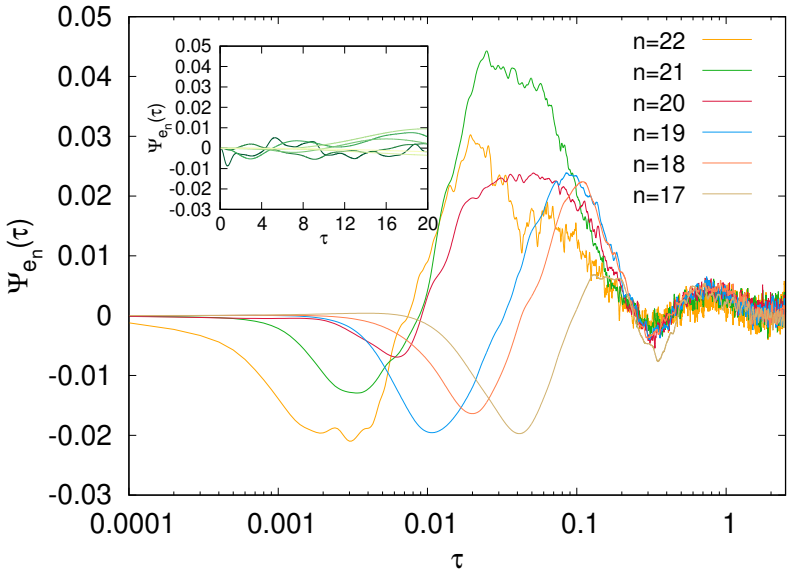

Figure 4.13. Asymmetric time correlation functions (4.80) measured at shells larger than the forced ones, as in label. Inset: same correlation functions, measured at shells below the forcing, with n ranging from 5 (lighter) to 11 (darker). Statistics: $5 \cdot 10^5$ samples.

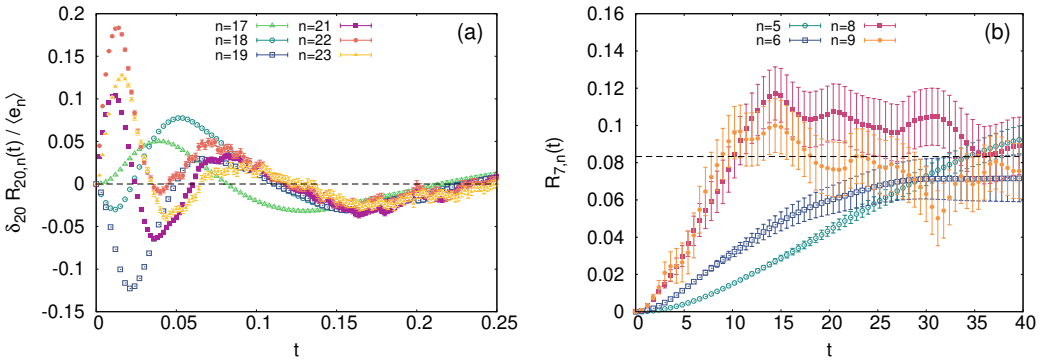

Figure 4.14. Energy response functions in the Sabra model with forcing at intermediate scales: (a) RFs normalized as in (4.88) when perturbing shell $m = 20$ in the inertial range. Both the forward ($n > m$) and the backward ($n < m$) functions are qualitatively similar to those of Figure 4.11a and b, respectively. (b) $R_{m,n}$ for $m = 7$ in the middle of the equiparted part of the spectrum, above the forced shell. The RFs approach a common asymptotic value as in Figure 4.10(b). The dashed line is estimated as $R_{eq}^{(\infty)} = 1/N^*$, where N^* is the number of shells for which energy equipartition holds. In both cases statistics is over $2 \cdot 10^5$ realizations.

energy flux $\langle \Pi_M \rangle$ in the inset: energy equipartition and zero energy flux obtained for shells smaller than the forced ones are good indicators of statistical equilibrium. At first we study the asymmetric correlation (4.80) to test the time asymmetry of the energy evolution at scales both below and above the forcing one. As shown in Figure 4.13, $\Psi_{e_n}(\tau)$ for $n > n_f$ (main panel) is akin to the results of Figure 4.7(a) obtained with the usual large scale forcing, while for $n < n_f$ (see inset) is statis-

tically compatible with zero, as expected in an equilibrium regime (compare with Figure 4.7(b)). Then we investigate the relaxation of an energy perturbation, either perturbing a shell $m > n_f$ (i.e. in the energy cascade range) or a shell $m < n_f$ (i.e. in the supposed equilibrium range). Figure 4.14(a) displays the normalized RFs, i.e. the relative energy deviations (4.88), when the perturbed shell is larger than the forced ones, and their behavior retain the features shown by both forward and backward normalized RFs. Conversely, Figure 4.14(b) refers to the case where the perturbation acts on a shell smaller than forced ones: as in the inviscid model, all RFs are positive and reach a common asymptote whose value is again found, in first approximation, by assuming energy equipartition among the degrees of freedom.

Summarizing, the behavior of both asymmetric correlation and energy response functions gives strong evidence that, in the Sabra shell model, the physics of the scales larger than the forcing one is compatible with the equilibrium as in the inviscid shell model. We remark, however, that there could be some properties which can deviate from equilibrium. The dynamics clearly does not preserve neither the total energy nor the total helicity, and it is unclear what will be the effect on, e.g., the spectrum at the scales which match the forcing scales. As discussed in Appendix E, in the inviscid case oscillations in the spectra are expected in correspondence of the largest shell: this behaviour will be clearly modified by the presence of the forcing. A confirmation of this difference is found in the good estimate of the asymptotic value computed with the perfect-equipartition assumption: boundary correction appears not necessary (see Figure 4.14(b)). In Ref. [111] it was pointed out that there are detectable deviations from Gaussianity at scales larger than the forcing scale for the Navier-Stokes equations. We studied a similar quantity, namely the Sabra model third-order structure function as defined in (4.78), and we found that it takes values compatible with zero for $n < n_f$ (not shown). This result is further confirmed by considering the analogous of the Kàrmàn-Howarth-Monin equation for the shell model. The difference between DNS and shell model is likely due to the fact that in the latter the quadratic interaction term is local, and not long-ranged.

4.6 Conclusion

The study of asymmetric time correlations and of energy response functions provided interesting information about the energy cascade (in the viscous case) or its absence (in the inviscid case). Asymmetric time correlation functions of the shell energies can clearly distinguish the case of a forced shell model displaying the direct energy cascade, in which the peculiar behaviour of the functions is linked to the irreversible energy transfers, from the case of an unforced and inviscid model where the correlations simply amount to zero. Energy response functions display great dissimilarities between the two cases as well: in the inviscid case the conservative nature of the model clearly emerges from the long-time behaviour of such functions. Moreover, a net difference is observed in the forced case when looking at shells larger (smaller scales) or smaller (larger scales) than the perturbed one, as a consequence of the average energy current from large to small scales. The quantities studied in this Chapter thus allow to observe - somehow from another novel perspective - the celebrated Richardson cascade scenario from the point of view of nonequilibrium

statistical mechanics. Finally, we also considered the case of a Sabra model forced at intermediate scales, in order to be able to scrutinize the behavior of both quantities at scales larger or smaller than the forcing scale. The emerging picture seems to confirm the belief that scales larger than the forcing display properties which can be ascribed to the equilibrium physics of the unforced-inviscid Sabra model.

There are open research directions stemming from this study. A natural one would be to adapt our tools to the case of three-dimensional Navier-Stokes turbulence, to be studied numerically with DNS, and in particular to explore their behavior at scales larger than the forcing scale where some features seem to be ascribable to equilibrium [106, 108, 109] while others show deviations from equilibrium [111]. It could be not surprising, but surely very interesting, to discover that some properties are well captured by the equilibrium physics while others are not. It must be remarked, however, that in NS turbulence there is the risk that interesting properties shown by asymmetric correlations would be masked by sweeping effects, which are unavoidable in the Eulerian framework. Another possible direction is to exploit the possibility offered by the Sabra shell model to change the second inviscid invariant by simply changing the parameter b, in order to repeat the same study in a 2D-like shell model [112, 101], where an inverse energy cascade (i.e. towards large scales) accompanied by a direct cascade of enstrophy should take place. In two-dimensional hydrodynamics nonlocal interactions have a significant weight on transfer mechanisms, rendering 2D shell models less reliable than their 3D versions. Still, a rich variety of regimes was conjectured to exist for 2D-like models [113]: it is then interesting to observe what the tools we introduced can tell us about this topic.

Chapter 5

Conclusion

This Thesis focused on the characterization of time-irreversibility and transfer processes in nonlinear simplified models of geophysical and turbulent flows: the two-scales Lorenz96 model and the Sabra shell model. Only a minimal resemblance to the original, full equations is retained, yet nontrivial dynamical and statistical phenomena are observed, such as the propagation of Rossby-like waves in the former and the direct energy cascade in the latter model. Let us remark here the apparent similarity between the evolution equations of the two systems: the degrees of freedom are a finite set of interacting variables, real in the former and complex in the latter; a forcing term provides "energy" to some variables, while linear viscous damping drains energy from the system; advective-like couplings, preserving phase-space volumes and energy, redistribute excitations in order to reproduce known transport properties. Broadly speaking, both models represent driven-dissipative processes. Conversely, there are major differences that must be borne in mind. The Lorenz96 model aims at reproducing a one-dimensional spatial structure, namely the indices of the variables indicate a discretization of the positional coordinate along a mid-latitude circle, whereas the Sabra model mimicks nonlinear spectral interactions in Fourier space, thus the indices of the variables indicate the wavenumbers (or inverse lengths) at which velocity fluctuations are estimated. Then, the Lorenz96 model is constructed with two timescales (also corresponding to two typical fluctuation amplitudes), while the Sabra model is a (spatially and temporally) multiscale system, since each Fourier-space shell has its own timescale and typical amplitude.

The tools chosen for performing our investigation on the nonequilibrium nature of both systems yielded original results. The asymmetric third-order time correlations showed visible differences when computed in the inviscid or viscous cases: in the former these functions show almost no activity, as expected from systems that are time-reversible and in equilibrium, while in the latter they display a nontrivial dependence on time, especially for short time-separations, as they should for nonequilibrium systems. The consistent behaviour found in the inertial range of the viscous Sabra model has been successfully linked to the asymmetries shown by the energy transfers among shells, transfers that are favored along the cascade direction. Non-diagonal response functions have demonstrated their effectiveness in detecting transfer asymmetries but also in discriminating between a conservative and a dissipative dynamics, therefore giving also access to phase-space properties. A

coherent behaviour was observed, in both models, for local-energy response functions when measured along the direction of transport (propagation of travelling waves in Lorenz96, energy cascade in Sabra), accompanied by incoherence in the opposite direction. We can conjecture the latter phenomenon to be caused by a sort of interference caused by fluctuations arriving at a given site after having travelled different paths, but this is still an open question.

In the Sabra model we also investigated the statistical behaviour of length scales above the forcing scale: the properties found in that range are indistinguishable from those of systems in equilibrium, while below the forcing the expected cascade develops. Thus, a coexistence of equilibrium and nonequilibrium properties was observed when the model is forced at intermediate scales. Additionally, the study on response functions in the Lorenz96 model led us to some final considerations about the predictability of multiscale systems. Comparing the responses of the total energy to a perturbation acting either on a slow or on a fast variable, it appeared evident how the simple observation of a relaxation process is not able to provide any information on the perturbing agent which caused the disturbance. A concrete example from geophysics is the following: let us consider a situation in which one is interested in predicting how a fluctuation of the air temperature, measured 2 meters above Earth's surface on a tropical region, evolves over time. If this fluctuation was caused by an increase in sea surface temperature - as during the El Niño–Southern Oscillation (ENSO) phenomenon - then the time evolution of the fluctuation follows the evolution of this driving. If instead it was caused by an increase in the solar incident radiation, then its time scale would be linked to that of the radiative processes.

This work left several open questions: the study of time correlations and response functions in 2D-like shell models is certainly of paramount interest, but it seems to be hindered by the unclear effectiveness of the existing models. Contradicting results are found in the literature, and the possibility that the original Sabra model, with a single set of variables, may reproduce a double cascade is quite dubious. The coexistence of equilibrium and nonequilibrium in real viscous flows is a subtle matter, since long-range spectral interactions could influence the behaviour of some observables but not of others. The tools showed here may help in understanding the behaviour of scales larger than the forced ones, even though the problem of large-scale sweeping on small eddies has to be somehow circumvented. Furthermore, while response functions are not easy to measure in more complex and realistic systems, asymmetric time correlations are easily computed from time series: thus another direction might be to analyze experimental records of suitable geophysical quantities to infer the absence of time reversibility.

Appendix A

Derivation of EPR and FDR for a discrete-time linear Gaussian process

In this Appendix we compute the Entropy Production Rate (EPR) and the Fluctuation-Dissipation Relation (FDR) for a linear Gaussian map, providing the full derivation to Eqs. (2.49) and (2.82). These derivations can be found in [114] and [12], respectively. Let us consider the most general case, namely a n-dimensional stochastic process at discrete times

$$\boldsymbol{x}_{t+\Delta t} = A\boldsymbol{x}_t + B\boldsymbol{\eta}_t\,, \tag{A.1}$$

where $\boldsymbol{x_t} = (x_t^{(1)}, \dots, x_t^{(n)})$, $\boldsymbol{\eta}_t$ is a n-dimensional vector of independent Gaussian variables with zero mean and unitary variance, A is a $n \times n$ matrix whose largest eigenvalue (in modulo) is < 1, and B is diagonal.

Entropy Production Rate

We denote by $P_s(\boldsymbol{x})$ the probability of $\boldsymbol{x}$ in the stationary state, and by $P(\boldsymbol{x}|\boldsymbol{y})$ the probability for the system to be found in $\boldsymbol{x}$, given that it was in $\boldsymbol{y}$ at the latest time. First, one has to compute the probability of the direct path $\boldsymbol{x}_t \to \boldsymbol{x}_{t+\Delta t}$

$$\begin{aligned} P(\{\boldsymbol{x}_s\}_t^{t+\Delta t}) &= P_s(\boldsymbol{x}_t)P(\boldsymbol{x}_{t+\Delta t}|\boldsymbol{x}_t) \\ &= \frac{P_s(\boldsymbol{x}_t)}{(2\pi)^{n/2}|B|}\exp\left[-\frac{1}{2}\left|B^{-1}\left(\boldsymbol{x}_{t+\Delta t} - A\boldsymbol{x}_t\right)\right|^2\right]\,, \end{aligned}$$

and that of the inverse trajectory $\boldsymbol{x}_{t+\Delta t} \to \boldsymbol{x}_t$

$$\begin{aligned} P(\{\boldsymbol{x}_s\}_{t+\Delta t}^{t}) &= P_s(\boldsymbol{x}_{t+\Delta t})P(\boldsymbol{x}_t|\boldsymbol{x}_{t+\Delta t}) \\ &= \frac{P_s(\boldsymbol{x}_t)}{(2\pi)^{n/2}|B|}\exp\left[-\frac{1}{2}\left|B^{-1}\left(\boldsymbol{x}_t - A\boldsymbol{x}_{t+\Delta t}\right)\right|^2\right]\,. \end{aligned}$$

Since the system is Markovian, we only need to consider one time-step. The entropy production rate is then defined as:

$$\sigma = \frac{1}{\Delta t}\left\langle \log\frac{P(\{\boldsymbol{x}_s\}_t^{t+\Delta t})}{P(\{\boldsymbol{x}_s\}_{t+\Delta t}^{t})}\right\rangle\,, \tag{A.2}$$

where the average is taken on $P(\{\boldsymbol{x}_s\}_t^{t+\Delta t})$. Since we are in the stationary state, the marginal probabilities verify

$$P(\boldsymbol{x}_t) = \int d\boldsymbol{x}_{t+\Delta t} P(\{\boldsymbol{x}_s\}_t^{t+\Delta t}) = P_s(\boldsymbol{x}_t)$$

and

$$P(\boldsymbol{x}_{t+\Delta t}) = \int d\boldsymbol{x}_t P(\{\boldsymbol{x}_s\}_{t+\Delta t}^{t}) = P_s(\boldsymbol{x}_{t+\Delta t})\,.$$

This fact allows for several simplification in the computation of (A.2). In particular, we easily get

$$\begin{aligned}\sigma &= \frac{1}{\Delta t}\left\langle \boldsymbol{x}_{t+\Delta t}^T B^{-2} A \boldsymbol{x}_t - \boldsymbol{x}_t^T B^{-2} A \boldsymbol{x}_{t+\Delta t}\right\rangle \\ &= \frac{1}{\Delta t}\left\langle \boldsymbol{x}_t^T (A^T B^{-2} - B^{-2} A)\boldsymbol{x}_{t+\Delta t}\right\rangle\,.\end{aligned}$$

In the second passage we used the trivial property that a 1×1 matrix is symmetric. By recalling (A.1), we get the final result

$$\begin{aligned}\dot{\Sigma} &= \frac{1}{\Delta t}\left\langle \boldsymbol{x}_t^T (A^T B^{-2} - B^{-2} A) A \boldsymbol{x}_t\right\rangle \\ &= \frac{1}{\Delta t}\mathrm{Tr}\left[(A^T B^{-2} - B^{-2} A) A C_0\right]\end{aligned} \tag{A.3}$$

where by Tr we denote the trace, and

$$C_0 = \langle \boldsymbol{x}_t \boldsymbol{x}_t^T\rangle\,. \tag{A.4}$$

This result can readily be applied to our system of interest (2.46) by simply substituting $\Delta t = 1$ and $B = B^{-2} = I$, with I the identity matrix. The sought expression (2.49) for the entropy production rate then follows.

Fluctuation-Dissipation Relation

The derivation consists simply in applying the generalized FDR:

$$R_{x^{(j)},\,x^{(k)}}(t) = -\left\langle x_t^{(k)} \frac{\partial \ln \rho(\boldsymbol{x})}{\partial x^{(j)}}\bigg|_{t=0}\right\rangle \tag{A.5}$$

having substituted $B(\boldsymbol{x}_t) = x_t^{(k)}$ in the general formulation (2.80), and assumed that the considered process admits a smooth invariant distribution $\rho(\boldsymbol{x})$. Solving iteratively Eq. (A.1), setting for simplicity $\Delta t = 1$, we find:

$$\boldsymbol{x}_t = A^t \boldsymbol{x}_0 + \sum_{s=0}^{t-1} A^{t-s-1} B \boldsymbol{\eta}_s\,. \tag{A.6}$$

This yields the following relation between time correlations and the matrix A:

$$C_t \equiv \langle \boldsymbol{x}_t \boldsymbol{x}_0^T\rangle = A^t \langle \boldsymbol{x}_0 \boldsymbol{x}_0^T\rangle \;\equiv A^t C_0. \tag{A.7}$$

On the other hand, the r.h.s. of (A.5) reads

$$
\begin{aligned}
&- \int d\boldsymbol{x}_0 \, dx_t^{(k)} x_t^{(k)} \, \frac{\partial \ln \rho(\boldsymbol{x}_0)}{\partial x_0^{(j)}} \, \rho(x_t^{(k)}|\boldsymbol{x}_0)\rho(\boldsymbol{x}_0) \\
&= - \int d\boldsymbol{x}_0 \, dx_t^{(k)} x_t^{(k)} \, \frac{\partial \rho(\boldsymbol{x}_0)}{\partial x_0^{(j)}} \, \rho(x_t^{(k)}|\boldsymbol{x}_0) \\
&= \int d\boldsymbol{x}_0 \, dx_t^{(k)} x_t^{(k)} \, \rho(\boldsymbol{x}_0) \, \frac{\partial \rho(x_t^{(k)}|\boldsymbol{x}_0)}{\partial x_0^{(j)}} \\
&= - \int d\boldsymbol{x}_0 \, dx_t^{(k)} x_t^{(k)} \, \rho(\boldsymbol{x}_0) \, [A^t]^{kj} \, \frac{\partial \rho(x_t^{(k)}|\boldsymbol{x}_0)}{\partial x_t^{(k)}} \ ,
\end{aligned}
$$

where we have indicated by $\rho(x_t^{(k)}|\boldsymbol{x}_0)$ the probability density of $x_t^{(k)}$ conditioned to the initial state $\boldsymbol{x}_0$. In the passage from second to third line an integration by parts with respect to $x_0^{(j)}$ is performed, while from third to fourth line we noticed that the derivative can be switched from $x_0^{(j)}$ to $x_t^{(k)}$, since $\rho(x_t^{(k)}|\boldsymbol{x}_0)$ depends on $x_t^{(k)}$ and $x_0^{(j)}$ only through the linear combination $x_t^{(k)} - \sum_i [A^t]^{ki} x_0^{(i)}$. Integrating by parts with respect to $x_t^{(k)}$ one obtains for (A.5):

$$
R_{x^{(j)},\, x^{(k)}}(t) = [A^t]^{kj} \tag{A.8}
$$

that in matrix form becomes, taking into account (A.7),

$$
R_t = C_t C_0^{-1} \ . \tag{A.9}
$$

This is the FDR for linear Gaussian processes that was verified in Paragraph 2.3.4, derived here for discrete-time evolutions but valid also for continuous-time dynamics.

Appendix B

Lyapunov exponents and their extensions

Lyapunov exponents [58, 59] quantify the mean rate of divergence of trajectories starting infinitesimally close to a reference one, generalizing the concept of linear stability to aperiodic motions.

Let us consider a n-dimensional trajectory $\boldsymbol{x}(t)$ generated by the ODE

$$\dot{\boldsymbol{x}} = \boldsymbol{f}(\boldsymbol{x})\,. \tag{B.1}$$

We are interested in the behaviour of nearby trajectories $\boldsymbol{x}'(t)$ starting from initial conditions $\boldsymbol{x}'(0)$ such that: $\boldsymbol{x}'(0) = \boldsymbol{x}(0) + \delta\boldsymbol{x}(0)$, $|\delta\boldsymbol{x}(0)| \ll 1$. Supposing that $\delta\boldsymbol{x}(t) = \boldsymbol{x}'(t) - \boldsymbol{x}(t)$ remains (infinitesimally) small at all times, then $\delta\boldsymbol{x}$ can be considered as a vector $\boldsymbol{z}(t)$ in tangent space. Its time evolution is obtained by linearizing Eq. (B.1):

$$\dot{\boldsymbol{z}} = J(\boldsymbol{x})\boldsymbol{z} \tag{B.2}$$

where $J_{ij}(\boldsymbol{x}(t)) = \partial f_i(\boldsymbol{x})/\partial x_j|_{\boldsymbol{x}(t)}$ is the Jacobian matrix. As a consequence of the Oseledec theorem [115], under quite general hypotheses, an orthonormal basis $\{\boldsymbol{e}_i(\boldsymbol{x}(t))\}$ exists in tangent space such that $\boldsymbol{z}$ can be written as:

$$\boldsymbol{z}(t) = \sum_{i=1}^{n} c_i\,|\boldsymbol{z}(0)|\,\boldsymbol{e}_i(\boldsymbol{x}(t))\,e^{\lambda_i t}\,, \tag{B.3}$$

with generic coefficients $\{c_i\}$. Eq. (B.3) roughly means that a sphere of radius ε and center $\boldsymbol{x}(0)$ is deformed with time into an "ellipsoid" of semi-axes $\varepsilon_i(t) = \varepsilon\exp(\lambda_i t)$ directed along the $\boldsymbol{e}_i$ vectors. The quantities $\lambda_1 \geq \lambda_2 \geq \cdots \geq \lambda_n$ are called *characteristic Lyapunov Exponents* (LEs).

The maximum LE λ_1 plays the dominant role in determining the nature of a dynamical system. Defining the response function $R_\tau(t) = |\delta\boldsymbol{x}(\tau+t)|/|\delta\boldsymbol{x}(\tau)|$, such exponent can be defined by averaging the logarithm of the response function over the possible initial conditions along the trajectory [116]:

$$\lambda_1 = \lim_{t\to\infty}\frac{1}{t}\,\overline{\ln R(t)}\,, \tag{B.4}$$

in which $\overline{(\cdot)}$ indicates a time average over τ. When the limit exists and yield $\lambda_1 > 0$, then the trajectory shows sensitivity to initial conditions and the system is *chaotic*.

Let us point out that Lyapunov exponents are associated to a single trajectory, thus the dependence on $\boldsymbol{x}(0)$ has to be retained unless the dynamics is ergodic.

Characteristic LEs, however, cannot account for time fluctuations due to their global character. For instance, (B.4) provides an average measurement of the expansion rate, but tells us nothing about a possible intermittent behaviour. Higher-order moments of $R_\tau(t)$ may be studied to better quantify fluctuations, and to this end *generalized LEs* $L(q)$ can be introduced:

$$L(q) = \lim_{t\to\infty} \frac{1}{t} \ln \overline{R^q(t)} \ . \tag{B.5}$$

Interestingly, the maximum LE can be recovered from the generalized ones as: $\lambda_1 = \lim_{q\to 0} L(q)/q = dL(q)/dq|_{q=0}$. If fluctuations are absent, then $L(q) = \lambda_1 q$.

A further extension of LEs stems from the interest in considering finite-size perturbations, that are common in real systems. Here the linear tangent-space formalism does not apply, therefore alternative methods are necessary to study the divergence of nearby trajectories. A possibility is to consider the Finite-Size Lyapunov Exponent (FSLE) [60, 59], which quantifies at different observation scales the average growth rate of non-infinitesimal perturbations. If such perturbations have initial amplitude δ and we want to follow them up to a chosen tolerance Δ, one can define a predictability time $T(\delta, \Delta)$ as the time it takes for a perturbation to grow from size δ to size Δ. The natural definition of the FSLE is an average of some function of the predictability time, such that if both δ and Δ are infinitesimal one recovers the usual maximum LE. A possible choice is:

$$\lambda(\delta, \Delta) = \left\langle \frac{1}{T(\delta, \Delta)} \right\rangle \ln\left(\frac{\Delta}{\delta}\right) \ , \tag{B.6}$$

but others viable options exist. The authors [60] also propose, besides (B.6), to measure the time T_r an initial perturbation of size δ needs to reach a size $r\delta$, with r a chosen growth factor. Once that separation is attained, the perturbed trajectory $\boldsymbol{x}'$ is rescaled at the original distance along the direction δx, and the procedure is repeated several times. A FSLE at scale δ is then computed as:

$$\lambda(\delta) = \left\langle \frac{1}{T_r} \ln\left(\frac{|\delta\boldsymbol{x}(T_r)|}{|\delta\boldsymbol{x}(0)|}\right)\right\rangle = \frac{1}{\langle T_r\rangle_e} \ln r \ , \tag{B.7}$$

where $\langle\cdot\rangle_e$ is an average over many consecutive experiments. For infinitesimal errors δ and not too large r this definition yields the maximal LE. Other FSLEs are present in the literature, and we refer the reader to [60, 58] and references therein.

Appendix C

Numerical details of simulations

Two-scales Lorenz96 model

The model used in the numerical computation, defined by Eqs. (3.5), is made $N = 30$ slow variables and $K = 5$ fast variables for each slow one, for a total of $D = N(K+1) = 180$ degrees of freedom. The numerical integration is performed by means of a 4th order Runge-Kutta algorithm. The integration time step employed is $dt = 5 \cdot 10^{-5}$ for both inviscid and viscous cases. It was chosen by running a simulation without forcing and damping terms and ensuring that the total energy remained constant (within a very small range) for simulation times of $\mathcal{O}(10^5)$. The study required very long runs of the inviscid system, so it was necessary to minimize as much as possible the discrepancy between the total energy at the beginning and at the end of the simulations. The initial conditions, for both cases, are drawn following a common protocol for the Lorenz96 model: all X's and y's are given a common positive value, chosen here to be 0.1, and then one fast and one slow variable, randomly extracted, are perturbed by an amount δ_X and δ_y. In the inviscid model $\delta_X = \delta_y = 10^{-4}$, whereas in the viscous one $\delta_X = b\,\delta_y = 10^{-4}$. For completeness we remember that the parameter used in the viscous system are: $c = 5$, $b = 10$, $h = 1$ and $F = 10$, while in the inviscid system we put $F = 0$ and the linear damping terms are dropped in both (3.5a) and (3.5b).

Sabra shell model

The Sabra shell model, Eq. (4.68), with N shells was integrated by means of a 4th order Runge-Kutta algorithm, with explicit integration of the linear term (see e.g. [117]). In the turbulent case, the moduli of the complex shell velocities were first initialized according to the scaling law $|u_n| \sim k_n^{-1/2}$, while the phases were assigned randomly in $[0, 2\pi)$. In the inviscid and unforced shell model we fixed the total energy to $E_{tot} = 0.13$ and distributed it equally among all shells as $|u_n| = \sqrt{2E_{tot}/N}$, with phases assigned randomly as well. Then, in both cases, we let the system evolve for a long enough transient of time (many large eddy turnover times) until a stationary state is reached, after which we start our measurements. As for the

forcing f_n in (4.68), we inject energy at scale n_f and $n_f + 1$ by imposing

$$f_n = \begin{cases} \epsilon/(2u_n^*) & \text{for} \quad n = n_f, n_f + 1 \\ 0 & \text{otherwise} \end{cases} \tag{C.1}$$

so that the input power $\sum_n \mathrm{Re}(f_n u_n^*) = \epsilon$ is constant at each timestep. In all our simulations $\epsilon = 1$ was chosen.

Table C.1 summarizes the parameters we used in the three simulations, run-LSF, run-Eq and run-ISF.

Parameter	**run-LSF**	**run-Eq**	**run-ISF**
Δt	$5 \cdot 10^{-5}$	$5 \cdot 10^{-5}$	10^{-5}
N	24	15	30
k_0	2^{-4}	2^{-4}	2^{-10}
n_f	1	N.A.	13
ν	10^{-6}	0	$5 \cdot 10^{-7}$

Table C.1. Values of the parameters used in numerical simulations. Run-LSF and Run-ISF correspond to the forced shell model, i.e. the turbulent case, with forcing at large scales or intermediate scales, respectively, while run-Eq denotes the unforced inviscid shell model, i.e. the equilibrium case. The parameters are the time step (Δt), the number of shells (N), the smallest wave number (k_0), the smallest of the two consecutive shell numbers where the forcing is acting (n_f), and the viscosity (ν).

Appendix D

Issues on the numerical computation of asymmetric correlations

In this Appendix we discuss some delicate issues about the numerical computation of the correlation functions (2.62) and its equivalent form (2.63). First of all, we can rewrite Eq. (2.63) as

$$\Phi_x(\tau) = \Theta_x(\tau) + \Psi_x(\tau)\,, \tag{D.1}$$

with $\Theta_x(\tau) = \frac{1}{3}\left[\langle x^3(t+\tau)\rangle - \langle x^3(t)\rangle\right]$. Owing to the assumed stationarity of $x(t)$, one expects $\Theta_x(\tau) = 0$, and thus $\Phi_x(\tau) \equiv \Psi_x(\tau)$. However, in numerical evaluations, due to the way cancellations are realized, the two equivalent functions Ψ_x and Φ_x have different pros and cons, as discussed below. In the following we will drop the subscript $_x$ and the time dependence from the x variable to ease the notation.

The obvious advantage of computing $\Psi(\tau)$ is that, especially at large τ, it guarantees the cancellation of the term $\Theta(\tau)$ because it is automatically imposed. This can be appreciated from Figure D.1 where one can see that, at large τ, the curves obtained computing Ψ in the Sabra model, i.e. with $x(t) = e_n(t)$, tend to be smoother than those obtained by computing Φ, although both curves do convey the same result. However, as will be shown below, problems due to statistical convergence can manifest at small τ, while the computation of $\Phi(\tau)$ is more efficient in ensuring the cancellations at small τ's. To understand such issue it is useful to Taylor-expand the functions $\Theta(\tau)$, $\Psi(\tau)$ and $\Phi(\tau)$ at $\tau \simeq 0$, stopping at third order:

$$\begin{aligned}
\Theta(\tau) &= \langle x^2\dot{x}\rangle\tau + \frac{1}{2}\langle[2x\dot{x}^2 + x^2\ddot{x}]\rangle\tau^2 \\
&+ \frac{1}{6}\langle[2\dot{x}^3 + 6x\dot{x}\ddot{x} + x^2\dddot{x}]\rangle\tau^3 + \dots \qquad \text{(D.2)} \\
\Psi(\tau) &= -\langle x^2\dot{x}\rangle\tau - \frac{1}{2}\langle[2x\dot{x}^2 + x^2\ddot{x}]\rangle\tau^2 \\
&- \frac{1}{6}\langle[6x\dot{x}\ddot{x} + x^2\dddot{x}]\rangle\tau^3 + \dots\,. \qquad \text{(D.3)} \\
\Phi(\tau) &= \frac{1}{3}\langle\dot{x}^3\rangle\tau^3 + \dots\,. \qquad \text{(D.4)}
\end{aligned}$$

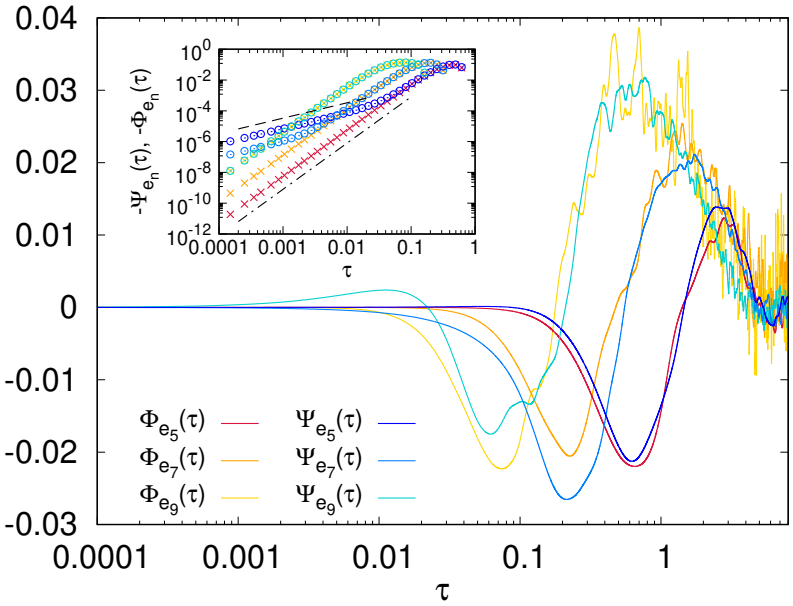

Figure D.1. Correlation functions $\Psi_{e_n}(\tau)$ and $\Phi_{e_n}(\tau)$ for the turbulent Sabra model, with $n = 5, 7, 9$. Statistics is computed on $5 \cdot 10^5$ samples. Inset: short time behavior ($\tau < 1$) of the same correlation functions with inverted sign and in logarithmic y scale. The dashed and dash-dotted lines denote respectively a linear and a cubic dependence on τ. Statistics on 10^6 samples. We point out that computing the running average of $\langle e_n^2 \dot{e}_n \rangle = d/dt \langle e_n^3 \rangle / 3$ (not shown) one can clearly see the slow convergence to zero, which is responsible for the spurious linear behavior.

Since in principle $\Phi \equiv \Psi$, then also $\Psi(\tau)$ should behave the same way at small τ. In order to see this it is useful to rewrite Eqs. (D.2-D.3) as

$$\Theta(\tau) = \frac{1}{3}\frac{d}{dt}\langle x^3 \rangle \tau + \frac{1}{2}\frac{d}{dt}\langle x^2 \dot{x} \rangle \tau^2 + \frac{1}{6}\frac{d^2}{dt^2}\langle x^2 \dot{x} \rangle \tau^3 \tag{D.5}$$

$$\begin{aligned} \Psi(\tau) &= -\frac{1}{3}\frac{d}{dt}\langle x^3 \rangle \tau - \frac{1}{2}\frac{d}{dt}\langle x^2 \dot{x} \rangle \tau^2 \\ &- \frac{1}{6}\left[\frac{d^2}{dt^2}\langle x^2 \dot{x} \rangle - 2\langle \dot{x}^3 \rangle\right]\tau^3 . \end{aligned} \tag{D.6}$$

Now all the terms of the form $d^k/dt^k \langle [\ldots] \rangle$ should vanish by stationarity, so that $\Psi(\tau) = \frac{1}{3}\langle \dot{x}^3 \rangle \tau^3$. However, the statistical convergence of $d^k/dt^k \langle [\ldots] \rangle \to 0$ may be hard to obtain with a finite statistics, leading to spurious $O(\tau)$ terms. The inset of Figure D.1 does illustrate precisely this problem. As one can see the small τ behavior of Ψ when computed for the energy of shell 5 and 7 starts with a spurious linear behavior and recovers the correct τ^3 behavior only at sufficiently large τ's, while Φ always displays the correct τ^3 dependence. For shell 9 the two curves do coincide: this is due to the fact that shell 9 is much faster than 7 and 5 so that statistical convergence, and thus the cancellations, can be realized more easily.

We conclude this appendix by noticing that in Ref. [51] the authors reported a linear behavior at small τ for an experimental time series of a turbulent velocity flow. As discussed above, we strongly believe that the linear behavior have a spurious

origin. It would thus be very interesting to re-analyze the data using $\Phi(\tau)$ instead of $\Psi(\tau)$ for confirmation.

Appendix E

Energy equipartition in the inviscid Sabra model

As discussed in Appendix C, in the inviscid shell model we start from an initial configuration of perfect energy equipartition. However, as shown in the blue plot of Figure E.1, after stationarity is reached the measured energy spectrum shows clear departures from equipartition at large shell indexes, where sharp oscillations do appear. A few more simulations (not shown), performed at changing the number of shells while keeping the energy per shell constant in the initial condition, demonstrate that the oscillations remain confined to the last 5-6 shells. Indeed by appropriately shifting the shell axis we observed that the oscillations do superimpose. This demonstrates that such oscillations are due to the boundary conditions which in the shell model, having a single variable per shell, are expected to have a stronger effect than in the truncated NS equation. The main consequence of such oscillations is to alter the equipartition value of the energy far from the boundary, so to invalidate the naive expectation $R_{eq}^{(\infty)} = 1/N$ for the asymptotic value of the energy response functions, as discussed in Section 4.5.2. In order to determine the corrected (effective) value we have run a long simulation after having performed the usual perturbation (4.86), and we computed the new spectrum (red plot in Figure E.1). This way one can directly measure the energy shift in the far-from-boundary shells, which display equipartition. Due to this effect, the actual difference between the two equipartition values is larger than it would be in the case of perfect equipartition, meaning that the asymptotic value of $R_{m,n}(t)$ is slightly larger than expected (see Figure 4.10(b)).

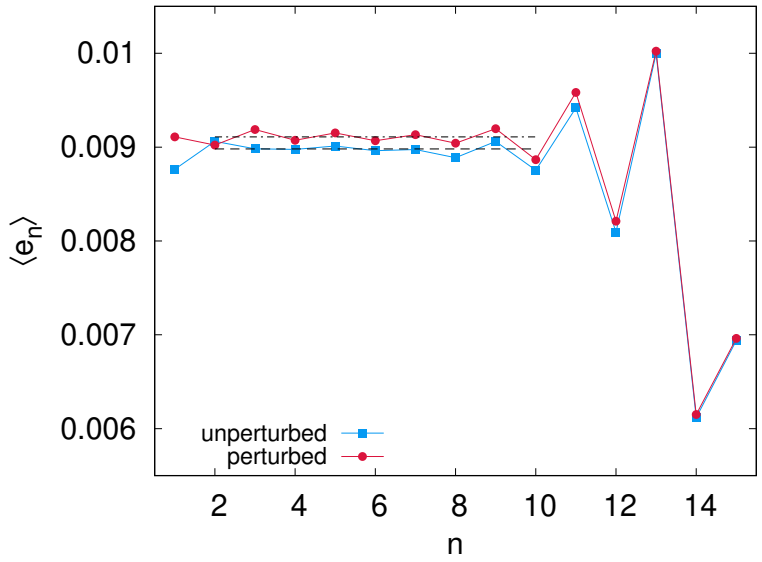

Figure E.1. Energy spectra of unperturbed (blue) and perturbed (red) inviscid Sabra shell model. The fit on the equipartition region of the perturbed spectrum, restricted to the shells which are far enough from the large-n boundary, leads to the value $R_{corr}^{(\infty)}$. Initial perturbation $\delta_{m=7} \simeq 1.79 \cdot 10^{-3}$.

Appendix F

Initial time-derivatives of response functions in the Sabra model

In this Appendix we focus on the initial time derivatives of the energy response functions, showing that they provide information on the direction of the average energy flux among shells (where present).

From Eq. (4.68) we derived the equation for the energy rate of change at shell n, which we rewrite here:

$$\dot{e}_n = -t_n + d_n + i_n \ . \tag{4.73}$$

The transfer term t_n, which interests us the most here, reads:

$$t_n = \Delta_{n+1} + b\Delta_n - (1+b)\Delta_{n-1} \ , \tag{4.74}$$

where Δ_n is defined as:

$$\Delta_n = k_n \mathrm{Im}\{u^*_{n-1}u^*_n u_{n+1}\} \ . \tag{4.77}$$

For the sake of readability we omitted the time variable in all the dynamical quantities. The transfer term explicitly shows that, by construction of the model, energy is directly exchanged between neighbors and next-to-neighbors shells, i.e. within a "range" (or distance) 2. The real quantities Δ_n play a key role in the following argument.

In both inviscid and turbulent cases (assuming in the latter to restrict ourselves in the inertial range so that the forcing is absent and the dissipation can be neglected) we can express the initial time derivative of $R_{m,n}(t)$ using (4.73) as follows:

$$\left.\frac{dR_{m,n}}{dt}\right|_{t=0} = -\frac{1}{\delta_m}\left.\left[\overline{t'_n(t)} - \overline{t_n(t)}\right]\right|_{t=0} \ , \tag{F.1}$$

where primed quantities refer to the perturbed system.

Let us start from the inviscid case. As shown in the inset of Figure 4.10(b), the time-derivative of $R_{m,n}$ is zero for $t = 0$ for any n, which can be understood as follows. Clearly, if $|n-m| > 2$ the perturbed shell m does not directly interact with shell n, which is thus unaware of the perturbation for some time and, consequently,

$dR_{m,n}/dt\big|_{t=0} = 0$. On the other hand if $|m-n| \leq 2$ the shell n will in principle be affected by energy perturbation via the non-linear term. However, at equilibrium, we should expect the shell velocities to be statistically independent and Gaussian. Now, by using Eq. (4.73) with $i_n = d_n = 0$, for $n = m+1$ it is easy to derive that

$$\left.\frac{dR_{m,m+1}}{dt}\right|_{t=0} \propto \left.\tfrac{1}{2}(\overline{\delta\Delta_{m+1}} + \overline{\delta\Delta_m})\right|_{t=0} . \tag{F.2}$$

Here $\delta\Delta_m = k_m \mathrm{Im}\{u^*_{m-1}\delta u^*_m u_{m+1}\}$ and $\delta\Delta_{m+1} = k_{m+1}\mathrm{Im}\{\delta u^*_m u^*_{m+1} u_{m+2}\}$, and in general δf denotes the difference between variable f in the perturbed and unperturbed systems. Under the assumption that the average over many realization is equivalent to the statistical average, one finds that the triple moments factorize into the product of three single moments, two of which are zero. With the same reasoning one can conclude that the derivative should be zero also for $n = m-2, m-1$ and $m+2$.

We now discuss the turbulent case. For $|m-n| > 2$ the same reasoning relying on the distance between perturbation and response applies, so that the initial derivatives of the RFs should be zero. For $|m-n| \leq 2$, one can construct the following argument. First, we rewrite the perturbed velocity (4.86) in terms of u_m as $u'_m = u_m\sqrt{1+\delta_m/e_m}$, so that

$$\delta u_m = (u'_m - u_m) = \left(\sqrt{1+\frac{\delta_m}{e_m}} - 1\right) u_m \equiv \alpha_m u_m \,, \tag{F.3}$$

where we notice that α_m is a real positive quantity for $\delta_m > 0$. Then, the equation (F.1) can be explicitly written as:

$$\delta_m \left.\frac{dR_{m,n}}{dt}\right|_{t=0} = -\left.\left[\overline{\delta\Delta_{n+1}} - \tfrac{1}{2}\overline{\delta\Delta_n} - \tfrac{1}{2}\overline{\delta\Delta_{n-1}}\right]\right|_{t=0} , \tag{F.4}$$

where

$$\delta\Delta_n\big|_{t=0} = k_n \mathrm{Im}\Big[\delta_{m,n-1}\alpha_{n-1}u^*_{n-1}u^*_n u_{n+1} + \\ + \delta_{m,n}\ \alpha_n u^*_{n-1}u^*_n u_{n+1} + \delta_{m,n+1}\alpha_{n+1}u^*_{n-1}u^*_n u_{n+1}\Big] . \tag{F.5}$$

n	**R.h.s. of** (F.4)
$m-2$	$-\overline{\alpha_m\Delta_{m-1}}\big\|_{t=0} < 0$
$m-1$	$\overline{\alpha_m\left[\frac{1}{2}\Delta_{m-1} - \Delta_m\right]}\big\|_{t=0} < 0$
$m+1$	$\overline{\alpha_m\left[\frac{1}{2}\Delta_m + \frac{1}{2}\Delta_{m+1}\right]}\big\|_{t=0} > 0$
$m+2$	$\overline{\alpha_m\frac{1}{2}\Delta_{m+1}}\big\|_{t=0} > 0$

Table F.1. Initial time derivatives of $R_{m,n}(t)$ for $|n-m| \leq 2$.

The Kronecker delta $\delta_{a,b}$ imposes that at least one of the three shell velocities involved has to be the initially-perturbed one, otherwise there will be no contribution, as seen in the previous case.

Computing the sign of the initial time derivative of the RFs amounts to studying terms of the kind (indices omitted):

$$\overline{\delta\Delta} \sim k\overline{\alpha \mathrm{Im}\{uuu\}} = \overline{\alpha\Delta}, \tag{F.6}$$

but α is positive by definition (see Eq. (F.3)), and it can be shown [9] that $\langle\Delta\rangle$ is positive on average since it is related to the energy flux (4.79). Again we will assume that $\overline{\Delta} = \langle\Delta\rangle$.

Once established this result let us reconsider (F.4) and (F.5). In Table F.1 we explicitly write the non-zero terms, when varying n in the range of indices we are studying. Given that $\overline{\Delta_n} > 0$, at least for n in the inertial range, we have that backward RFs start with negative slope, while forward ones with positive slope. Concerning the case $n = m - 1$, where the sign of the expression is not as straightforward as the others, the negativity of the r.h.s. is ensured by an explicit expression for $\overline{\Delta_n}$ found in Eq. (16) of [9].

Bibliography of the Author

1. **NC**, G. Gradenigo, and A. Vulpiani, "Thermalization without chaos in harmonic systems", *Physica A: Statistical Mechanics and its Applications*, **601**, 127581, 2022

2. **NC**, M. Cencini, and A. Vulpiani, "Nonequilibrium statistical mechanics of the turbulent energy cascade: Irreversibility and response functions", *Physical Review E*, **109**, 014113, 2024

3. D. Lucente, M. Baldovin, F. Cecconi, M. Cencini, **NC**, A. Puglisi, M. Viale, A. Vulpiani, "Conceptual and practical approaches for investigating irreversible processes", *arXiv:2410.15925*

4. **NC**, D. Lucente, "Detecting time-irreversibility in multiscale systems: correlation and response functions in the Lorenz96 model", *arXiv:2411.07005*

The results in Chapter 3 are based on article #4, those in Chapter 4 on article #2.

Bibliography

[1] J. P. Sethna. *Statistical Mechanics: Entropy, Order Parameters and Complexity.* Oxford University Press, 2006.

[2] Robert Zwanzig. *Nonequilibrium statistical mechanics.* Oxford University Press, 2001.

[3] R. Livi and P. Politi. *Nonequilibrium Statistical Physics: A Modern Perspective.* Cambridge University Press, 2017.

[4] X.-J. Zhang, H. Qian, and M. Qian. Stochastic theory of nonequilibrium steady states and its applications. Part I. *Phys. Rep.*, 510(1):1–86, 2012.

[5] D. Lucente, M. Baldovin, F. Cecconi, M. Cencini, N. Cocciaglia, A. Puglisi, M. Viale, and A. Vulpiani. Conceptual and practical approaches for investigating irreversible processes, 2024. arXiv:2410.15925.

[6] U. Frisch. *Turbulence: the legacy of A. N. Kolmogorov.* Cambridge University Press, 1995.

[7] D. Lucente, A. Baldassarri, A. Puglisi, A. Vulpiani, and M. Viale. Inference of time irreversibility from incomplete information: Linear systems and its pitfalls. *Phys. Rev. Res.*, 4:043103, 2022.

[8] E. N. Lorenz. Predictability: a problem partly solved. *Seminar on Predictability, 4-8 September 1995*, 1:1–18, 1995.

[9] V. S. L'vov, E. Podivilov, A. Pomyalov, I. Procaccia, and D. Vandembroucq. Improved shell model of turbulence. *Phys. Rev. E*, 58:1811–1822, 1998.

[10] J. L. Lebowitz and H. Spohn. A Gallavotti–Cohen-type symmetry in the large deviation functional for stochastic dynamics. *J. Stat. Phys.*, 95:333–365, 1999.

[11] C. Sarra, M. Baldovin, and A. Vulpiani. Response and flux of information in extended nonequilibrium dynamics. *Phys. Rev. E*, 104(2):024116, 2021.

[12] M. Baldovin, F. Cecconi, and A. Vulpiani. Understanding causation via correlations and linear response theory. *Phys. Rev. Res.*, 2:043436, 2020.

[13] U. Seifert. Entropy production along a stochastic trajectory and an integral fluctuation theorem. *Phys. Rev. Lett.*, 95:040602, 2005.

[14] J. M. Horowitz and T. R. Gingrich. Thermodynamic uncertainty relations constrain non-equilibrium fluctuations. *Nat. Phys.*, 16(1):15–20, 2020.

[15] Y. Pomeau. Symétrie des fluctuations dans le renversement du temps. *J. Phys. France*, 43(6):859–867, 1982.

[16] U. M. B. Marconi, A. Puglisi, L. Rondoni, and A. Vulpiani. Fluctuation–dissipation: Response theory in statistical physics. *Phys. Rep.*, 461(4):111–195, 2008.

[17] J. Pedlosky. *Geophysical Fluid Dynamics*. Springer New York, 2nd edition, 1987.

[18] K. Huang. *Statistical Mechanics*. John Wiley & Sons, 1987.

[19] L. D. Landau and E. M. Lifshitz. *Fluid Mechanics*. Pergamon Press Oxford, England, 1959.

[20] A. Majda and X. Wang. *Nonlinear Dynamics and Statistical Theories for Basic Geophysical Flows*, chapter 7.4. Cambridge University Press, 2006.

[21] J.H. Ferziger and M. Peric. *Computational Methods for Fluid Dynamics*. Springer Berlin Heidelberg, 3rd edition, 2012.

[22] T. Bohr, M. H. Jensen, G. Paladin, and A. Vulpiani. *Dynamical Systems Approach to Turbulence*. Cambridge Nonlinear Science Series. Cambridge University Press, 1998.

[23] P. Constantin, B. Levant, and E. S Titi. Analytic study of shell models of turbulence. *Physica D*, 219(2):120–141, 2006.

[24] A. J. Majda, I. Timofeyev, and E. Vanden Eijnden. Models for stochastic climate prediction. *PNAS*, 96(26):14687–14691, 1999.

[25] E. N. Lorenz. Designing chaotic models. *J. Atmos. Sci.*, 62(5):1574 – 1587, 2005.

[26] D. Chandler. *Introduction to Modern Statistical Mechanics*. Oxford University Press, 1987.

[27] S.R. de Groot and P. Mazur. *Non-equilibrium Thermodynamics*. Dover Books on Physics and Chemistry. Dover New York, 1984.

[28] M. Falcioni and A. Vulpiani. *Meccanica Statistica Elementare*. Springer Milano, 2014.

[29] L. Onsager. Reciprocal relations in irreversible processes. I. *Phys. Rev.*, 37:405–426, 1931.

[30] U. Seifert. Stochastic thermodynamics, fluctuation theorems and molecular machines. *Rep. Prog. Phys.*, 75(12):126001, 2012.

[31] E. N. Lorenz and K. A. Emanuel. Optimal sites for supplementary weather observations: Simulation with a small model. *J. Atmos. Sci.*, 55(3):399 – 414, 1998.

[32] M. R. Frank, L. Mitchell, P. S. Dodds, and C. M. Danforth. Standing swells surveyed showing surprisingly stable solutions for the Lorenz '96 model. *Int. J. Bifurc. Chaos*, 24(10):1430027, 2014.

[33] M. Carlu, F. Ginelli, V. Lucarini, and A. Politi. Lyapunov analysis of multiscale dynamics: the slow bundle of the two-scale Lorenz 96 model. *Nonlin. Processes Geophys.*, 26(2):73–89, 2019.

[34] J. Kerin and H. Engler. On the Lorenz '96 model and some generalizations, 2020.

[35] D. L. van Kekem and A. E. Sterk. Wave propagation in the Lorenz-96 model. *Nonlin. Processes Geophys.*, 25(2):301–314, 2018.

[36] N. Cocciaglia and D. Lucente. Detecting time-irreversibility in multiscale systems: correlation and response functions in the Lorenz96 model, 2024. arXiv:2411.07005.

[37] H. A. Rose and P. L. Sulem. Fully developed turbulence and statistical mechanics. *J. Phys. France*, 39(5):441–484, 1978.

[38] G. Parisi and U. Frisch. On the singularity structure of fully developed turbulence. In M. Ghil, R. Benzi, and G. Parisi, editors, *Turbulence and predictability in geophysical fluid dynamics and climate dynamics*, Enrico Fermi International School of Physics Series, pages 84–87. North-Holland, 1985.

[39] L. Biferale. Shell models of energy cascade in turbulence. *Ann. Rev. Fluid Mech.*, 35(1):441–468, 2003.

[40] P. D. Ditlevsen. *Turbulence and shell models.* Cambridge University Press, 2010.

[41] N. Cocciaglia, M. Cencini, and A. Vulpiani. Nonequilibrium statistical mechanics of the turbulent energy cascade: Irreversibility and response functions. *Phys. Rev. E*, 109:014113, 2024.

[42] S.-K. Ma. *Statistical Mechanics.* World Scientific, 1985.

[43] L. Peliti and S. Pigolotti. *Stochastic Thermodynamics: An Introduction.* Princeton University Press, 2021.

[44] L. Onsager and S. Machlup. Fluctuations and irreversible processes. *Phys. Rev.*, 91:1505–1512, 1953.

[45] I. Prigogine. *Introduction to Thermodynamics of Irreversible Processes.* Wiley, 2nd Edition, 1968.

[46] S. Bonella, G. Ciccotti, and L. Rondoni. Time reversal symmetry in time-dependent correlation functions for systems in a constant magnetic field. *EPL*, 108(6):60004, 2015.

[47] C. Bustamante, J. Liphardt, and F. Ritort. The nonequilibrium thermodynamics of small systems. *Phys. Today*, 58(7):43–48, 2005.

[48] D. J. Evans, E. G. D. Cohen, and G. P. Morriss. Probability of second law violations in shearing steady states. *Phys. Rev. Lett.*, 71:2401–2404, 1993.

[49] D. J. Evans and D. J. Searles. Equilibrium microstates which generate second law violating steady states. *Phys. Rev. E*, 50:1645–1648, 1994.

[50] G. Gallavotti and E. G. D. Cohen. Dynamical ensembles in nonequilibrium statistical mechanics. *Phys. Rev. Lett.*, 74:2694–2697, 1995.

[51] C. Josserand, M. Le Berre, T. Lehner, and Y. Pomeau. Turbulence: Does energy cascade exist? *J. Stat. Phys.*, 167:596–625, 2017.

[52] C.W. Gardiner. *Handbook of Stochastic Methods for Physics, Chemistry and the Natural Sciences*. Springer-Verlag, Berlin, 1990.

[53] R. Kubo. The fluctuation-dissipation theorem. *Rep. Progr. Phys.*, 29(1):255, 1966.

[54] R. Kubo, M. Toda, and N. Hashitsume. *Statistical physics II: nonequilibrium statistical mechanics*, volume 31. Springer Science & Business Media, 2012.

[55] R. Kubo. Statistical-mechanical theory of irreversible processes. I. General theory and simple applications to magnetic and conduction problems. *J. Phys. Soc. Jpn.*, 12(6):570–586, 1957.

[56] M. Falcioni, S. Isola, and A. Vulpiani. Correlation functions and relaxation properties in chaotic dynamics and statistical mechanics. *Phys. Lett. A*, 144(6-7):341–346, 1990.

[57] D. Bandak, N. Goldenfeld, A. A. Mailybaev, and G. Eyink. Dissipation-range fluid turbulence and thermal noise. *Phys. Rev. E*, 105:065113, Jun 2022.

[58] F. Cecconi, M. Cencini, and A. Vulpiani. *Chaos: from simple models to complex systems*. World Scientific, 2010.

[59] M. Cencini and A. Vulpiani. Finite size Lyapunov exponent: review on applications. *J. Phys. A: Math. Theor.*, 46(25):254019, 2013.

[60] A. Aurell, G. Boffetta, A. Crisanti, G. Paladin, and A. Vulpiani. Predictability in the large: an extension of the concept of Lyapunov exponent. *J. Phys. A: Math. Gen.*, 30(1):1, 1997.

[61] E. N. Lorenz. The predictability of a flow which possesses many scales of motion. *Tellus*, 21(3):289–307, 1969.

[62] E. N. Lorenz. Deterministic nonperiodic flow. *J.Atmos. Sci.*, 20(2):130 – 141, 1963.

[63] G. Boffetta, A. Celani, M. Cencini, G. Lacorata, and A. Vulpiani. The predictability problem in systems with an uncertainty in the evolution law. *J. Phys. A*, 33(7):1313, 2000.

[64] G. Lacorata and A. Vulpiani. Fluctuation-response relation and modeling in systems with fast and slow dynamics. *Nonlin. Processes Geophys.*, 14(5):681–694, 2007.

[65] A. Karimi and M. R. Paul. Extensive chaos in the Lorenz-96 model. *Chaos*, 20(4):043105, 2010.

[66] G. Gallavotti and V. Lucarini. Equivalence of non-equilibrium ensembles and representation of friction in turbulent flows: The Lorenz 96 model. *J. Stat. Phys.*, 156:1027–1065, 2014.

[67] D. Orrell and L. A. Smith. Visualising bifurcations in high dimensional systems: The spectral bifurcation diagram. *Int. J. Bifurcat. Chaos*, 13(10):3015–3027, 2003.

[68] R. J. J. Stappers and J. Barkmeijer. Optimal linearization trajectories for tangent linear models. *Q. J. Roy. Meteor. Soc.*, 138(662):170–184, 2012.

[69] B. de Leeuw, S. Dubinkina, J. Frank, A. Steyer, X. Tu, and E. Van Vleck. Projected shadowing-based data assimilation. *SIAM J. Appl. Dyn. Syst.*, 17(4):2446–2477, 2018.

[70] L. Basnarkov and L. Kocarev. Forecast improvement in Lorenz 96 system. *Nonlin. Processes Geophys.*, 19(5):569–575, 2012.

[71] A. E. Sterk, M. P. Holland, P. Rabassa, H. W. Broer, and R. Vitolo. Predictability of extreme values in geophysical models. *Nonlin. Processes Geophys.*, 19(5):529–539, 2012.

[72] D. L. van Kekem and A. E. Sterk. Travelling waves and their bifurcations in the Lorenz-96 model. *Physica D*, 367:38–60, 2018.

[73] R. M. Lieb-Lappen and C. M. Danforth. Aggressive shadowing of a low-dimensional model of atmospheric dynamics. *Physica D*, 241(6):637–648, 2012.

[74] G. Benettin, L. Galgani, and J.-M. Strelcyn. Kolmogorov entropy and numerical experiments. *Phys. Rev. A*, 14(6):2338, 1976.

[75] H. Xu, A. Pumir, G. Falkovich, E. Bodenschatz, M. Shats, H. Xia, N. Francois, and G. Boffetta. Flight–crash events in turbulence. *Proc. Nat. Acad. Sci.*, 111(21):7558–7563, 2014.

[76] G. Boffetta, G. Lacorata, S. Musacchio, and A. Vulpiani. Relaxation of finite perturbations: Beyond the fluctuation-response relation. *Chaos*, 13(3):806–811, 2003.

[77] M. Lesieur. *Turbulence in Fluids*. Fluid Mechanics and Its Applications. Springer Netherlands, 2008.

[78] A. N. Kolmogorov. The local structure of turbulence in incompressible viscous fluid for very large Reynolds numbers. *Dokl. Acad. Nauk SSSR*, 30:301–305, 1941.

[79] A. N. Kolmogorov. Dissipation of energy in locally isotropic turbulence. *Dokl. Acad. Nauk SSSR*, 32:16–18, 1941.

[80] H. K. Moffatt. The degree of knottedness of tangled vortex lines. *J. Fluid Mech.*, 35(1):117–129, 1969.

[81] L. Onsager. Statistical hydrodynamics. *Il Nuovo Cimento*, 6(2):279–287, 1949.

[82] G.L. Eyink and H. Spohn. Negative-temperature states and large-scale, long-lived vortices in two-dimensional turbulence. *J. Stat. Phys.*, 70:833–886, 1993.

[83] R. H. Kraichnan. Helical turbulence and absolute equilibrium. *J. Fluid Mech.*, 59(4):745–752, 1973.

[84] A. S. Monin and A. M. Yaglom. *Statistical Fluid Mechanics: Mechanics of Turbulence. Vol 2*. MIT Press, Cambridge, Massachusetts, 1975.

[85] A. N. Kolmogorov. A refinement of previous hypotheses concerning the local structure of turbulence in a viscous incompressible fluid at high Reynolds number. *J. Fluid Mech.*, 13(1):82–85, 1962.

[86] U. Frisch and R. Morf. Intermittency in nonlinear dynamics and singularities at complex times. *Phys. Rev. A*, 23:2673–2705, 1981.

[87] U. Frisch, P.-L. Sulem, and M. Nelkin. A simple dynamical model of intermittent fully developed turbulence. *J. Fluid Mech.*, 87(4):719–736, 1978.

[88] B. B. Mandelbrot. Intermittent turbulence in self-similar cascades: divergence of high moments and dimension of the carrier. *J. Fluid Mech.*, 62(2):331–358, 1974.

[89] R. Benzi, G. Paladin, G. Parisi, and A. Vulpiani. On the multifractal nature of fully developed turbulence and chaotic systems. *J. Phys. A: Math. Gen.*, 17(18):3521, 1984.

[90] Z.-S. She and E. Leveque. Universal scaling laws in fully developed turbulence. *Phys. Rev. Lett.*, 72:336–339, 1994.

[91] A. M. Obukhov. Some general characteristic equations of the dynamics of the atmosphere. *Atmos. Oceanic Phys.*, 7:41, 1971.

[92] E. B. Gledzer. System of hydrodynamic type admitting two quadratic integrals of motion. *Sov. Phys. Dokl.*, 18:216, 1973.

[93] V. N. Desnyansky and E. A. Novikov. The evolution of turbulence spectra to the similarity regime. *Atmos. Oceanic Phys.*, 10:127, 1974.

[94] K. Ohkitani and M. Yamada. Temporal intermittency in the energy cascade process and local Lyapunov analysis in fully-developed model turbulence. *Prog. Theor. Phys.*, 81(2):329–341, 1989.

[95] E. Aurell, P. Frick, and V. Shaidurov. Hierarchical tree-model of 2D-turbulence. *Physica D*, 72(1):95–109, 1994.

[96] C. Gloaguen, J. Léorat, A. Pouquet, and R. Grappin. A scalar model for MHD turbulence. *Physica D*, 17(2):154–182, 1985.

[97] M. H. Jensen, G. Paladin, and A. Vulpiani. Shell model for turbulent advection of passive-scalar fields. *Phys. Rev. A*, 45:7214–7221, 1992.

[98] R. Benzi, L. Biferale, R. M. Kerr, and E. Trovatore. Helical shell models for three-dimensional turbulence. *Phys. Rev. E*, 53:3541–3550, 1996.

[99] E. S. C. Ching, H. Guo, and W.C. Cheng. Understanding the different scaling behavior in various shell models proposed for turbulent thermal convection. *Physica D*, 237(14):2009–2014, 2008.

[100] G. Boffetta, F. De Lillo, and S. Musacchio. Shell model for quasi-two-dimensional turbulence. *Phys. Rev. E*, 83:066302, 2011.

[101] P. D. Ditlevsen and I. A. Mogensen. Cascades and statistical equilibrium in shell models of turbulence. *Phys. Rev. E*, 53:4785–4793, 1996.

[102] R. Benzi, L. Biferale, R. Fisher, D. Q. Lamb, and F. Toschi. Inertial range eulerian and lagrangian statistics from numerical simulations of isotropic turbulence. *J. Fluid Mech.*, 653:221–244, 2010.

[103] L. Biferale, G. Boffetta, A. Celani, and F. Toschi. Multi-time, multi-scale correlation functions in turbulence and in turbulent models. *Physica D*, 127(3-4):187–197, 1999.

[104] M. Cencini, L. Biferale, G. Boffetta, and M. De Pietro. Time irreversibility and multifractality of power along single particle trajectories in turbulence. *Phys. Rev. Fluids*, 2(10):104604, 2017.

[105] L. Biferale, A. A. Mailybaev, and G. Parisi. Optimal subgrid scheme for shell models of turbulence. *Phys. Rev. E*, 95(4):043108, 2017.

[106] V. Dallas, S. Fauve, and A. Alexakis. Statistical equilibria of large scales in dissipative hydrodynamic turbulence. *Phys. Rev. Lett.*, 115(20):204501, 2015.

[107] A. Cameron, A. Alexakis, and M.-E. Brachet. Effect of helicity on the correlation time of large scales in turbulent flows. *Phys. Rev. Fluids*, 2(11):114602, 2017.

[108] A. Alexakis and M.-E. Brachet. On the thermal equilibrium state of large-scale flows. *J. Fluid Mech.*, 872:594–625, 2019.

[109] J.-B. Gorce and E. Falcon. Statistical equilibrium of large scales in three-dimensional hydrodynamic turbulence. *Phys. Rev. Lett.*, 129(5):054501, 2022.

[110] D. N. Hosking and A. A. Schekochihin. Emergence of long-range correlations and thermal spectra in forced turbulence. *J. Fluid Mech.*, 973:A13, 2023.

[111] M. Ding, J.-H. Xie, and J. Wang. Departure from the statistical equilibrium of large scales in forced three-dimensional homogeneous isotropic turbulence. *J. Fluid Mech.*, 984:A71, 2024.

[112] E. Aurell, G. Boffetta, A. Crisanti, P. Frick, G. Paladin, and A. Vulpiani. Statistical mechanics of shell models for two-dimensional turbulence. *Phys. Rev. E*, 50:4705–4715, Dec 1994.

[113] T. Gilbert, V. S. L'vov, A. Pomyalov, and I. Procaccia. Inverse cascade regime in shell models of two-dimensional turbulence. *Phys. Rev. Lett.*, 89(7):074501, 2002.

[114] M. Baldovin. Unpublished notes.

[115] J. P. Eckmann and D. Ruelle. Ergodic theory of chaos and strange attractors. *Rev. Mod. Phys.*, 57:617–656, 1985.

[116] G. Paladin and A. Vulpiani. Anomalous scaling laws in multifractal objects. *Phys. Rep.*, 156(4):147–225, 1987.

[117] L. Biferale, M. Cencini, M. De Pietro, G. Gallavotti, and V. Lucarini. Equivalence of nonequilibrium ensembles in turbulence models. *Phys. Rev. E*, 98:012202, 2018.